

## Special Issue: *Australopithecus sediba*

### The Anatomy of the Lower Limb Skeleton of *Australopithecus sediba*

JEREMY M. DESILVA

Department of Anthropology, Dartmouth College, Hanover, NH 03755, USA; and, Evolutionary Studies Institute, University of the Witwatersrand, Private Bag 3, WITS 2050, Johannesburg, SOUTH AFRICA; [jeremy.m.desilva@dartmouth.edu](mailto:jeremy.m.desilva@dartmouth.edu)

KRISTIAN J. CARLSON

Department of Integrative Anatomical Sciences, Keck School of Medicine of the University of Southern California, Los Angeles, CA 90033, USA; and, Evolutionary Studies Institute, University of the Witwatersrand, Private Bag 3, WITS 2050, Johannesburg, SOUTH AFRICA; [kristian.carlson@usc.edu](mailto:kristian.carlson@usc.edu)

ALEXANDER G. CLAXTON

Department of Anthropology, Boston University, Boston, MA 02215, USA; [alexgclaxton@gmail.com](mailto:alexgclaxton@gmail.com)

WILLIAM E.H. HARCOURT-SMITH

Department of Anthropology, Lehman College, CUNY, Bronx, NY 03755; Division of Paleontology, American Museum of Natural History, New York, NY 10024; Department of Anthropology, City University of New York Graduate Center, New York, NY 10016; USA; and, Evolutionary Studies Institute, University of the Witwatersrand, Private Bag 3, WITS 2050, Johannesburg, SOUTH AFRICA; [willhs@amnh.org](mailto:willhs@amnh.org)

ELLISON J. MCNUTT

Department of Anthropology; and, Ecology, Evolution, Ecosystems, and Society, Dartmouth College, Hanover, NH 03755, USA; [Ellison.j.mcnutt.gr@dartmouth.edu](mailto:Ellison.j.mcnutt.gr@dartmouth.edu)

ADAM D. SYLVESTER

Center for Functional Anatomy and Evolution, Johns Hopkins School of Medicine, Baltimore, MD 21205, USA; [adam.d.sylvester@gmail.com](mailto:adam.d.sylvester@gmail.com)

CHRISTOPHER S. WALKER

Department of Molecular Biomedical Sciences, College of Veterinary Medicine, North Carolina State University, Raleigh, NC 27607; Department of Evolutionary Anthropology, Box 90383, Duke University, Durham, NC 27708, USA; and, Evolutionary Studies Institute, University of the Witwatersrand, Private Bag 3, WITS 2050, Johannesburg, SOUTH AFRICA; [Christopher\\_walker@ncsu.edu](mailto:Christopher_walker@ncsu.edu)

BERNHARD ZIPFEL

Evolutionary Studies Institute, University of the Witwatersrand, Private Bag 3, WITS 2050, Johannesburg, SOUTH AFRICA; [Bernhard.zipfel@wits.ac.za](mailto:Bernhard.zipfel@wits.ac.za)

STEVEN E. CHURCHILL

Department of Evolutionary Anthropology, Duke University, Durham, NC 27708, USA; and, Evolutionary Studies Institute, University of the Witwatersrand, Private Bag 3, WITS 2050, Johannesburg, SOUTH AFRICA; [churchy@duke.edu](mailto:churchy@duke.edu)

LEE R. BERGER

Evolutionary Studies Institute, University of the Witwatersrand, Private Bag 3, WITS 2050, Johannesburg, SOUTH AFRICA; [profleeberger@ahoo.com](mailto:profleeberger@ahoo.com)

submitted: 9 September 2017; accepted 24 July 2018

#### ABSTRACT

The functional anatomy of the lower limb skeleton has featured prominently in reconstructions of locomotion in early hominins. Based on recent discoveries, many scholars now suggest that Plio-Pleistocene hominins experimented with different forms of bipedalism, due in part to variation in how arboreally adapted some hominin species remained. The 1.977 Ma *Australopithecus sediba* fossils from Malapa, South Africa, are central to the hypothesis of locomotor and kinematic variation in early hominins. Here, we provide detailed anatomical descriptions of the

thigh, leg, and foot of *Au. sediba* and present additional comparative and functional analyses. *Australopithecus sediba* possesses, in general, an australopith-like hip and knee, though the anatomy of these joints differs in important ways from other australopiths. 3D geometric morphometrics and comparative linear and angular analyses demonstrate that each individual foot bone in *Au. sediba* displays a mosaic of anatomies conducive for both terrestrial bipedalism and arboreality. These findings demonstrate both the taxonomic validity of *Au. sediba* and suggest that australopiths had both diverse locomotor strategies and variation in locomotor kinematics.

This special issue is guest-edited by Scott A. Williams (Department of Anthropology, New York University) and Jeremy M. DeSilva (Department of Anthropology, Dartmouth College). This is article #7 of 9.

## INTRODUCTION

The last two decades have witnessed the discovery and scientific description of new foot and ankle fossils that have been critical for reconstructing bipedalism in early hominins (Clarke and Tobias 1995; Haile-Selassie et al. 2012; Harcourt-Smith et al. 2015; Jungers et al. 2009; Lovejoy et al. 2009; Pontzer et al. 2010; Ward et al. 2012; Zipfel et al. 2011). Additionally, the functional anatomy of the hip (Day 1969; Lovejoy et al. 1973; Lovejoy et al. 2002; MacLachy 1996; Marchi et al. 2017; Napier 1964; Richmond and Jungers 2009; Ruff 1995; Stern and Susman 1983; Ward et al. 2015) and the knee (Heiple and Lovejoy 1971; Le Gros Clark 1947; Lovejoy 2007; Stern and Susman 1983; Sylvester et al. 2011; Tardieu 1981) continue to be central to reconstructions of locomotion in australopiths and early *Homo*. The 1.977 Ma *Australopithecus sediba* skeletons from Malapa, South Africa (Pickering et al. 2011), preserve lower limb bones that have been comparatively and functionally assessed in previous papers (Berger et al. 2010; DeSilva et al. 2013; Zipfel et al. 2011). Here, we provide detailed anatomical descriptions and additional comparative analyses.

The relative paucity of lower limb remains, compared to the extraordinary and unprecedented completeness of the upper limb of *Au. sediba* (Churchill et al. 2013; Kivell et al. 2011), belies the rich information that can be gleaned from the preserved anatomies of the lower limb. The holotype juvenile skeleton MH1 preserves the proximal portion of a right femur, which is complete minus the epiphyses of the head and trochanters. Additional elements attributed to the MH1 leg include a right tibial fragment (which demonstrates that the U.W. 88-21/40 tibia belongs to another adult individual, designated MH4) and a fibula fragment. MH1 also is attributed a calcaneal apophysis and partial fourth and fifth metatarsals. The currently more complete adult female skeleton, MH2, preserves the proximal portion of a right femur, a fragmentary femoral shaft fragment, and a knee joint, preserving the distal femur, proximal tibia, and patella. Additional elements from the leg of MH2 include a left proximal tibial fragment and a left proximal fibula. An associated adult distal tibia, talus, and calcaneus are also attributed to the MH2 skeleton. There is a nearly complete tibia from another individual (MH4), and an unattributed adult fifth metatarsal. Detailed anatomical descriptions are provided below.

## MATERIALS AND METHODS

### ANATOMICAL DESCRIPTIONS

Anatomical descriptions and brief functional remarks are presented for the lower limb fossils recovered from Malapa, South Africa (2008-2011) (Table 1). All measurements are reported in mm. Individual measurements are described or illustrated in the text, and when necessary, additional details for specific measurements are added. Descriptions are arranged by element (beginning proximally with the femur and moving distally to the foot) and then by individual (MH1 followed by MH2). Abbreviations used throughout include: AP (anteroposterior; anteroposteriorly); ML (mediolateral; mediolaterally); PD (proximodistal; proximodistally); DP (dorsoplantar; dorsoplantarly); SI (superoinferior; superoinferiorly).

### FEMORAL RECONSTRUCTION

The medial condyle of U.W. 88-63 was reconstructed using a combination of statistical and geometric reconstruction procedures, as advocated by Gunz et al. (2009). The extant reference sample consists of 93 femora representing three extant hominid species (Table 2). The bones are parts of collections curated by the National Museum of Natural History (Smithsonian Institution, Washington D.C.), the Max Planck Institute for Evolutionary Anthropology (Leipzig, Germany), the Department of Anthropology at the University of Vienna (Vienna, Austria), the William M. Bass Skeletal Collection housed by the Department of Anthropology at the University of Tennessee (Knoxville, TN) and the Museum für Naturkunde (Berlin, Germany). All bones are from adult individuals, are free of obvious pathology and right femora were always preferred when available. On occasion, when only left femora were available, reflected surface models were substituted. All extant femora were scanned using a Breuckmann OptoTop-HE white light surface scanner that directly produces triangulated mesh surface models.

To quantify three-dimensional shape variation in the reference sample, 1007 sliding semilandmarks were distributed across each joint surface using custom software written for Matlab © (MathWorks, Inc., Natick, MA) following the protocol outlined by Gunz et al. (2005). One hundred forty-one of the landmarks were placed along the articular margin and the remaining 866 were placed on the articular

TABLE 1. LOWER LIMB AND FOOT FOSSILS FROM AUSTRALOPITHECUS SEDIBA.

Specimen number	Element	Individual
U.W. 88-4/5/39	Right proximal femur	MH1
U.W. 88-51	Right proximal femur	MH2
U.W. 88-53	Right femoral shaft	MH2
U.W. 88-63	Right distal femur	MH2
U.W. 88-79/100	Right patella	MH2
U.W. 88-89	Right tibial shaft	MH1
U.W. 88-64/78	Right proximal tibia	MH2
U.W. 88-24	Left proximal tibia	MH2
U.W. 88-97	Right distal tibia	MH2
U.W. 88-21/40	Right tibia	MH4
U.W. 88-18	Left fibula	MH1
U.W. 88-23/84/146/202	Left fibula	MH2
U.W. 88-98	Right talus	MH2
U.W. 88-113	Right calcaneal apophysis	MH1
U.W. 88-99	Right calcaneus	MH2
U.W. 88-22	Right 4th metatarsal	MH1
U.W. 88-16	Right 5th metatarsal	MH1
U.W. 88-33	Right proximal 5th metatarsal	unassigned

surface. All landmarks were slid along tangent planes (surface landmarks) and curves (articular margin landmarks) to minimize bending energy of the thin plate spline function relative to the updated Procrustes average (Gunz et al. 2009). Because landmarks slide off the actual specimen as they slide along tangent planes and vectors, all landmarks were projected back onto the specimen. Following sliding and projection, specimens were aligned using generalized Procrustes superimposition to remove information about location, orientation, and size (Rohlf and Slice 1990). The processes of sliding, Procrustes alignment, and updating the Procrustes average landmark configuration were repeated until landmark positions became stabilized. Although high-dimensional data (data where number of variables exceeds number of cases) pose problems for standard parametric statistical techniques (Collyer et al. 2015), this is

not the case for geometric morphometrics. In such analyses, the number of landmarks often exceeds the number of specimens (e.g., Freidline et al. 2015; Mitteroecker et al. 2004), even in the context of fossil reconstruction (Gunz et al. 2009).

Reconstructing the missing medial condyle of U.W. 88-63 consisted of estimating the coordinates of landmarks corresponding to the surface of the medial condyle. To begin, coordinates of sliding landmarks on the preserved portion of the articular surface of U.W. 88-63 were determined. This required using a reduced landmark data set; 673 of the 1007 sliding semilandmarks could be confidently placed on the preserved articular surface of the U.W. 88-63 distal femur. These landmarks covered the lateral condyle, patellar surface, and the most anterior portion of the medial condyle (more than ~1cm away from the broken edge of the

TABLE 2. EXTANT REFERENCE SAMPLE FOR DISTAL FEMUR.

Species	M	F	U	Institution
<i>Homo sapiens</i> : 20th c. North Americans	9	10	-	1
<i>Homo sapiens</i> : KhoeSan	5	10	-	2
<i>Pan troglodytes</i>	13	14	8	2, 3, 4, 5
<i>Gorilla gorilla</i>	13	11	-	2, 4, 5

All specimens are skeletally adult and free from pathology. M=male; F=female; U=unknown sex. Institutions: 1=Department of Anthropology, The University of Tennessee; 2=Department of Anthropology, University of Vienna; 3=Max Planck Institute for Evolutionary Anthropology; 4=National Museum of Natural History, Smithsonian Institution (Washington, D.C.); 5=Museum für Naturkunde (Berlin).

condyle). Although landmarks close to the broken edge of the medial condyle could have been incorporated, a more conservative approach was selected for two reasons. First, landmarks initially placed close to the broken edge could potentially slide off the preserved morphology during the sliding procedure. Second, including a small portion of the preserved medial condyle in the reconstruction provided a means of assessing the accuracy of the reconstruction. The 673 landmarks were slid to minimize bending energy of the thin plate spline function relative to the final Procrustes average of the full reference sample. U.W. 88-63 was then Procrustes aligned to the average landmark configuration of the reference sample based on the subset of 673 landmarks.

The statistical procedure suggested by Gunz et al. (2009) was used to find initial estimates for the positions of the subset of 334 landmarks representing the predominantly missing medial condyle of U.W. 88-63. Using the reference sample, the subset of 673 landmarks representing the preserved portions of U.W. 88-63 and the subset of 334 medial condyle landmarks (predominantly missing on U.W. 88-63) were treated as two blocks of variables in a two-block partial least squares analysis. This procedure identified the statistical relationship between the two blocks of landmarks that maximized their correlation, and was used to estimate positions of the subset of 334 medial condyle landmarks for U.W. 88-63 based on the other 673 landmarks.

Next, final positions of the missing landmarks were estimated using geometric reconstruction (see Gunz et al. 2009). In this procedure, the subset of 334 missing landmarks representing the U.W. 88-63 medial femoral condyle was treated as sliding semilandmarks that were deficient in all three coordinate directions. The landmarks were slid to minimize bending energy of the thin-plate spline function of the U.W. 88-63 landmark configuration relative to two reference models: the Procrustes average human and average chimpanzee distal femur. Thus, the procedure resulted in two reconstructions, a human-based reconstruction and a chimpanzee-based reconstruction. The final reconstruction of U.W. 88-63 was determined as the weighted average of the human-based and chimpanzee-based reconstructions, which demonstrated the smallest surface distance between the portion of the medial condyle that was both preserved in U.W. 88-63 as well as reconstructed using the above procedure.

## HIGH RESOLUTION CT SCANNING AND SEGMENTATION PROTOCOLS

Delicate preservation of and proximity within matrix conjoining U.W. 88-97 (distal tibia), -98 (talus), and -99 (calcaneus) prevents their physical separation. In order to digitally separate the three elements for further study of obscured aspects of their anatomy (e.g., joint surfaces), the group of elements was scanned in the Palaeosciences Centre Microfocus X-ray CT facility of the University of the Witwatersrand. The facility has a Nikon Metrology XTH 225/320 LC dual source industrial CT system. The fossils were securely wrapped in standard bubble wrap to prevent movement during scanning and to protect them from being

damaged by contacting the walls of the sample holder (i.e., an acrylic container with an external diameter of approximately 86mm and a wall thickness of 1.5mm). The bubble-wrapped bundle was placed inside the container, which was secured with beeswax to the rotating sample platform of the scanner. Strips of Styrofoam were used to further secure the specimen inside the container, and prevent movement artifacts.

The following scan parameters were used—130 kV; 390  $\mu$ A; 4000 projections, where each projection represented the average of three frames (i.e., a shuttling setting of 3 was used); 2 frames per second acquisition time; and 1.2mm copper filtration. An isotropic voxel size of 57.1 $\mu$ m was achieved. An automated protocol in proprietary software—CT Pro version 2.2 service pack 5 (Nikon Metrology NV 2011)—was applied to projections in order to correct beam hardening (setting 2), after which the same software was used to reconstruct projections into a 32-bit float volume data file (.vol). The resultant volume file was imported into Avizo Fire 8.0 (FEI Visualization Sciences Group, Méri-gnac cedex-France 2013) for segmentation using facilities in the Virtual Imaging in Palaeontology (VIP) laboratory of the University of the Witwatersrand.

In order to digitally separate the three elements, segmentation was necessary. This procedure transpired as follows. First, an Edit New Label Field module was connected to the .vol file. Next, the combined use of magic wand and brush tools permitted selecting and assigning voxels in the image data set representing the elements to three respective materials. The assignment of voxels to each material was verified in three orthogonal views. Once labels for an element were finalized, a Generate Surface module was connected to the labels file (.am). A surface rendering of a material was generated from the .am file using an unconstrained smoothing setting of 5. Separate surface renderings for each element were saved as Big Endian STL files for further analyses using landmarks and a geometric morphometric approach.

## GEOMETRIC MORPHOMETRICS METHODOLOGY

### Talus

The extant talus sample consists of *Homo sapiens* (n=91), *Gorilla gorilla* (n=42), *Pan troglodytes* (44), *Pan paniscus* (n=15), and *Pongo pygmaeus* (n=43), housed in the Dart Collection (University of the Witwatersrand, South Africa), American Museum of Natural History (New York, USA), Smithsonian Institution Museum of Natural History (Washington D.C., USA), Yale Peabody Museum (New Haven, CT, USA), Powell Cotton Museum (Birchington, Kent, UK) Natural History Museum (London, UK), and the Royal Museum for Central Africa (Tervuren, Belgium). All non-human specimens were adult wild-shot individuals free of noticeable pathologies. The fossil sample consists of *Australopithecus sediba* (U.W. 88-98), *Au. afarensis* (A.L. 288-1 and A.L. 333-147), *Au. africanus* (?) (StW 88), *Homo habilis* (?) (OH 8), *H. floresiensis* (LB 1), *H. naledi* (U.W. 101-148 and -1417), and

**TABLE 3. TALAR LANDMARKS.**

<b>Trochlea</b>	1. Most distal point of trochlear groove.
	2. Most distal point of contact between the medial malleolar facet and the trochlear surface.
	3. Most dorsal point on the medial facet margin.
	4. Most proximal point of contact between the medial malleolar facet and the trochlear surface.
	5. Most proximal point of the trochlear groove.
	6. Most proximal point of contact between the lateral malleolar facet and the trochlear surface.
	7. Most dorsal point on the lateral facet margin.
	8. Most distal point of contact between the lateral malleolar facet and the trochlear surface.
	9. Most dorsal point on the trochlear groove.
	10. Most distal point on the medial malleolar facet.
	11. Most plantar point on the medial malleolar facet.
	12. Most distal point on the lateral malleolar facet.
	13. Most plantar point on the lateral malleolar facet.
	14. Deepest (most medial) point on the lateral malleolar facet, between landmarks 14 and 7.
<b>Proximal calcaneal facet</b>	15. Most disto-lateral point.
	16. Most lateral point.
	17. Most proximo-lateral point.
	18. Deepest (most dorsal) point on the proximal facet margin.
	19. Most proximo-medial point.
	20. Most medial point.
	21. Most disto-medial point.
	22. Deepest (most dorsal) point on the distal facet margin.
	23. Deepest (most dorsal) point of the facet.
<b>Head/navicular facet</b>	24. Most dorsal point.
	25. Most plantar point.
	26. Most medial point.
	27. Most lateral point.
	28. Most distal point.
	29. Most lateral point of contact between the navicular facet and the distal calcaneal facet.

a talus from Koobi Fora, Kenya (KNM-ER 1464) which is most likely to belong to either *Homo* or *Paranthropus*. Landmarks were used according to definitions by Harcourt-Smith (2002) and are listed in Table 3. U.W. 88-98 has some erosion along the lateral and plantar tip of the fibular facet. The missing bone was reconstructed with clay. Given how little bone is missing, we regard the estimated landmarks to have been reconstructed with high certainty.

### Calcaneus

Measurements were taken at the American Museum of Natural History (New York, NY) on the following extant species: *Homo sapiens* (n=32), *Gorilla gorilla* (n=16), *Gorilla beringei* (n=1), *Pan troglodytes* (n=12), *Pan paniscus* (n=1), and *Pongo pygmaeus* (n=4). The modern human sample included four small-bodied individuals, three from the Andaman Islands and one from a small-bodied population from the

Democratic Republic of Congo. Fossil specimens included casts of *Australopithecus afarensis* (A.L. 333-8 and A.L. 333-55), and *Australopithecus sediba* (U.W. 88-99).

All specimens were held in place using museum putty. Landmarks were recorded using a microscribe and the software packages MicroScribe Utility Software (v.5.1) and Microsoft Excel. Landmark locations are listed in Table 4. It was not possible to record every landmark on each of the fossil specimens. Landmarks 1 and 2 were estimated on U.W. 88-99. Landmark 1 was estimated based on the preservation of a slight divot in the cuboid facet. Landmark 2 was estimated by using preserved edges of the cuboid facet to estimate this point. It was not possible to include landmarks 1–8 on A.L. 333-8 and A.L. 333-55 due to damage to the specimen.

Calcaneal and talar landmarks were analyzed in *morphologica* 2.5 (O’Higgins and Jones 1998). Datasets were

TABLE 4. CALCANEAL LANDMARKS.

<b>On the cuboid facet on the distal end of the calcaneus.</b>	1. Most proximal point of articulation with cuboid beak.
	2. Most medial point of the facet.
	3. Most superior point of the facet.
	4. Most lateral point on the dorsal edge of the facet.
	5. Most plantar point of the facet.
<b>On the anterior talar facet of the calcaneus.</b>	6. Most proximal point on the midline of the facet.
	7. Most plantar point on the midline of the facet.
	8. Most distal point on the midline of the facet.
<b>On the posterior talar facet of the calcaneus.</b>	9. Most proximal point on the long axis of the posterior talar facet.
	10. Most distal point on the long axis.
	11. Lateral point that dictates the short axis at the widest point.
	12. Intersection point between the two axes.
<b>On the lateral side of the calcaneus.</b>	13. Medial point that dictates the short axis at the widest point.
	14. Most lateral point on the peroneal tubercle.
<b>On the posterior tuberosity of the calcaneus.</b>	15. Most lateral point on the posterior tuberosity in line with the retrotrochlear eminence.
	16. Most superior point on the tuberosity through the long axis.
	17. Most inferior point on the MPP through the long axis.
	18. Most lateral point on the border between the middle and inferior facet of the tuberosity.
	19. Most medial point on the border between the middle and inferior facet of the tuberosity.
	20. Most distal point on the plantar surface of the posterior tuberosity (i.e., the beak).

subjected to a Generalized Procrustes Analysis followed by a Principal Component Analysis (PCA).

## RESULTS

Presented below are the anatomical descriptions, comparative assessments, and brief functional remarks for the lower limb fossils recovered from Malapa, South Africa (2008–2011). For each fossil, the state of preservation is presented first, followed by a detailed morphological description. Surface scans of the fossils are available online ([www.morphosource.org](http://www.morphosource.org)).

### FEMUR OF MH1

#### **U.W. 88-4/5/39: Partial Right Proximal Femur**

U.W. 88-4, U.W. 88-5, and U.W. 88-39 are conjoining pieces of the right, juvenile, femur of MH1, preserving the most proximal 93.5mm of the femur from a break in the proximal shaft to the epiphyseal surface of the femoral head (Figure 1). U.W. 88-4 is the largest piece, preserving most of the metaphyseal surface of the head, the neck, metaphyseal surfaces for the greater and lesser trochanters, and a part of the proximal shaft. U.W. 88-5 is a 48.1mm piece of the proximal shaft that cleanly joins with U.W. 88-4 anteriorly and medially. U.W. 88-39 is the inferior aspect of the metaphyseal surface of the head, which also adjoins with U.W. 88-

4. Epiphyses of the femoral head, greater trochanter, and lesser trochanter have not been recovered. The distal part of the metaphysis for the lesser trochanter is sheared away along a break in the shaft that proceeds proximomedially to distolaterally. U.W. 88-5 adjoins cleanly with the anterior and medial surfaces of U.W. 88-4, but there is approximately 7mm of the PD part of the femoral shaft missing laterally and posteriorly. Medially, there is a large crack running the length of this part of the shaft, enlarging distally.

The metaphyseal plate of U.W. 88-4 and U.W. 88-39 conjoin, but there is some erosion around the perimeter, making it difficult to estimate the size of the complete metaphyseal plate, and thus the femoral head diameter. Estimates have ranged from 29.8mm (Berger et al. 2010) to 33mm (DeSilva et al. 2013). Here, we adopt a femoral head diameter of 32.5mm (see Holliday et al. 2018).

The neck is relatively long, with the biomechanical neck length estimated as 60.3mm based on the dimensions of the MH2 proximal femur. This measurement assumes that the missing greater trochanter of MH1 would have been australopith-like in lacking the lateral flare that characterizes *Homo* greater trochanters (Napier 1964). Posteriorly, the length of the neck from the intertrochanteric crest to the edge of the epiphyseal surface for the head is 28.9mm. Based on this dimension, the neck is elongated, as often characterizes *Australopithecus* proximal femora and



Figure 1. Right proximal femur U.W. 88-4/5/39. In the upper left box, the proximal femur from MH1 U.W. 88-4 is situated along the top row in anterior and posterior (top left and right) views, while in the bottom row (left to right) superior, medial, and lateral views are illustrated. In the upper right box is U.W. 88-4 articulated with U.W. 88-5, and shown in anterior view. In the bottom right box is U.W. 88-5 illustrated in (from left to right): medial, posterior, and lateral views. The bottom left box illustrates U.W. 88-39 (epiphyseal surface) in inferomedial view on the left and the sheared lateral surface that contacts U.W. 88-4 on the right (scale bar=1cm for each of the panels).

functionally improves mechanical advantage of the lesser gluteals during the single-legged support phase of walking (Lovejoy et al. 2002). The neck is moderately compressed anteroposteriorly, measuring 23.3mm superoinferiorly and 17.1mm anteroposteriorly. Anteriorly, the neck is smooth and there is no evidence for an intertrochanteric line, an anatomy absent from some hominin femora, but present in over 95% of modern humans (Lovejoy et al. 2002). The neck tapers superiorly into a strong bar of bone that runs along the superoanterior edge of the top of the femoral neck. The epiphyseal surface of the head is angled anteromedially to posterolaterally in superior view. Posteriorly, a weak, but palpable obturator externus groove runs across the neck.

The neck shaft angle is approximately  $110^{\circ}$ – $115^{\circ}$ , near the average for *Australopithecus*, but lower than that found in both modern humans and modern apes (Aiello and

Dean 1990). The metaphyseal surface for the greater trochanter is large, measuring 29.6mm AP, and 31.3mm ML along the elongated anterior border, while only 21.3mm ML along the shorter posterior border. It is thus asymmetrical, angling more anteriorly than posteriorly. To what degree this anatomy is indicative of femoral anteversion is unclear until the more complete left MH1 femur (currently still encased in hardened matrix) is prepared and studied. In anterior or posterior view, the trochanteric metaphyseal surface is horizontal and on the same plane as the femoral neck (Figure 2), which is similar to the condition found in modern apes and in *Au. afarensis* (Ward et al. 2012), and unlike the more inferiorly projecting lateral part of the trochanteric metaphyseal surface found in *Homo*, including *Homo naledi* (Marchi et al. 2017). These different anatomies of the greater trochanter apophysis may be related to the

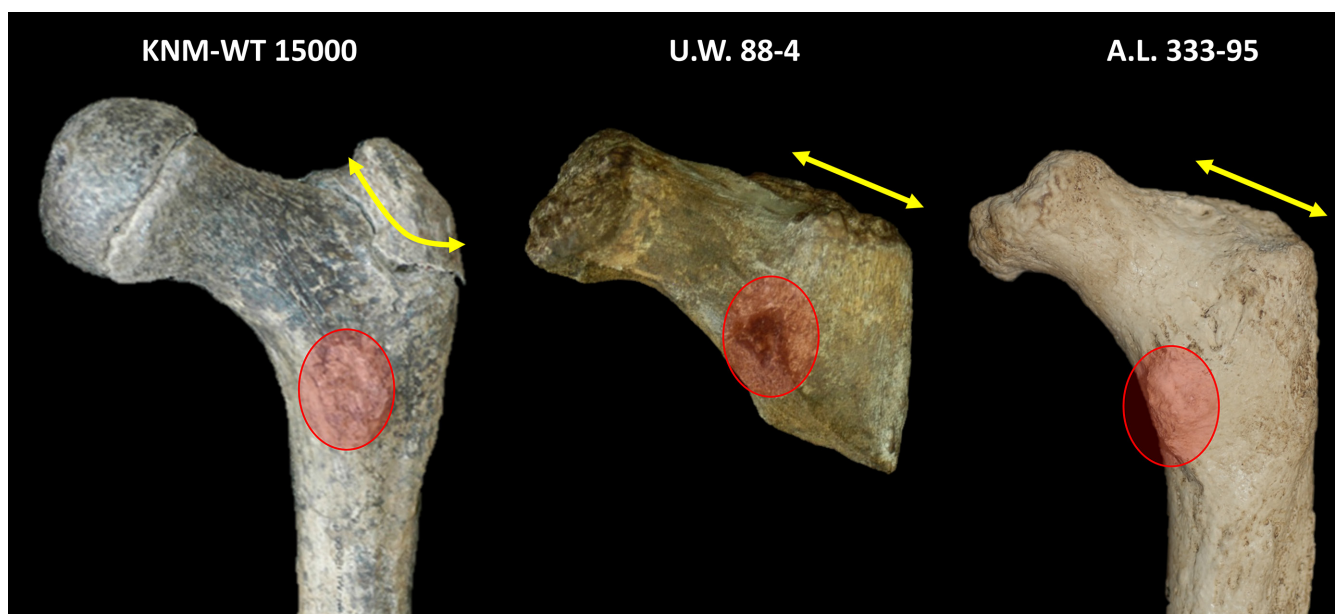


Figure 2. KNM-WT 15000 (left), U.W. 88-4 (middle), and A.L. 333-95 (right) have been scaled to roughly the same size (by equalizing the distance from the margin of the capital epiphysis and the lateral border of the proximal shaft), mirrored to the right side, and positioned so that the inferior extent of the metaphysis for the femoral head is in the same horizontal plane. The femoral shaft is oriented as close to vertical as possible. Notice in both U.W. 88-4 and in A.L. 333-95 that the metaphysis for the greater trochanter (yellow arrows) is relatively more horizontal, paralleling the long axis of the femoral neck. KNM-WT 15000, however, possesses a greater trochanter metaphysis (and matching epiphysis) that angles inferolaterally. These different anatomies of the greater trochanter apophysis may be related to the more distal and extensive insertion of the lesser gluteals onto the proximal femur of australopiths (Ward et al. 2012). Also note in this image the relatively proximal position of the lesser trochanter (denoted by the red circle) in *Au. sediba*.

more distal and extensive insertion of the lesser gluteals onto the proximal femur of australopiths (Ward et al. 2012).

The distal edge of the metaphyseal surface for the greater trochanter is close to the surface for the lesser trochanter—the two are only 18mm apart and bridged by an elevated intertrochanteric crest. The lesser trochanter is therefore quite proximally positioned relative to the femoral head, which may functionally imply a shorter lever arm for the *M. iliopsoas* (see Figure 2). An adult proximal femur with a preserved lesser trochanter will help clarify *M. iliopsoas* function in *Au. sediba*. The metaphyseal surface for the lesser trochanter is positioned along the medial border of the posterior aspect of the bone. Below the trochanter, the shaft is platymeric, measuring 26.4mm ML and 20.3mm AP. Laterally, there is a roughened gluteal tuberosity, or third trochanter, starting at about the same level as the lesser trochanter and proceeding distally until it is interrupted by the break in the shaft. The anterior and posterior parts of the shaft are convex.

Along the lateral aspect of U.W. 88-5, just inferior to the gluteal tuberosity is a well-developed hypotrochanteric fossa marking the insertion of *M. gluteus maximus*. While this anatomy is human-like, it is most likely primitive given similar femoral architecture in *Orrorin*, *Ardipithecus*, and Miocene apes (Almecija et al. 2013; Lovejoy et al. 2009b).

## FEMUR OF MH2

### U.W. 88-51: Right Proximal Femur

U.W. 88-51 is an adult right proximal femur from MH2, preserving 50.8mm ML of the femoral head and neck (Figure 3). The head is damaged anteriorly and medially. Anteriorly, 18.5mm SI is missing from the articular surface of the femoral head. This damage proceeds medially and tapers to 12.4mm SI near the center of the head (in anterior view), and expands again to 19.8mm SI near the medial most region of the head. There is damage to the most anterior part of the fovea. Posteriorly, the head is very well-preserved. The anterior portion of the neck is also damaged, save for an 8.7mm projection of bone along the inferomedial aspect of the neck. There is a small piece of bone that has been displaced superiorly and is cemented to the superior aspect of the neck. The posterior surface of the femoral neck is well preserved, save for some minor exfoliation of cortical bone. The break in the femoral neck is oblique, such that posterior aspect of the neck projects more laterally than the medial side of the neck.

The maximum SI head diameter is 32.7mm. As in MH1, the neck is anteroposteriorly compressed, measuring 22.4mm SI at a minimum and approximately 16.6mm AP perpendicular to the SI minimum, though damage to the anterior neck precludes a more definitive measure. The

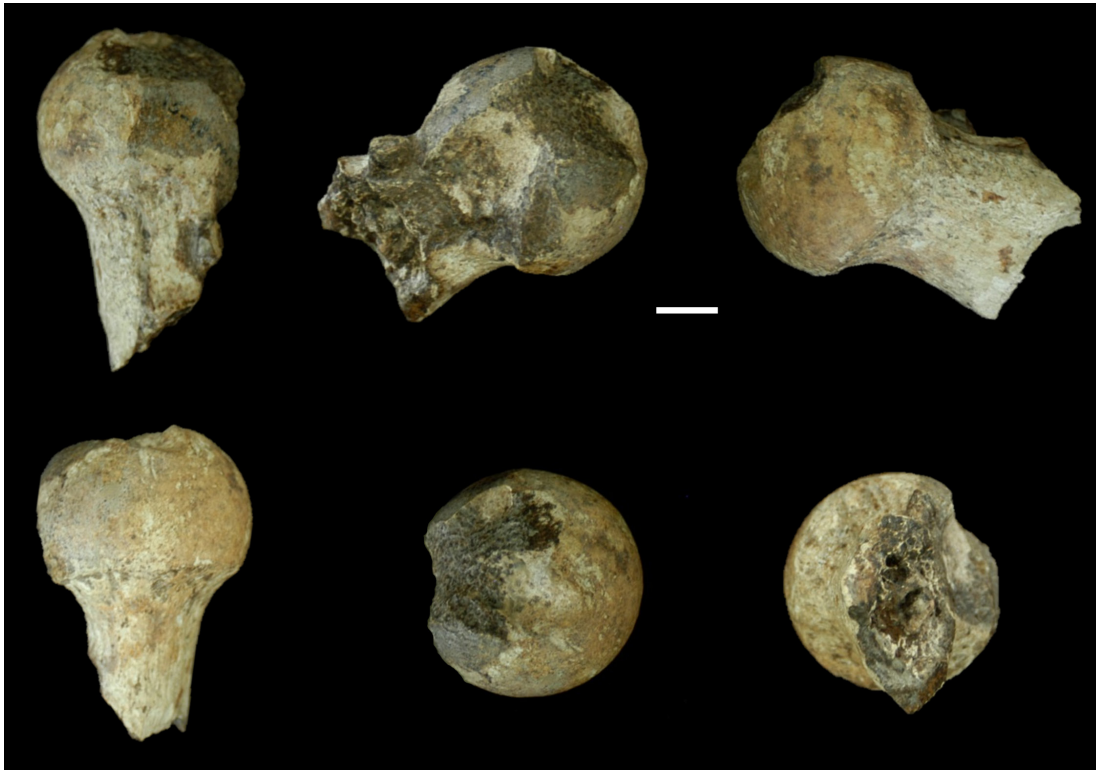


Figure 3. Right proximal femur U.W. 88-51 in (top left to right) superior, anterior, and posterior views. Bottom row (left to right): inferior, medial, and lateral views (scale bar=1cm).

head is globular, with the fovea located just inferior and posterior to its center. Fovea dimensions are approximately 10mm AP and 7mm SI. Viewed superiorly, the articular surface of the head has a v-shape, and is angled in such a way to elongate the anterior aspect of the head, taper at the midpoint, and then elongate the posterior aspect of the head (though not as great as the anterior). The head grades into the neck superiorly, extends slightly (2.8mm) onto the neck posteriorly, and separates more abruptly from the neck as one moves inferiorly. There are several foramina along the inferior aspect of the head-neck junction. The superior aspect of the neck begins to rise superiorly just prior to the break, allowing for a notch depth measurement (following method of Lovejoy et al. 2002) of about 14.2mm. Most laterally along the femoral neck is a small indentation that may be the groove produced by the obturator externus tendon, though there is some flaking of the cortex here and thus this anatomy is uncertain. The break in the femoral neck is jagged, but reveals a thicker cortex inferiorly than superiorly. Taken orthogonally to the neck at its base, a  $\mu$ CT slice reveals thicker cortex inferiorly (~4.7mm) than superiorly (~2.2mm). This uneven distribution of cortical bone in the femoral neck is characteristic of bipedal hominins (Lovejoy et al. 2002; Ohman et al. 1997), though there appears to be variation in different australopiths (Ruff and Higgins 2013). Relative to the diameter of the femoral head, the femoral neck is moderately SI tall, which overlaps the morphology found in *Homo* and in *Australopithecus* (Figure 4).

#### U.W. 88-53: Partial Shaft Of Right Femur

U.W. 88-53 is a small (52.8mm maximum PD) piece of femoral shaft from the right femur of MH2 (Figure 5). Breaks in the shaft are oblique both proximally and distally such that only 19.2mm PD of the anterior part of the bone is preserved, but heavily eroded.

Laterally, the shaft is slightly concave, whereas the posteromedial part of the shaft is flat. Posteriorly, a pilaster is present, giving the shaft a tear-drop shape in cross section, even though the maximum dimensions are even (20.4mm AP, 20.3mm ML). There is a low, faint linea aspera comprised of two, raised and parallel lines. At the most distal aspect of the bone, the lines diverge and the most superior part of the medial supracondylar line is detectable. Given these anatomies, this piece is from the more distal part of the femoral shaft, though it is does not cleanly contact U.W. 88-63, the distal femur from MH2.

#### U.W. 88-63: Right Distal Femur

U.W. 88-63 is a well-preserved right distal femur from MH2 (Figure 6; Table 5). It is 86.7mm long from the proximal most point of the oblique break through the shaft to the distal ends of the condyles. The bone is 54.5mm ML wide from the lateral epicondyle to the most medial aspect of the broken medial side—a minimum biepipicondylar breadth. This value is probably near the true bi-epicondylar breadth given that in humans and apes the medial epicondyle usually does not extend medially much more than the medial extent of the condyle and there is enough bone preserved

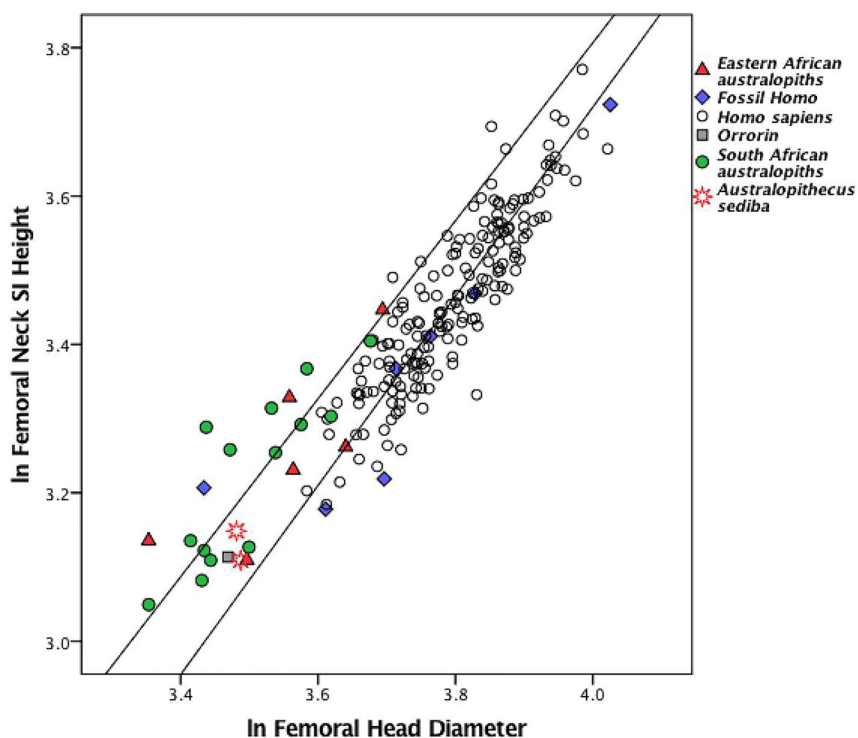


Figure 4. Modeled after Ruff and Higgins (2013). The superoinferior height of the femoral neck is elevated relative to the size of the femoral head in australopiths. This may be an adaptation for resisting high SI bending forces in the coronal plane on a long femoral neck incurred during the support phase of walking (Ruff and Higgins 2013). MH1 and MH2 (FHD 32.5mm and 32.7mm respectively) have SI shorter femoral necks than many australopiths of comparable size, though they remain within the range of australopiths. Fossil Homo is human-like with the exception of LB1, which is the blue diamond to the far left of the graph. Human femora ( $n=183$ ) and fossil hominins from sources listed in DeSilva et al. (2013) and Ward et al. (2015). Reduced major axis regression line drawn through the human data ( $R^2=0.80$ ;  $m=1.275$ ;  $y=-1.38$ ), and the australopith data ( $R^2=0.66$ ;  $m=1.2$ ;  $y=-0.9932$ ). The regression lines are remarkably parallel, meaning that for a given femoral head diameter, australopiths have SI tall necks as found by others (Ruff and Higgins 2013).

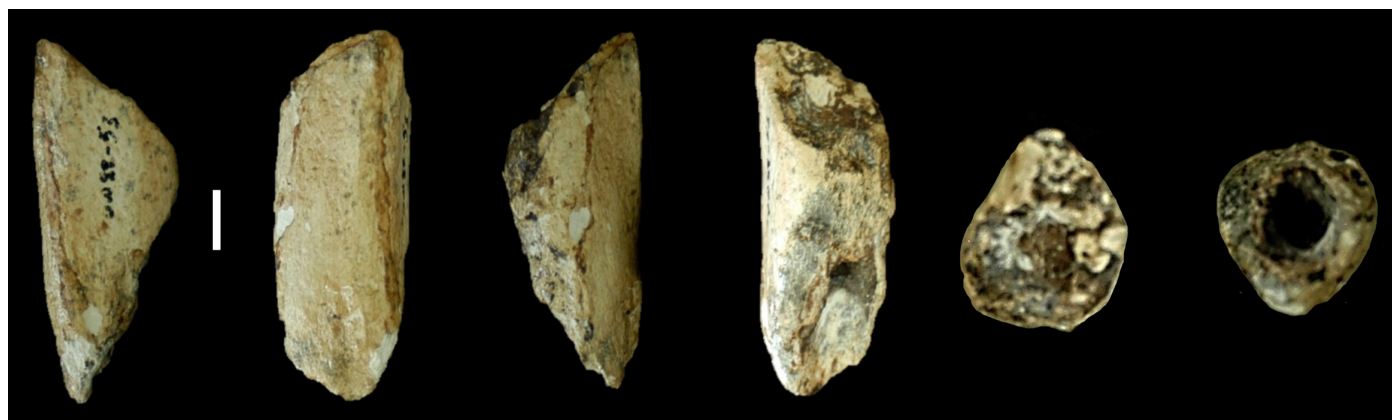


Figure 5. Right femoral shaft U.W. 88-53 in lateral, posterior, medial, and anterior views. To the right of the anterior view are cross sections of the proximal (left) and distal (right) breaks through the shaft (scale bar=1cm).

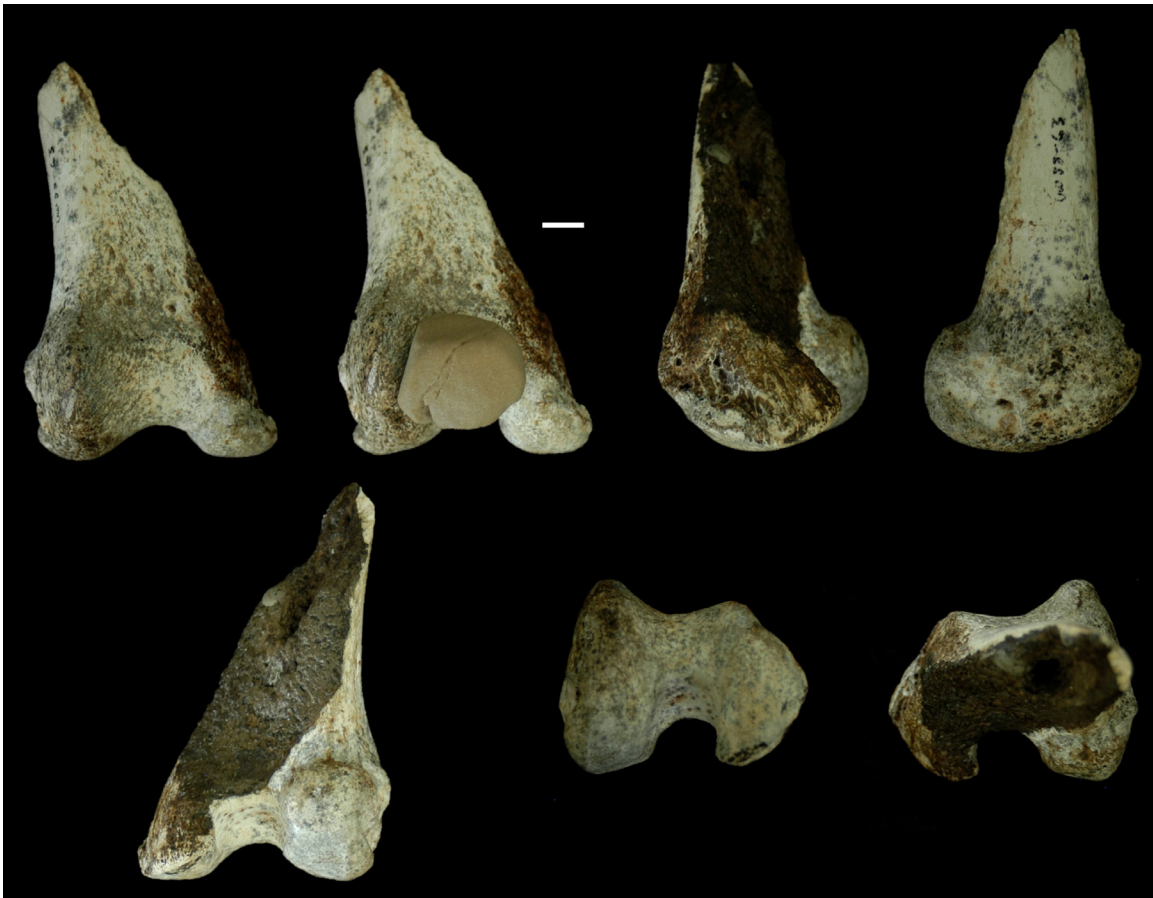


Figure 6. Right distal femur U.W. 88-63. Top row: Anterior, anterior with patella, medial, and lateral views. Bottom row: posterior, inferior, and superior views. Notice in anterior view that the patella has a strong superomedial angulation resulting in a contact with the high lateral lip. The exceptionally high lateral lip is visible in inferior and superior views. In anterior and posterior views, the bicondylar angle (estimated as  $\sim 9^\circ$ ) can be seen (scale bar=1cm).

on U.W. 88-63 to define a medial border to the medial condyle. The posteromedial part of the bone has been sheared away and there is erosion along the medial aspect of the medial condyle, but the lateral condyle, patellar articular surface, anterior portion of the shaft, and some of the medial condyle are all well-preserved.

Anteriorly, there is a sustrochlear hollow just superior to the patellar surface, which provides evidence of contact with the patella in a fully extended position (Tardieu 2010). The patellar surface is quite well-preserved and is strongly concave ML and gently convex PD. The intercondylar notch is tall and relatively narrow, measuring 21.8mm PD and 13.7mm ML. A clear impression for the anterior cruciate ligament is present on the lateral aspect of the intercondylar notch, indenting into the lateral condyle. An impression for the posterior cruciate ligament can be palpated along the anterior edge of the medial intercondylar notch. The anterior aspect of the intercondylar notch is pitted with multiple vascular foramina.

The lateral condyle is very well-preserved. It measures 44mm AP and is AP-elliptical in lateral view. There is a small impression for the anterior horn of the meniscus 20.9mm from the most posterior aspect of the lateral con-

dyle, just medial to the termination of the articular surface of the lateral condyle and just anteroinferior to the popliteal groove. The proximal portion of the lateral condyle is dominated by a projecting lateral patellar lip, which rises well above the patellar articular surface. The extension of the lateral lip is not a function of overall anterior expansion of the patellar surface, as is found in *Homo*, and is restricted to the lateral side (Figure 7). Because the medial condyle is damaged, it was difficult to orient the bone to get an accurate lateral patellar lip angle. Subsequent to the new reconstruction (Figure 8), the original measurement of the lateral patellar lip angle should be lowered from  $31.3^\circ$  to  $26.5^\circ$ . Thus, while our original assessment of the lateral patellar lip remains unchanged in that it is exceptionally high, quantification of this anatomy is not quite as extreme as was originally suggested (DeSilva et al. 2013). Also, because the medial condyle is sheared off posteriorly, a condylar height is difficult to measure. It is estimated as no less than 37.4mm AP. The medial articular surface forms a condylar boss that angles laterally as the articular surface reaches its most anterior aspect. In inferior view, the articular aspect of the lateral condyle is a maximum of 16.1mm ML while the medial condyle is wider, 18.2mm ML. Compared with the

TABLE 5. COMPARATIVE METRICS OF THE HOMININ DISTAL FEMUR.

Specimen	Bicipondylar breadth	Lateral condyle height	Lateral condyle width	Medial condyle height	Medial condyle width	Intercondylar notch height	Intercondylar notch width	Maximum height/width ratio	Lateral condyle width/height	Source
U.W. 88-63	54.5 <sup>3</sup>	44	16.1	37.4 <sup>1</sup>	18.2	21.8	13.7	80.1 <sup>3</sup>	36.6	This study
A.L. 129-1	56.5	39.9	18.8	40.3	20.3	19.6	14.5	70.1	47.1	Ward et al. (2012); cast measurements
A.L. 288-1	56.7	40.3 <sup>2</sup>	-	-	-	-	-	71.1	-	Ward et al. (2012); cast measurements
A.L. 333-4	72.2	50.2	-	51.5	-	29.6	15.6	69.3	-	Lovejoy et al. (1982)
A.L. 333-w56	-	48.3	-	-	-	-	-	-	-	Ward et al. (2012)
TM 1513	55.7 <sup>3</sup>	44	21.3	45	22	13	12.2	79 <sup>3</sup>	48.4	This study
Sfs 34	62.7	45.1 <sup>1</sup>	20.6 <sup>2</sup>	51.7 <sup>2</sup>	21.9	16	16.5	71.2	47.9	This study
SW 129	-	47.3	20.8 <sup>1</sup>	-	-	-	-	-	44 <sup>2</sup>	This study
SW 318	-	41	18.5	-	-	-	-	-	45.1	This study
TM 3601	48.1	34	16.6	-	19.2	-	-	70.7	48.8	This study
SK 1896	68.6 <sup>4</sup>	52	21.4	52.3	27.1	-	-	-	41.1	This study
KNM-ER 993	66.7 <sup>1</sup>	40.7	-	-	-	21.22	22.92	61 <sup>1</sup>	-	This study
KNM-ER 1472	67.1	50.8	21.7	50.2	23.4 <sup>2</sup>	25.5	19.4	75.7	42.7	This study
KNM-ER 1481	68.7	59.4	25.5	58.8	23.1	24.3	19.7	86.5	42.9	This study
KNM-ER 1592	79.2	53.1 <sup>2</sup>	28 <sup>2</sup>	55.3 <sup>2</sup>	-	24.9 <sup>2</sup>	-	67.1 <sup>1</sup>	52.7 <sup>2</sup>	This study
KNM-ER 3951	-	48.9 <sup>1</sup>	20.8 <sup>2</sup>	50.8	21.6 <sup>2</sup>	29.9	18.1	-	42.5 <sup>2</sup>	This study
U.W. 101-215	57 <sup>2</sup>	-	20.6 <sup>1</sup>	-	18.8 <sup>1</sup>	-	19.3	-	-	Marchi et al. (2017)
Modern human (n=102)	-	62.1±4.1	27±2.7	59.2±4.5	25.6±2.4	-	21.2±3.3	-	43.4±3.1	This study

<sup>1</sup>Minimum measurements that underestimate the actual value.<sup>2</sup>Estimates that approximate the actual value.<sup>3</sup>Maximum values for which the true value can be no greater.<sup>4</sup>Measured value on a complete, but distorted fossil.

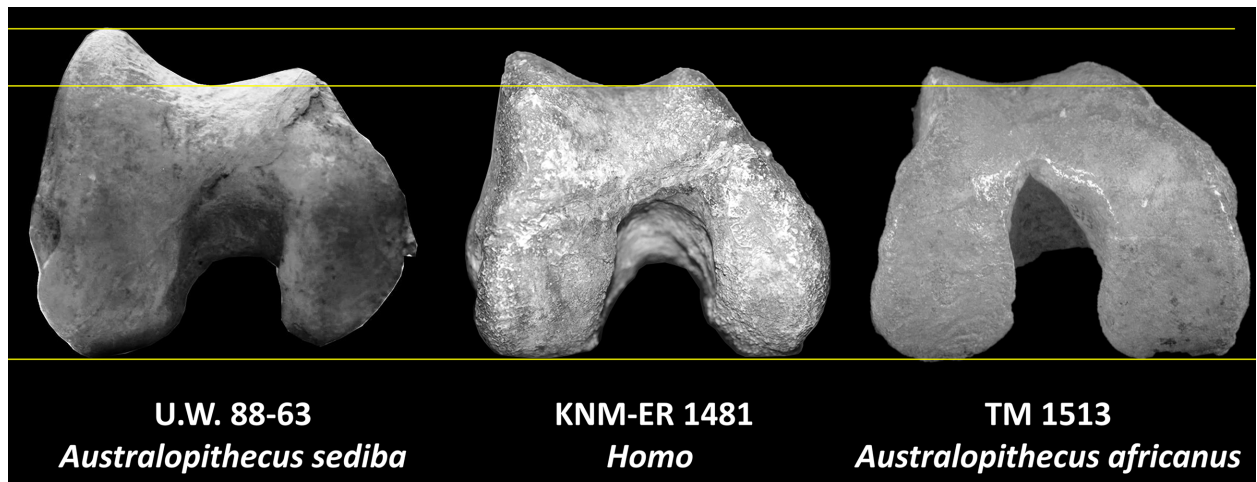


Figure 7. In DeSilva et al. (2013), the elevated lateral lip of U.W. 88-63 was visualized after orienting the distal femur as recommended by Lovejoy et al. (2007), and size-standardizing the bone by epicondylar width. Here, we standardize it by equalizing the vertical distance between the most posterior points of the lateral condyles and the deepest part of the patellar groove in inferior view (the bottom two yellow lines). In this view, KNM-ER 1481 (*Homo* sp.) has a higher lateral lip than TM 1513 (*Au. africanus*), but U.W. 88-63 has an extremely high lateral lip. Height of the medial patellar rims do not appreciably differ between the three femora. We have argued elsewhere that the elevated lateral lip of U.W. 88-63 could facilitate patellar retention during excessive medial rotation of the femur, as might occur during a hyperpronating gait, or in the absence of a well-developed *M. vastus medialis obliquus*. U.W. 88-63 has been positioned to account for the reconstructed medial condyle (see Figure 8).

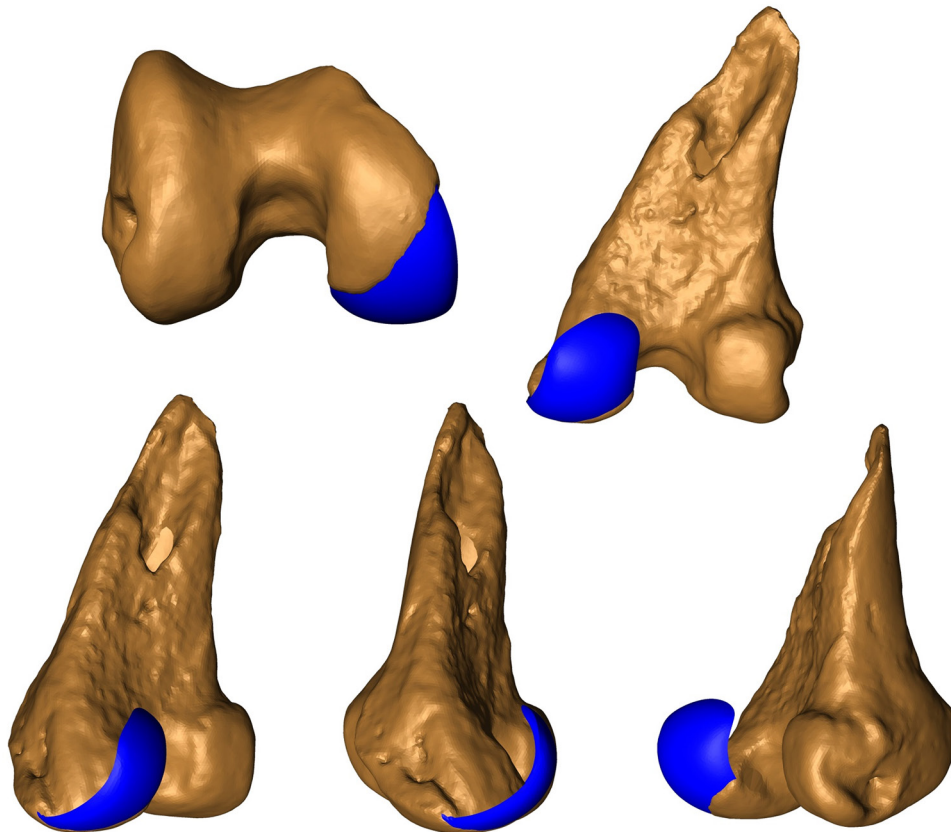


Figure 8. Digitally reconstructed distal femur of MH2 (U.W. 88-63) illustrated along the top (left to right) in inferior and posterior views, and along the bottom (left to right) in posteromedial, medial, and posterolateral views. The preserved anatomy of U.W. 88-63 is shown in gold, while the reconstructed medial condyle is in blue. See materials and methods for approach to reconstructing the medial condyle.

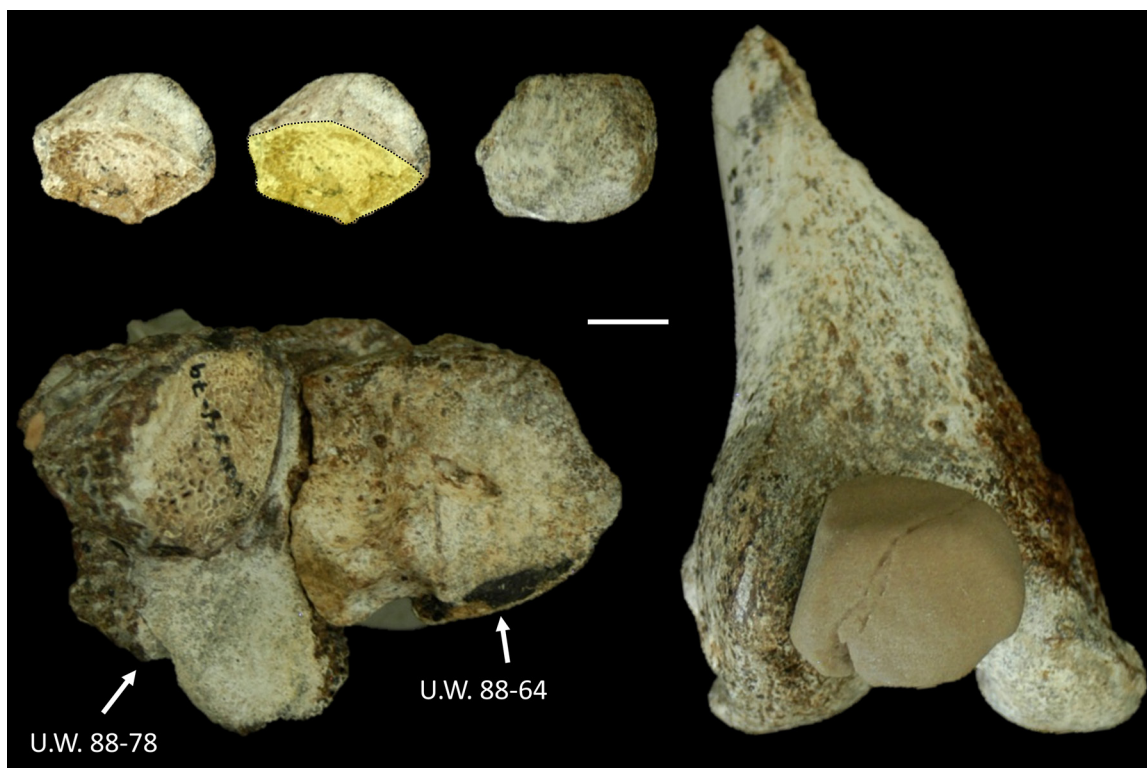


Figure 9. Upper left illustrates the right patella (U.W. 88-100) in posteromedial view; to the immediate right is the same image highlighting and outlining the clean section through bone. To the right of the previous image is U.W. 88-100 in anterior view. Bottom left is U.W. 88-64 and U.W. 88-78 articulated together to form the proximal tibial plateau. Adhered to U.W. 88-78 is the lateral half of the right patella of MH2—U.W. 88-79. Both pieces were  $\mu$ CT scanned and digitally reconstructed by aligning individual trabeculae. The resulting patella is illustrated elsewhere (DeSilva et al. 2013). Along the far right, a 3D printout of the digitally reconstructed MH2 patella is articulated within the patellar groove of the U.W. 88-63 femur. The distolateral to proximomedially oriented fracture delineates the separation between U.W. 88-79 (to the left) and U.W. 88-100 (to the right). Notice the diagonally-oriented lateral edge of U.W. 88-79, which rests against the high lateral lip of U.W. 88-63 (scale bar=1cm).

mediolateral width of the lateral tibial condyle (U.W. 88-64; minimum of 21.3mm), the lateral femoral condyle is quite narrow. At only 75.6% (minimum) the width of the lateral tibial condyle (U.W. 88-64), the *Au. sediba* knee falls at the far low end of the human range (average  $88\% \pm 6.1\%$ ; minimum 75.4%). A smaller lateral femoral condyle relative to the lateral tibial condyle would permit greater rotation of the femur (around a relatively less mobile medial condyle), knee mechanics which have been proposed for *Au. sediba* (DeSilva et al. 2013). In inferior view, the medial condyle extends anteriorly much more than the lateral: 30.1mm AP (minimum) medially versus only 20.9mm AP laterally.

On the lateral side of the distal femur, there is a deep pit marking the origin of *M. popliteus*, which is 7.9mm PD, and a popliteal groove, which extends 20.5mm posteriorly. The pit marking the origin of *M. popliteus* is bordered anteriorly by an elevated bony wall. There is a well-developed tubercle for the lateral collateral ligament, posterior to which is a small impression for the lateral head of the gastrocnemius. The bicondylar angle is approximately  $9^\circ$ , which is within the range of modern humans, but ultimately low for an australopith.

## PATELLA OF MH2

### U.W. 88-79/100: Right Patella

U.W. 88-79 and U.W. 88-100 combine to form the almost complete right patella of MH2 (Figure 9; Table 6). U.W. 88-100 is a 23.4mm PD, 21.9mm ML fragment comprising the majority of the medial and distal portions of the patella, including its apex. It is sheared away from U.W. 88-79 with a break running proximomedially to distolaterally across the entirety of the bone. U.W. 88-79 has been digitally segmented from  $\mu$ CT scans, and rejoined to U.W. 88-100 by aligning not only the clean articulations along the broken surfaces, but by also aligning individual trabeculae that bridge the break (see DeSilva et al. 2013). U.W. 88-79 preserves much of the lateral and proximal portions of the patella, including its base. The conjoined pieces form a patella that is almost complete, save for a small piece of the distolateral apex.

The patella is quite small. The 3D printout of the digitally segmented portion of the bone (U.W. 88-97), conjoined with U.W. 88-100 is 27.1mm ML. The complete patella is 24.7mm SI, which is probably just short of the actual height. Maximum AP width of the patella is 13.1mm. The base

TABLE 6. COMPARATIVE METRICS OF HOMININ PATELLAE.

Specimen	Species	Mediolateral width	Proximodistal height	Anteroposterior thickness
U.W. 88-79/100	<i>Australopithecus sediba</i>	27.1	24.7	13.1
SKX 1084	<i>Australopithecus robustus</i>	30.1	-	13.3
U.W. 101-852	<i>Homo naledi</i>	-	-	18.3
U.W. 101-1404	<i>Homo naledi</i>	30	-	16.2
LB1/10 <sup>1</sup>	<i>Homo floresiensis</i>	30.5	~31.3	12.1
LB1/11 <sup>1</sup>	<i>Homo floresiensis</i>	30.9	33.3	12.3

<sup>1</sup>From Jungers et al. 2009b.

D3418 is a complete patella from Dmanisi (Lordkipanidze et al. 2007; Pontzer et al. 2010) but no linear measurements have been published.

is flat and smooth anteriorly. It deflects posteriorly, as is the case in human patellae. There are some small foramina along the superior border of the base. There is a small groove separating the foramina filled edge of the base, and a ridge that transitions to the anterior surface of the patella.

There are many vertical striations along the anterior aspect of the patella. The medial border of the patella is quite round. On the medial side, at the midpoint of the patella is a small tubercle, presumably for *M. vastus medialis*, with a small depression inferior to it. The patella lacks the strong medial projection of bone found in most modern human patellae. On the digital 3D printout, it can be seen that the lateral side of the patella is straight, angling from the base to the inferolateral corner, where it rounds to the apex. This straight edge is smooth, and contacts the lateral lip of U.W. 88-63 when the two are articulated. A complementary anatomy on the patella (flat lateral edge) combined with the high lateral lip suggest that the knee of U.W. 88-63 was not pathological and was well-adapted for patellar retention during internal rotation of the femur. There is no evidence for eburnation, as has been described for the Dmanisi knee (Pontzer et al. 2010). The apex is non-articular, and is pitted with many vascular foramina. It projects weakly and does not terminate in a point, as is often the case in human patellae. Rather, it is button-shaped, as are often patellae of apes.

The digital 3D printout reveals a posterior surface of the patella that is strongly convex mediolaterally, with a high central keel disproportionately separating the condylar facets medially and laterally. The medial side is slightly convex and can be articulated with the lateral aspect of the superomedial condyle in U.W. 88-63. Medially, the contact area for the femur grades into a flatter region mediolaterally and is slightly concave proximodistally for contact with the medial condyle during knee flexion. The lateral contact facet is strongly sloped and convex. The most protruding point of the posterior surface of the patella is located slightly lateral of the midline, making the medial facet area slightly larger than the lateral. A larger medial facet has also been noted for the Dmanisi patella (Lordkipanidze et al. 2007). In modern human patellae, the lateral facet is usually larger.

## TIBIA OF MH1

### U.W. 88-89: Partial Shaft Of Tibia

U.W. 88-89 is a 67.9mm piece of tibial shaft of MH1 (Figure 10), most likely from the right side. It is best placed near the midshaft based on comparisons with the more complete U.W. 88-21/40. It is broken obliquely on both ends such that the posterior aspect of the bone is longer than the anterior. There is a longitudinal crack that runs the length of the lateral side of the bone, distorting it slightly. The anterior surface has been damaged, with a very wide crack (~5.5mm) running its length.

The posterior surface is strongly convex. The lateral surface is flat proximally, but becomes more convex distally as a strong pillar of bone develops and progressively shifts anteriorly in more distal parts of the bone. The medial surface is flat. Proximally, the shaft cross section exposed by the break is mediolaterally compressed—23.4mm AP and 16.4mm ML. The more distal shaft cross section, by comparison, is more equivalent in dimensions—22.5mm AP and 18.7 ML. These dimensions are almost identical to comparable dimensions on U.W. 88-40.

## TIBIA OF MH2

### U.W. 88-64/78: Right Proximal Tibia

U.W. 88-64 and U.W. 88-78 are conjoining pieces of the right proximal tibia of MH2 (Figure 11; Table 7). U.W. 88-64 preserves the anterior half of the lateral condyle, the intercondylar eminence, and a portion of the anterior part of the plateau. U.W. 88-78 preserves the medial condyle and the medial aspect of the metaphysis. A part of the patella (U.W. 88-79) is adhered with matrix to the anteromedial portion of the plateau, obscuring that part of the condyle. Matrix also covers the medial portion of the plateau as well. There is erosion around the lateral side of the plateau, the posterolateral region of the plateau is not preserved at all, and none of the shaft is preserved. The posterior intercondylar area is only partially preserved, but the anterior intercondylar area is well-preserved. The metaphysis is poorly preserved and the shaft is absent.

The plateau measures a minimum of 54.4mm ML and



Figure 10. Tibial shaft U.W. 88-89 in (from left to right assuming specimen is from the right side): lateral, anterior, medial, and posterior views. To the far right are cross sections of the proximal and distal breaks through the bone (scale bar=1cm).

40.5mm AP. The medial condyle is flat AP and slightly concave ML. It is 39.3mm AP and approximately 22.1mm ML (the ML measurement is an estimate due to erosion along the medial border of the condyle). The lateral condyle is slightly convex anteroposteriorly, similar to the condition found in A.L. 129-1 and A.L. 288-1 (Johanson et al. 1982; Lovejoy et al. 1982), and not as anteroposteriorly convex as StW 514 (a presumed *Au. africanus*; Berger and Tobias 1996). The lateral condyle preserves 21.3mm ML. The lateral AP dimensions cannot be estimated because the posterior part of the lateral condyle is missing. The intercondylar eminence projects 6.2mm superior to the tibial plateau, and terminates in tibial spines that are 5.7mm apart from one another in a posteromedial to anterolateral direction. Compared to the condylar notch width (13.7mm), the spines are quite close together and yield an interspinal distance to intercondylar notch width ratio of 0.42, slightly higher (more human-like) than the ratio found in A.L. 129-1. This ratio is suggestive of elevated rotational capacity of the knee (Tardieu 1981), or alternatively (and more likely) a size-related anatomy (Aiello and Dean 1990) given the human-like ratio found in large-bodied gorillas. Relative to a coronal plane, the tibial spines are angled posteromedial to anterolateral. There is a pit in the anterior intercondylar area for the anterior cruciate ligament. The bone is broken almost exactly where the notch for the posterior lateral meniscus resides, however, there appears to be the beginnings of a notch in this area, suggesting the presence of a double insertion of the lateral meniscus.

Anterolaterally is a relatively flat and non-projecting Gerdy's tubercle marking the insertion of the iliotibial band, which helps stabilize the knee in humans. This band is well-developed in modern humans, more so than in other apes (Kaplan 1958), which lack the prominent insertion into Gerdy's tubercle. A Gerdy's tubercle is present on the proximal tibiae of other australopiths (KNM-KP 29285, A.L. 288-1, StW 514). The posterior part of the metaphysis has been sheared away, leaving only trabeculae exposed.

Medially, there is adhering matrix covering the *M. semimembranous* insertion.

#### U.W. 88-24: Partial Left Proximal Tibia

U.W. 88-24 is a small fragment of the left proximal tibia of MH2 preserving the anterolateral corner of the lateral condyle (Figure 12). This fragment measures 29.8mm AP, 14.5mm ML, and 18.2mm PD. There is a small, centrally located hole in the fibula facet and some minor damage extending posteriorly along the metaphysis. The medial aspect of the bone is sheared away, exposing internal trabeculae and rather thin (~1.1mm) subchondral bone.

Proximally, it preserves a small portion of the lateral condyle (28.6mm AP and 13.1mm ML), which is moderately convex AP, as is characteristic of other small-bodied australopiths (A.L. 288-1, A.L. 129-1), though it is not as convex as StW 514 (Berger and Tobias 1996). Laterally, there is a large and projecting fibula facet. The facet is 10.1mm AP (min) and 11.1mm PD and possesses a strong, projecting superior border. The superior part of the facet is flat mediolaterally, and gently concave proximodistally. The inferior part of the facet is more bulbous, convex proximodistally and slightly convex mediolaterally. The facet is oriented diagonally relative to the lateral condyle, which is similar to the orientation of a modern human superior fibular articular facet. Apes, on the other hand, tend to have a more inferiorly-facing facet (Aiello and Dean 1990). Anterolaterally there is a relatively flat and non-projecting Gerdy's tubercle for the insertion of the iliotibial band. The tubercle measures 11.1mm AP and 9.2mm PD, though these are minimum measurements since the bone is broken around the edges of the tubercle.

#### U.W. 88-97/98/99: Articulated Rearfoot And Distal Tibia

U.W. 88-97/98/99 are cemented together elements of the right rearfoot—a distal tibia, talus, and calcaneus (Figure 13). This is the earliest associated adult distal tibia, talus, and calcaneus in the hominin fossil record. They are de-

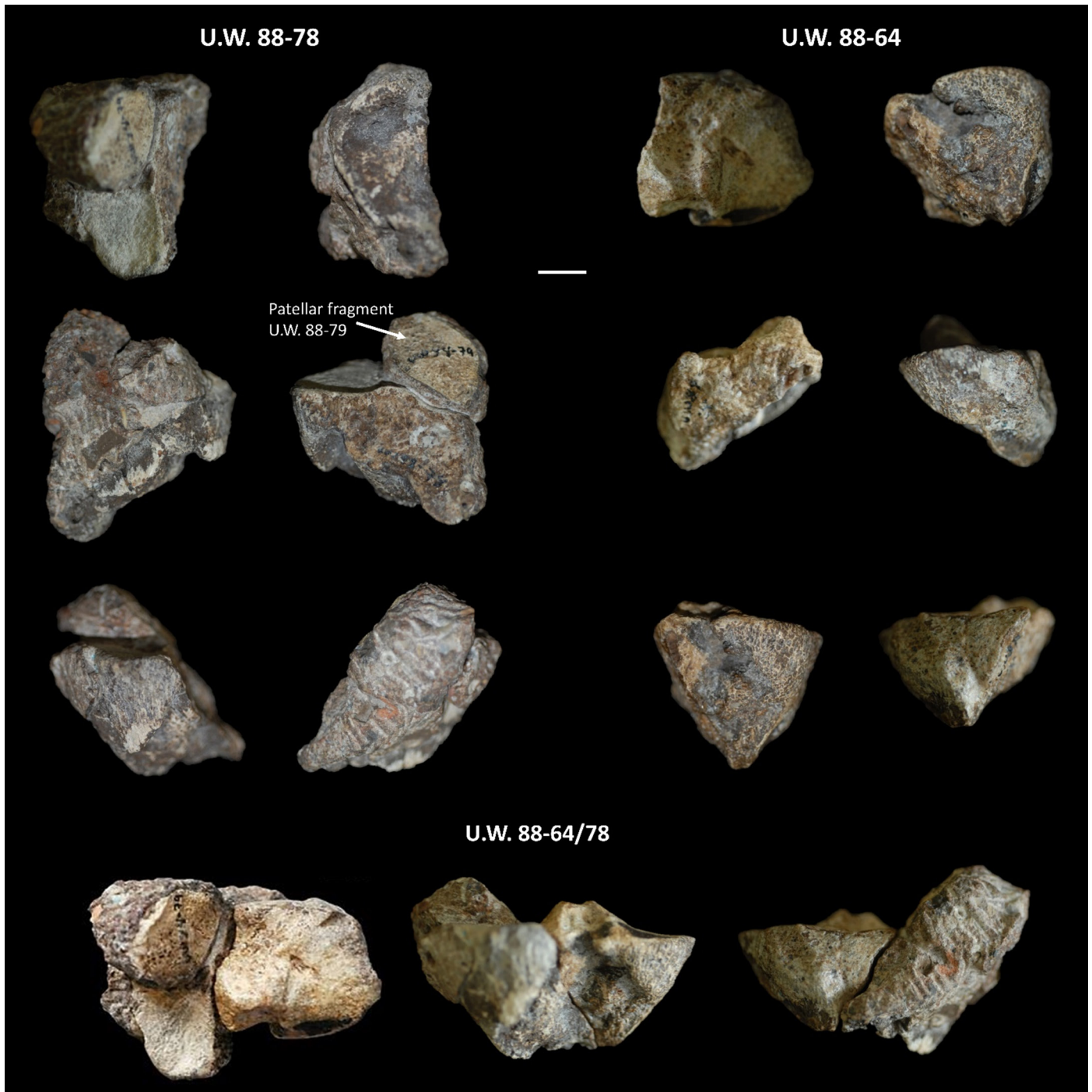


Figure 11. Right proximal tibia of MH2. Upper and middle left images are U.W. 88-78; upper and middle right images are U.W. 88-64. Each shown in (clockwise from upper left): superior, inferior, lateral, anterior, posterior, and medial views. Along the bottom U.W. 88-64 is conjoined with U.W. 88-78 shown in (left to right): superior, posterior, and anterior views. Note that attached to U.W. 88-78 is the U.W. 88-79 patellar fragment (scale bar=1cm).

scribed separately below based both on the original fossil and on 3D renderings of digitally segmented elements that were produced using a  $\mu$ CT scanner. Descriptions based solely on the 3D printouts of the segmented elements are differentiated in the text (see Materials and Methods for protocol), otherwise descriptions are based on observations collected from original specimens. The bones are very well-

preserved, although there is some surface erosion for each individual element. There is still some adhering matrix to the specimen along the lateral aspect of the tibia, the medial malleolus, and the anterior portion of the tibia. Additional bone can be observed in these adhering chunks, for example, bone cemented to the anterior part of the shaft has been digitally segmented from  $\mu$ CT scans and identified

TABLE 7. COMPARATIVE MEASUREMENTS ON THE HOMININ PROXIMAL TIBIA.

Specimen	AP depth of plateau	ML breadth of plateau	AP depth of medial condyle	ML width of medial condyle	AP depth of lateral condyle	ML width of lateral condyle	Source
U.W. 88-64/78	40.5	54.4	39.3	22.1 <sup>2</sup>	-	21.3 <sup>2</sup>	This study
KNM-KP 29285	44.1	69.2	42.6	26.1	38.4	24.4 <sup>1</sup>	This study
A.L. 129-1	33.2	50.7	29.2	20.1	22.6	21.2	Ward et al. (2012)
A.L. 288-1	32.8	50.2	31.1	22.6	27.6	21.6	Ward et al. (2012)
A.L. 330-6	42.6	65.7	37.4	26.7	33.1	29.2	Ward et al. (2012)
A.L. 333x-26	41.6	65.9	36.9	28.8	33.3	26	Ward et al. (2012)
A.L. 333-42	43 <sup>2</sup>	69 <sup>2</sup>	-	-	-	-	Lovejoy et al. (1982)
StW 514	31.7 <sup>1</sup>	52.3	-	20.5	20 <sup>2</sup>	20.8	Berger and Tobias (1996); This study
StW 396	-	-	37 <sup>2</sup>	24.4	-	-	Zipfel and Berger (2009)
KNM-ER 741	-	61.3	40.5	23.5	33.2 <sup>1</sup>	22.5 <sup>1</sup>	This study
KNM-ER 1471	-	-	30.9 <sup>1</sup>	24.2 <sup>1</sup>	30.7 <sup>1</sup>	20.5 <sup>1</sup>	This study
KNM-ER 1476	-	-	32.9	19.5	31.9	25	This study
KNM-ER 1481	35.9	66.5	34.3 <sup>1</sup>	23.9 <sup>1</sup>	34.8 <sup>1</sup>	21.9 <sup>1</sup>	This study
KNM-ER 1810	-	-	31.6 <sup>1</sup>	24 <sup>1</sup>	30 <sup>2</sup>	25.1 <sup>2</sup>	This study
Modern human (n=102)	-	70.2±5.3	44.6±3.4	31.1±2.2	39.2±3.5	30.6±2.8	This study

<sup>1</sup>Minimum measurements that underestimate the actual value.

<sup>2</sup>Estimates that approximate the actual value.

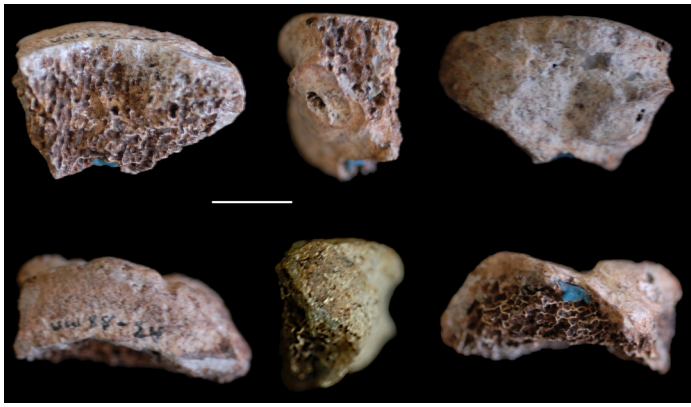


Figure 12. Fragmentary left proximal tibia (U.W. 88-24) in (top left to right): medial, posterior, and lateral views; same specimen in (bottom left to right): proximal, anterior, and distal views (scale bar=1cm).

as a metatarsal head. The tibia, talus, and calcaneus have shifted relative to one another diverging from anatomical position. The tibia is highly dorsiflexed on the talus and the calcaneus has inverted under the talus such that the posterior subtalar facet is no longer in contact with the posterior talar facet of the calcaneus.

U.W. 88-97 is a right distal tibia preserving 64.4mm of its length from a jagged break through the shaft to the tip of the medial malleolus (Table 8; Figure 14). A crack extends from the superomedial border of the proximal break across the anterior face of the shaft resulting in some anterior displacement of a small piece of the preserved shaft. The lateral aspect of the metaphysis is eroded, obscuring the fibular facet and exposing underlying trabeculae. Matrix adheres to the medial rim of the groove for the *M. tibialis posterior*

tendon, but the groove is not obscured and digital segmentation has removed this matrix. Fragments of bone are cemented to areas of the lateral, anterior, and medial shaft, obscuring some surface details, though these too have been digitally cleaned.

At the point of the proximal break, shaft dimensions are 21.1mm AP and 17.5mm ML. There may be some plastic deformation here rendering these measurements estimates. The digital 3D printout demonstrates that the shaft expands inferiorly into a metaphysis measuring 28.6mm ML and 25.4mm AP. The metaphysis is anteroposteriorly expanded relative to the talar facet, a feature typical of bipedal hominins (Zipfel et al. 2011). On a digital 3D printout, a squatting facet is present slightly lateral to the midline of the metaphysis. It measures 7.5mm ML and 3.4mm SI. The rim of the tibial plafond is relatively horizontal and does not possess an inferiorly projecting lip of bone at the anterior terminus of the keel. In anterior view, the medial malleolus projects inferomedially, rather than vertically downward. A coronal section of the 3D printout in anterior view reveals that the tibial plafond is nearly perpendicular to the shaft, producing an angle of  $91.7^\circ$ , like that found in modern humans and fossil hominins indicating a perpendicularly-oriented tibia over the foot (Figure 15A). In medial view of the 3D printout, the large, robust medial malleolus is dominant, measuring 15.4mm AP, 11.6mm ML, and 12.6mm SI. The robusticity index of the medial malleolus (Zipfel et al. 2011) is in the ape-range and well outside the modern human range. No other described fossil hominin tibia has a medial malleolus as relatively thick (DeSilva et al. 2013), except for the other *Au. sediba* distal tibia U.W. 88-21 (Figure 15C). This anatomy suggests that *Au. sediba* loaded its foot in an inverted position, perhaps during support phase of tree climbing and/or varus foot

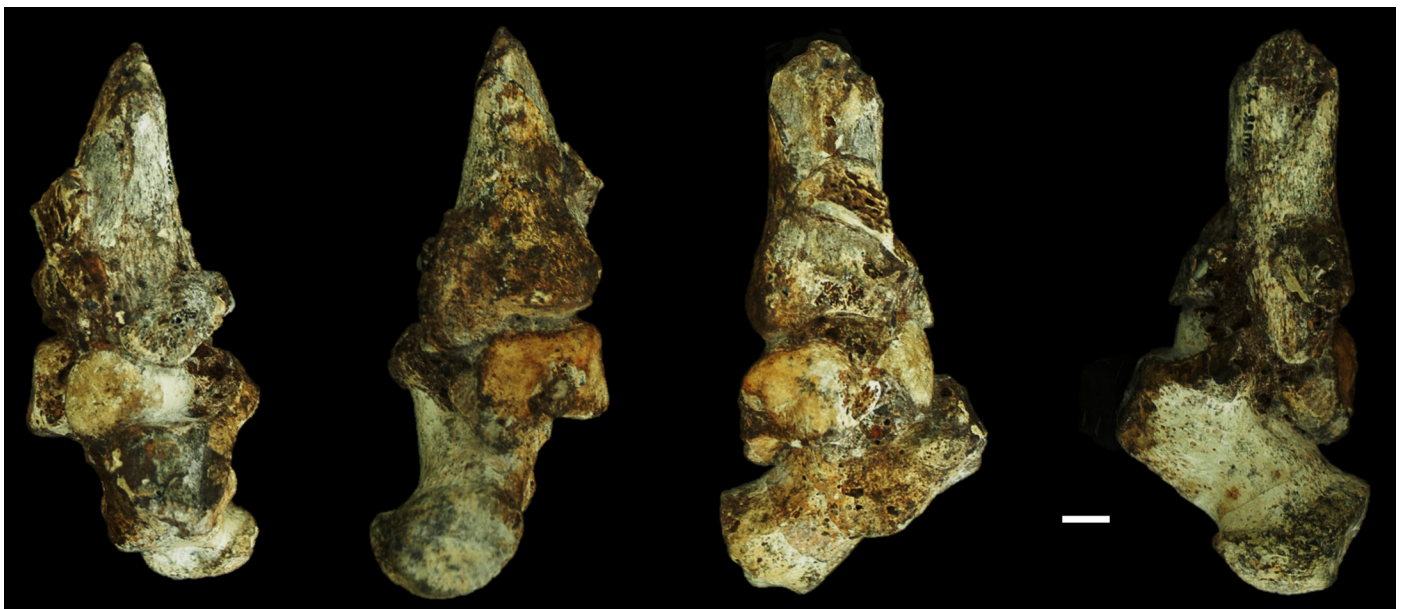
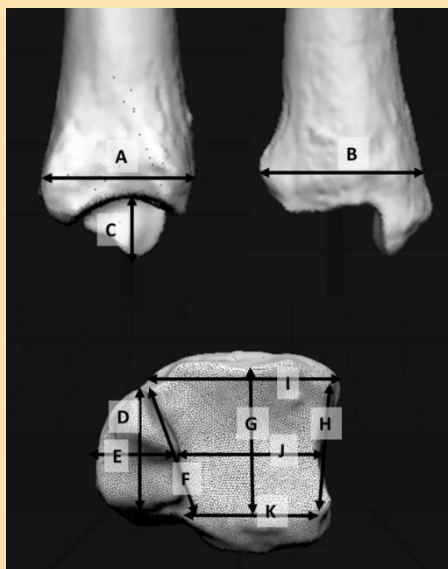


Figure 13. U.W. 88-97/98/99 oriented relative to the tibia and shown in (from left to right) anterior, posterior, lateral, and medial views (scale bar=1cm).

**TABLE 8. COMPARATIVE MEASUREMENTS OF THE DISTAL TIBIA IN FOSSIL HOMININS.**



	A	B	C	D	E	F	G	H	I	J	K
U.W. 88-21	26.2	27.9	12	17.2	12.2	18	19.3	18.3	21.5	17.2	19
U.W. 88-97	25.4	28.6	12.6	15.4	11.6	15.7	17.7	19	20.6	18.1	17.2
KNM-KP 29285	28.3	33.5	10.5	21.3	11.1	19	22.4	24.2	27	25.4	22.2
A.L. 288-1	21.6	24.5	9.1	14.5	8.1	14.6	17.2	19.6	20.8	17.3	18
A.L. 333-6	28	33.9	12	17.9	10.9	18	20.4	20.4	22.8	21.2	19.7
A.L. 333-7	33.4	35.6	13.7	21.4	13	20.4	23.9	24.5	28.3	25.4	23.2
A.L. 545-3 <sup>1</sup>	26.4	27.2	10	16.3	11	16.6	20.1	20	19.3	17.7	16.6
StW 181	-	-	-	-	-	-	-	-	-	21.1	20
StW 358	21.3	26.4	9.1	16.2	9	15.8	17.8	18.8	19.2	17.7	16.1
StW 389	28.9	30.7	-	-	-	18.8	20.7	22	23.4	21.9	20.6
StW 515	-	-	8.8 <sup>2</sup>	-	8.2	-	-	-	22.5	18.7	-
StW 567	33.7	33.5	15.2	21.4	11.1	20.3	21.2	24.9	25.5	23.5	17.7
OH 35	23.6	27	-	17.6 <sup>3</sup>	9.4 <sup>3</sup>	16.4	16.3	20.1	21.6	19.8	16.5
KNM-ER 1500	27.9	29.2	12.2	16.2	10.3	17.8	22.5	25	25.6	20.8	18.1
KNM-ER 2596	25.5	30.5	5.7	15.9	8.9	16.3	18.9	18.6	21.5	18	14.4
KNM-ER 1481	31.4	38.4	14.1	22.1	14.5	21.3	24	23.1	27.4	25.7	22.2
KNM-WT 15000	35.8	35.7	14.4	23.5	12.7	26.8	29.7	31.2	32	26.8	25.5
U.W. 101-420	30.3	-	-	-	-	17.2	19.5	20	-	19.4	-
U.W. 101-1416	25.4	-	11.4	14.1 <sup>2</sup>	7.1	-	-	15.4	18.7 <sup>3</sup>	17.1	15

<sup>1</sup>Measurements from Ward et al. 2012; supplemented by those (A-E; G) taken on cast.

<sup>2</sup>Minimum measurements that underestimate the actual value.

<sup>3</sup>Estimates that approximate the actual value.

positioning during the initial contact of support phase during bipedal walking gait (DeSilva et al. 2013). On the 3D printout, the lateral aspect of the medial malleolus is relatively flat AP and vertical, flaring anteromedially such that

it only slightly expands the anterior dimensions of the talar articular surface. Inferomedially, the tip of the medial malleolus is gently curved, possessing a relatively small intercollicular region for the origin of the tibiotalar portion of



Figure 14.  $\mu$ CT renderings of the distal tibia (U.W. 88-97). Top (from left to right): anterior, inferior, and posterior views. Bottom (left to right): medial and lateral views (scale as in image).

the deltoid ligament.

Posteriorly, there is a well-developed groove running inferomedially for the tendon of *M. tibialis posterior*. Measurements on the digitally segmented 3D printout yield a wide groove that is approximately 6.2mm ML and 0.9mm deep, measured at its deepest point. The tubercle of the posterior tibiofibular ligament strongly projects posterolaterally. On the 3D printout, the interosseous crest is very weakly developed anteriorly, terminating in a projection of bone for the anterior tibiofibular ligament positioned anterior and slightly superior to the distal fibular facet. In lateral view, the posterior rim of the tibial plafond projects more inferiorly than the anterior rim, producing a dorsiflexed set of  $6.7^\circ$  to the ankle joint (Zipfel et al. 2011; Figure 16). In lateral view, it is clear that the tibial plafond is deeply curved and unlike the flat joint surface found often in extant apes. The depth ratio relative to the width of the articular surface is 17.8% (see Figure 15B), which suggests reduced joint excursion in *Au. sediba* compared with modern apes.

The talar articular surface of the 3D printout measures 18.1mm ML and 17.7mm AP at the midpoint of the articu-

lar surface for the talus. The articular facet is slightly anteriorly-wedged, with an anterior breadth (20.6mm ML) exceeding a posterior breadth (17.2mm); it does not have the strongly trapezoid-shaped talar surface commonly found in African ape distal tibiae (DeSilva 2009; Zipfel et al. 2011; see Figure 15D). Like humans and other fossil hominins, the articular surface is broader laterally (19mm AP) and narrower medially (15.7mm AP). The articular surface is relatively flat mediolaterally, divided at the midline by a gentle AP keel.

#### TIBIA OF MH4

##### U.W. 88-21

U.W. 88-21 is a right distal tibia (Figure 17; see Table 8). It fits cleanly with U.W. 88-40, which was recovered from a block of calcified clastic sediment that preserves the anterior impression of the proximal tibia. The entire tibia has been estimated between 267–275.5mm (DeSilva et al. 2013; Holliday et al. 2018). U.W. 88-21 is very well-preserved, measuring 152.2mm from a transverse break through the

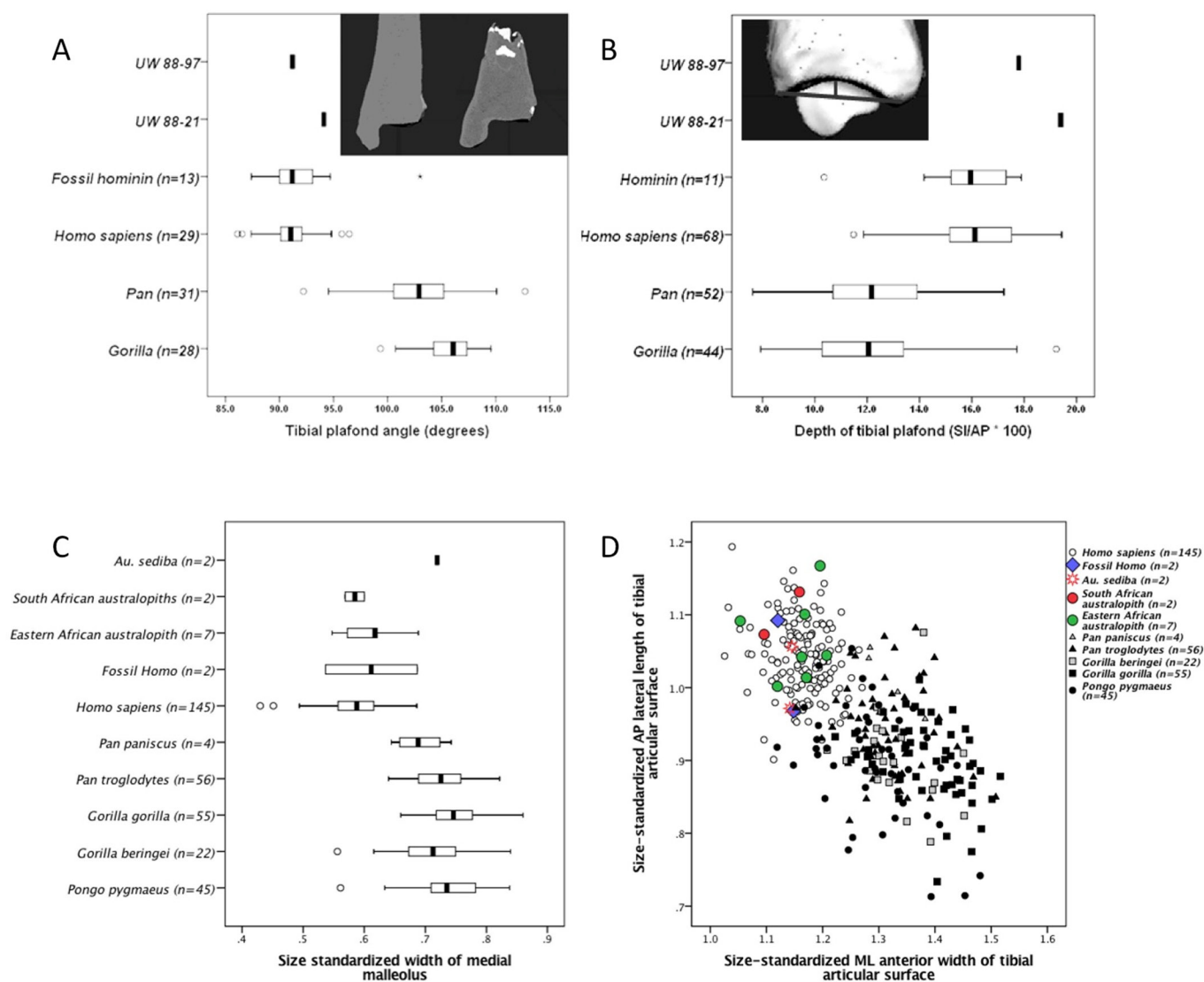


Figure 15. A) As in modern humans and other fossil hominins, *Au. sediba* had a vertical tibial shaft relative to the plane of the ankle joint (tibial plafond), an important bipedal adaptation that positions the foot directly under the knee. B) Modern humans have a deep tibial plafond compared to the relatively AP flattened talar facet found in African apes. Hominin fossils, including the two distal tibiae from *Au. sediba* align with modern humans in this anatomy. C) The *Au. sediba* tibiae ( $n=2$ ) possess ape-like, ML thick medial malleoli. In Zipfel et al. (2011), we standardized ML thickness of the medial malleolus by its AP width and by the surface area of the talar articular surface. Here, we calculated a geometric mean (GM) as the 11th root of the product of 3 dimensions of the malleolus, 2 dimensions of the metaphysis and 6 dimensions of the talar articular surface and divided the ML width of the medial malleolus by this GM. The two *Au. sediba* tibiae are nearly identical in medial malleolar thickness, in the ape-range. (D): The 6th root of the product of the 6 dimensions of the talar articular surface were used to standardize the anterior ML width and lateral AP length of the talar articular surface. Apes tend to have laterally short and anteriorly broad tibiae. Humans and all hominins, including *Au. sediba* have similarly shaped talar articular surfaces that tend to differ from the ape configuration.

proximal shaft to the most distal aspect of the medial malleolus. There is very little damage or erosion of the surface of the preserved shaft and the distal end save for some minor exfoliation of the cortical bone and some adherence of matrix along the posterior shaft.

The shaft is straight, and does not possess the anterior and lateral bowing exhibited by tibiae of apes. At the proximal break, the shaft is teardrop-shaped in cross section, measuring 23.6mm AP and 18.9mm ML. Cortical bone

of the cross section is thick, measuring 10.5mm anteriorly, 6.6mm posteriorly, 7.1mm medially, and 4.7mm laterally. The shaft flares moderately at the metaphysis, with maximum dimensions of 27.9mm ML and 26.2mm AP at this point. The anterior surface of the shaft is strongly convex and exhibits a prominent ridge running proximolaterally. The lateral surface is convex distally, but flattens proximally. Medially, the shaft remains relatively flat throughout its length, with a convex ridge progressively forming proxi-

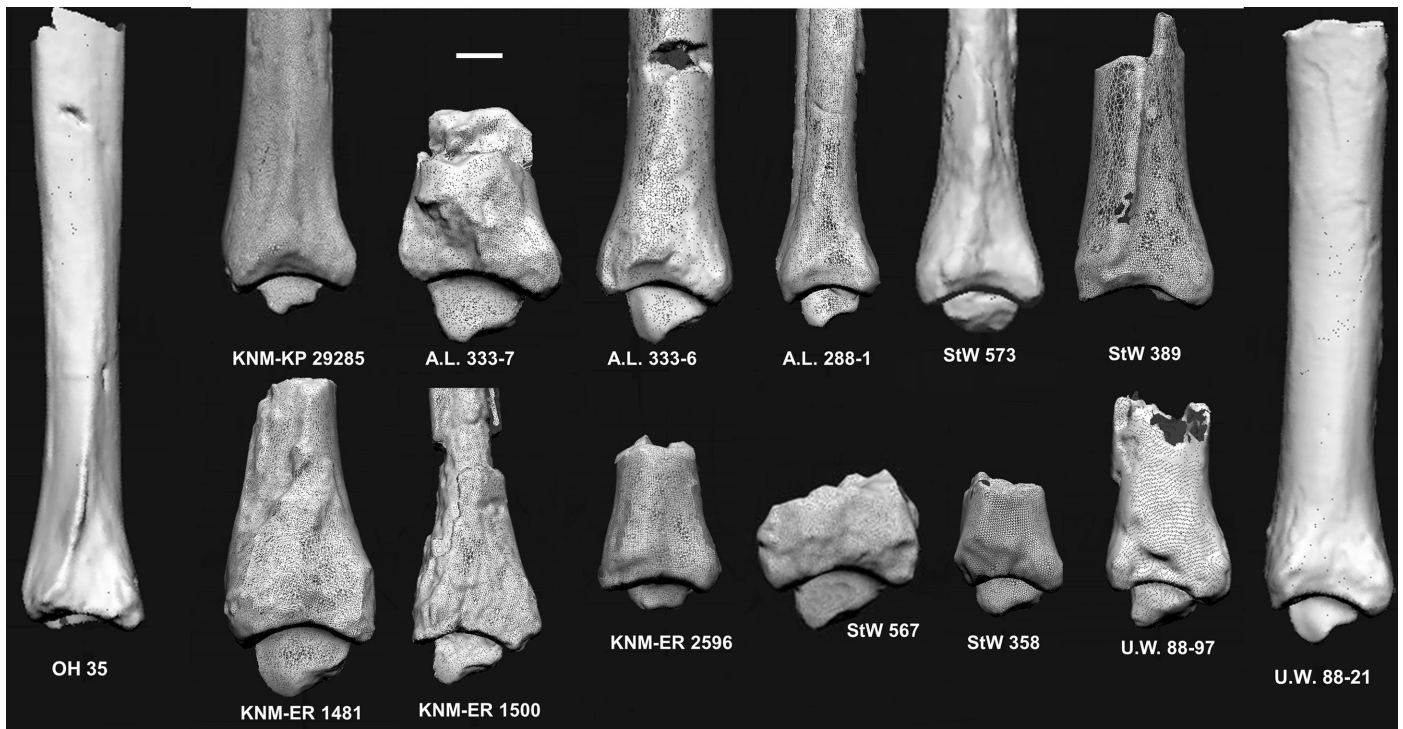


Figure 16. Hominin tibiae in lateral view, and mirrored when necessary, to all reflect the left side. U.W. 88-97 and another Au. sediba tibia (U.W. 88-21) are shown at the far right and have both been mirrored. This figure illustrates size and anatomical variation among australopithecine and early Homo distal tibiae from East and South Africa (scale bar=1cm).

mally on the medioposteriorly aspect of the shaft. Adjacent to the posterior side of this ridge is a depression for the origin of *M. flexor digitorum longus*. The posterior surface of the shaft is flat distally and progressively becomes more convex proximally. Relative to the dimensions of the shaft and to the articular surface, the metaphysis is AP expanded (Zipfel et al. 2011). There is no external or internal evidence of an epiphyseal line along the diaphyseal-epiphyseal junction, and thus this bone is attributed to an adult, MH4 (DeSilva et al. 2013; Holliday et al. 2018; Zipfel et al. 2011) rather than MH1 as originally hypothesized (Berger et al. 2010), and often illustrated.

Anteriorly, there is a squatting facet, measuring 15.1mm ML and 3.4mm SI extending over the lip and gently projecting inferiorly at the anterior margin of the talar facet. The anterior surface of the metaphysis has a weak groove running mediolaterally and inferiorly onto the medial malleolus—several nutrient foramina can be found along this groove. The medial malleolus is angled inferomedially rather than vertically with the articular surface on its lateral side being vertical and extending anteriorly, producing a very weak bulbous morphology. The malleolus is stout, measuring 17.2mm AP, 12.2mm ML, and 12mm SI (see Figure 15C). In medial view, there is a well-developed intercollicular groove for insertion of the tibiotalar portion of the deltoid ligament, a ligament which stabilizes the joint during dorsiflexion. A coronal section of the fossil in anterior view reveals that the tibial plafond is nearly perpendicular to the long axis of the shaft, forming an angle of 94.1°

like that found in modern humans and fossil hominins, indicating a perpendicularly-oriented tibia over the foot, and indirectly indicating a valgus knee (see Figure 15A).

The articular surface for the talus is only moderately anteriorly-wedged, measuring 21.5mm ML anteriorly and 19mm ML posteriorly (see Figure 15D). It is similarly broad laterally (18.3mm AP) and medially (18mm AP). Mid-point dimensions of the tibial plafond are 17.2mm ML and 19.3mm AP. There is a very weak midline AP keel, suggesting a relatively flat tibiotalar joint. Posteriorly, the groove for the tendon of *M. tibialis posterior* is wide and deep, measuring 8.5mm ML and 2.2mm AP deep at its deepest point. The medial rim of the groove consists of a pronounced ridge of bone. The lateral rim is subtler and terminates distally in a small tubercle. On the lateral side of the posterior surface of the tibia is a large tuberosity for the posterior tibiofibular ligament. Laterally, there is an articular facet for the fibula measuring 16mm ML and 4.4mm SI. The facet is surrounded anteriorly and posteriorly by pronounced tubercles for the posterior and anterior tibiofibular ligaments. The anterior tubercle is positioned superiorly to the distal fibular facet. There are palpable but very weak anterior and posterior crests that merge 19.7mm SI from the tibial plafond into a ridge of bone that continues superiorly. This ridge bulges from the shaft; an X-ray reveals thickened cortex in this region of the bone. In lateral view (see Figure 16), the posterior rim of the tibial plafond projects more inferiorly than the anterior rim, producing a dorsiflexed set of 4.9° to the ankle joint. In lateral view, it is clear that



Figure 17. Illustrated in the bottom left is U.W. 88-21 in (left to right): anterior, posterior, medial, and lateral views. Illustrated in the top left (left to right) is the cross section of the break through the proximal shaft, and the distal articular surface. To the near right is U.W. 88-21 conjoined with U.W. 88-40, and to the far right is U.W. 88-40 in its block of sediment along with the impression of the proximal tibia (scale bar=1cm).

the tibial plafond is deeply curved and unlike the flat joint surface found often in the apes (see Figure 15B). The depth ratio relative to the width of the articular surface is 19.4%, which suggests reduced joint excursion in *Au. sediba* compared with modern apes.

#### U.W. 88-40

U.W. 88-40 conjoins with U.W. 88-21 anteriorly and medially (Figure 18). Anteriorly, the bone measures 91.1mm PD. Its distal break is oblique and angled anterodistally to posteroproximally, reducing the length of the posterior side 21.6mm relative to its anterior side. Likewise, proximally, the break is oblique through the shaft. The preserved posterior length is 54.9mm. Laterally, a large piece of the distal part of the bone is missing, reducing the length of the lateral shaft to only about 27mm. A longitudinal crack spans the entire preserved length of the lateral surface of the shaft.

Along the preserved lateral margin is the interosseous crest, which demarcates the origins of *Mm. tibialis posterior* and *tibialis anterior*. The anterior and posterior parts of the shaft are strongly convex. The lateral surface of the shaft is flat. Medially the shaft is convex, but there is a strong ridge of bone running proximoanteriorly to distoposteriorly, posterior to which is a large depression for the *M. pop-*

*liteus* insertion. The posterior break is positioned along the path of where a *M. soleus* line would be, if present. There is only one small piece of the bone that preserves the anterior, posterior, medial, and lateral aspects. It has breadth dimensions of 26.8mm AP and 18.9mm ML. An analogous region on OH 35 is more ML compressed (16mm ML) but has a similar AP dimension (26mm). Similar ML compression is present on the Koobi Fora specimen KNM-ER 1476—23.3mm AP versus 14.5mm ML.

#### FIBULA OF MH1

##### U.W. 88-18

U.W. 88-18 is a small fragment of left fibula, probably from the left side of MH1 preserving an area just distal to the midshaft based on muscle scar identifications (Figure 19).

It is only 15mm long, 6.8mm AP and 8.6mm ML. Attachment sites of *Mm. extensor digitorum longus* and *extensor hallucis longus* can be barely detected, while the origin for *M. peroneus brevis* is flat, as is the case in humans (Susman and Stern 1982). An analogous region is preserved on the StW 356 fibula from Sterkfontein Member 4, and appears to be more robust.



Figure 18. U.W. 88-40 conjoined with U.W. 88-21 to far left. In the middle and on the right, the isolated U.W. 88-40 is isolated in anterior, medial, posterior, and lateral views (scale bar=1cm).

## FIBULA OF MH2

### U.W. 88-23/84/146/202

These four pieces conjoin cleanly to form the most proximal 97.1mm of the left fibula of MH2 (Figure 20). The maximum length of the four pieces are as follows—U.W. 88-23: 41.1mm; U.W. 88-84: 13.4mm; U.W. 88-146: 23mm; and U.W. 88-202: 27.1mm. The medial aspect of the styloid process is sheared off.

The minimum AP width of the styloid process can be estimated as 19.5mm. Medially along the shaft there is a strong interosseous crest. Adjacent to the anterior border of the crest is an insertion for the *M. extensor digitorum longus*. Posterior to the crest, the shaft remains relatively flat throughout its length. There is a large region for the origin of the *M. soleus* on the posterior surface. Laterally, the shaft is convex. At the distal break through the shaft, the cross-section measures 9.5mm ML and 11.3mm AP. The fibular

neck is relatively narrower (8mm AP and 8.4mm ML). Perhaps most notably there is an osteophytic growth where the *M. biceps femoris* inserts at the neck shaft junction. There are few proximal fibulae in the hominin fossil record for comparison. Overlapping external dimensions in StW 356 reveal a more robust fibula in *Au. africanus* than in *Au. sediba* (DeSilva et al. 2013).

## TALUS

### U.W. 88-98

U.W. 88-98 is a right talus (Figure 21; Table 9), associated with a distal tibia U.W. 88-97, and calcaneus U.W. 88-99. The talus is described separately below based both on the original fossil and on 3D renderings of digitally segmented elements that were produced from high resolution image data (see Materials and Methods for protocol), otherwise the descriptions are based on the original specimen. The



Figure 19. Left fibular shaft (U.W. 88-18) in medial, anterior, posterior, superior, and inferior views (scale bar=1cm).



Figure 20. Far left: Conjoined pieces of MH2 left fibula (U.W. 88-23, -84, -146, -202) in lateral view. Upper right: U.W. 88-23 and -84 in (from left to right): medial, anterior, lateral, and posterior views. Notice the osteophytic growth at the insertion of *M. biceps femoris* on U.W. 88-23. Bottom middle: cross-sectional images of U.W. 88-23 and -88. Bottom right: medial view of broken fibular styloid U.W. 88-23 (scale bar=1cm).

talus is overall small measuring a maximum of 39.8mm PD and from the 3D printout, 32.9mm ML. The body is 21.5mm deep dorsoplantarily. There is some erosion along the fibular facet, mostly proximally and plantarly, but also along the junction of the neck and body, that has removed the tip of the fibular facet and the most distal part of the anterior calcaneal facet.

In dorsal view, the 3D printout of the talar trochlea is only moderately anteriorly-wedged (Figure 22). Proximally, the trochlea is 16.5mm ML, 18.1mm ML at the midpoint of the joint surface, and expands to 20.3mm ML distally. The trochlear surface is only moderately AP grooved, corresponding to the gentle AP keel along the midline of the tibial plafond on U.W. 88-97. The talar axis angle (formed between the superior surface of the talus and the axis of rotation of the ankle joint, as determined by the most inferior aspect of the malleolar facets) is 7° (see Figure 22). The

talar neck is quite short, and there is a small pit between the trochlear body and the talar head for articulation with the beak at the anterior intersection of the keel and the talar facet margin of the distal tibia during dorsiflexion. A ridge of bone continues distomedially from the trochlear body toward the talar head. The head and neck form a horizontal angle of 28° relative to the body of the talus (Zipfel et al. 2011), which is similar to that exhibited by other tali attributed to australopiths.

The talar head is relatively large, measuring 23.5mm ML and 19.5mm DP. On the 3D printout, the angle of head torsion is between 15° (Zipfel et al. 2011) and 20° (remeasured for this study). Either measure is within the range found in African ape tali, and quite distinct from the higher head torsion angles of 43.2°±5.1° found in humans (n=40) (Zipfel et al. 2011). Furthermore, this value is the lowest for any hominin talus measured (Zipfel et al. 2011). Kidd

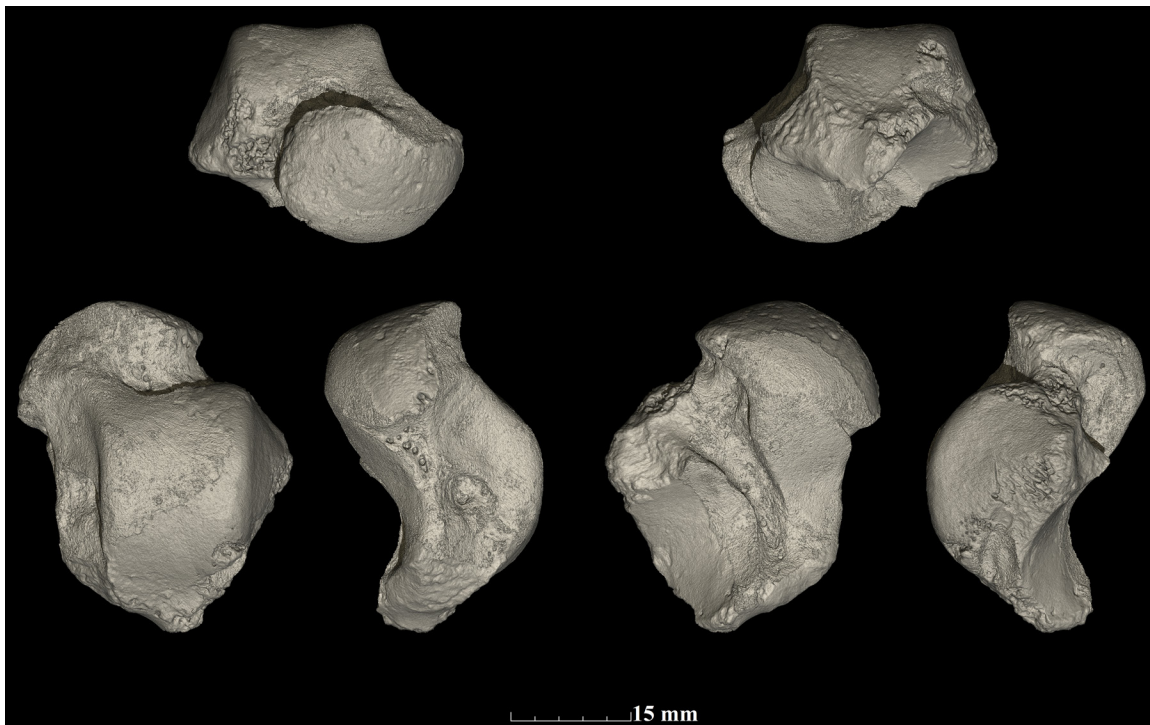


Figure 21.  $\mu$ CT renderings of the talus (U.W. 88-98). Top (from left to right): distal and proximal views. Bottom (left to right): dorsal, medial, plantar, and lateral views (scale as in image).

(1993) has suggested that talar head torsion is related to mobility at the midtarsal joints. The rather low head torsion angle is consistent with other forms of evidence (see U.W. 88-22 fourth metatarsal) that *Au. sediba* had more midfoot mobility than other australopiths.

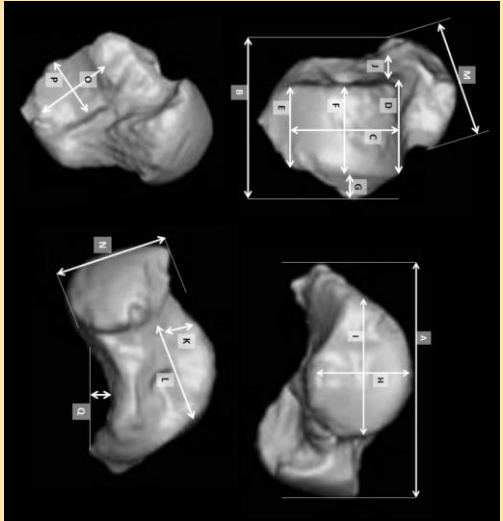
Medially, the cotylar fossa of the 3D printout gently slopes medially and plantarly, and is not deeply excavated as in many non-human primates. The medial articular surface is dominated by a large pit for the tibiotalar portion of the deltoid ligament. In lateral view, the talar trochlea is strongly curved, forming a radius of curvature of 11.6mm. The fibular facet is 23.2mm PD and 17.9mm from its dorsal surface to the plantar rim of the fibular facet. The fibular facet gradually slopes plantolaterally, as other australopith tali do, and lacks the distinctively vertical face and abrupt curve that forms the base of the fibular facet characteristic of tali from *Homo* (see Figure S7 in Zipfel et al. 2011). There is some damage at the junction of the neck and body, though it appears as though there may still be evidence of an area of insertion for the anterior talofibular ligament. Because of erosion to the original fossil, anterior and posterior extents of the articular surface are not clearly visible in lateral view. We can approximate these boundaries of the articular surface, however, using the associated tibia (U.W. 88-97; see below). The angle subtended by the most anterior and posterior aspects of the articular facet is 145° (Figure 23), which is higher than that calculated for A.L. 288-1 (139°) (Latimer et al. 1987) and falls within the range of modern chimpanzees. However, these high subtended angles may be a function of the small size of both Lucy and MH2, given the lower values in humans, gorillas, and the

larger A.L. 333-147 (Latimer et al. 1987; Ward et al. 2012). In lateral view, the talar head declines plantarly relative to a line connecting the most anterior and most posterior articular points for the tibia (following Day and Wood 1968). This angle of declination taken on the 3D printout is 28°, which is considerably higher than those exhibited by ape tali (13.9°–17.7° in Day and Wood 1968), and just lower than the human range (31.3°–37.5° in Day and Wood 1968). Functionally, Day and Wood (1968) relate this angulation of the talus to a longitudinally arched foot, which if true would indicate that *Au. sediba* had an arch, though flatter than most humans (see Prang 2015). Proximally, the groove for *M. flexor hallucis longus* descends plantomedially and is ~4.5mm ML wide. The lateral tubercle of the posterior process is present, but the medial tubercle is damaged, preventing a more detailed characterization of this region.

Plantarly on the 3D printout, there are two facets for the calcaneus separated by the sulcus tali, which is 4.6mm wide at its midpoint. The posterior of the facets is flat mediolaterally and quite concave proximodistally. Though erosion along the distal extent of the facet prevents precise measurement, it is a minimum of 20.1mm PD and 13.7mm ML. The middle facet for the sustentaculum tali is roughly 20.6mm PD and grades into the talar head. The middle facet is narrow proximally (8.2mm ML) and widens distally to a maximum of 13mm ML prior to the start of the talar head.

The U.W. 88-97 and U.W. 88-98 ankle joint represents one of only three definitive ankles in the early hominin fossil record, the other two being A.L. 288-1 and StW 573. OH 8/35 is controversial, with some suggesting these derived from the same individual (Susman and Stern 1982), and

TABLE 9. COMPARATIVE MEASUREMENTS OF THE TALUS IN FOSSIL HOMININS.



Fossil talus	A	B	C	D	E	F	G	H	I	J	K	L	M	N	O	P	Q
U.W. 88-98	39.8	32.9	24.9	20.3	16.5	18.1	-	17.9	23.2	4	11.4	21.4	23.5	19.5	22.5 <sup>1</sup>	13.7	-
A.L. 288-1	35.7	33.1	19.1	20.2	16.1	18	6.2	15.5	21.2	4.8	10.4	19.5	20.7	14.5	32	24.5	4.3
A.L. 333-75	-	-	-	-	-	-	-	-	-	-	-	-	25	16.1	-	-	-
A.L. 333-147	48.3	39.4	30.1	26.2	20.7	24.1	7.7	21.2	30.2	4.1	13.7	25.4	-	-	27.7	17.6	6.3
StW 88	43.2	35.8	24.5	21.9	18.2	19.1	7.2	19.5	24.3	5	11.5	23.5	24.7	17.9	25.9	16.8	6.3
StW 102	-	-	-	-	18.4	19.4	6.7	18.9	-	-	-	-	-	-	25.7	17.8	6.7
StW 347	-	-	-	21.3	-	-	-	-	-	2.9	9.8	-	21.1	17.1	-	-	-
StW 363	37.5	34.4	23.6	22.4	16.9	19	-	15.8	21.4	4.7	10.7	21	-	-	21.5	11.8	-
StW 486	-	35.7	-	23	-	21	8.4	19.9	21.2	2.4	9.8	-	24.6	-	21.9 <sup>1</sup>	12.2	-
StW 573	41.2	33.3	26	23.8	20.5	-	-	-	25.2 <sup>2</sup>	2.9	10.1	26.8	24.4	17.1	20.1	14.2	4.2 <sup>1</sup>
TM 1517	-	-	-	22.6	16.5	18.9	6.1	16.1	-	2.4	12	22.1	27.7	-	-	-	-
SKX 42695	-	-	-	-	19.7	23.1	8.7	18.6	24	-	-	-	-	-	25.1	16	4.5
Omo 323-76-898	55.1	44.7	28.8	26.4	22	23.2	10.7	25.8	27.1	1.6	14.1	28.9	27.5	18.1	29.3	17.4	7
OH 8	36.7	37.1	21	22.5	18.3 <sup>2</sup>	19.5	6.5	17.1	23.4	5.9	12.6	26.7	24.4	17.5	-	12.7 <sup>2</sup>	-
KNM-ER 813	50.6	37.2 <sup>1</sup>	27.7	27.6	23.3	24.7	6.7 <sup>1</sup>	22	28.1 <sup>2</sup>	3.4 <sup>1</sup>	10	24.8	27.8 <sup>2</sup>	17.8 <sup>1</sup>	27.7	20.5	4.7
KNM-ER 1464	48.7	43.4	27	27.1	23.4	25.3	8.7	24.2	27.3	3.7	13.7	24.7	28.4	20.1	30.7	18.4	6.2
KNM-ER 1476	44.2	38.6	24.3	23.6	19.5	20.4	8.7	19.4	25.2	5.3	11.2	25.8	25.9	-	27.3	15.4	6.2
KNM-ER 5428	57.3	50.5	31.1	36.6	30.9	33.9	9.5	22.6	34.8	3.6	11.9	31	36.6	24	21.1	10.3	4.7
U.W. 101-148	43.4	39	26.4	22.4	19.5	20.6	8.6	20.5	20.2	3.6	8	23	23.9 <sup>2</sup>	18.4	27.6	17.8	5.7
U.W. 101-520	40.8	35.6	26.2	19.7	-	18.3 <sup>2</sup>	7.8	20.3	18.8	2.9	-	-	21.3 <sup>2</sup>	13.4 <sup>1</sup>	25.4	14.8	4.9
U.W. 101-1417	38.4	34.5	19	19.6	17.1	18.4	6.6 <sup>1</sup>	18.5	14.2	5.6	8.6	19.9	20.7 <sup>2</sup>	14.3	22.5	14.8	4.1 <sup>1</sup>

<sup>1</sup>Minimum measurements that underestimate the actual value.

<sup>2</sup>Estimates that approximate the actual value.

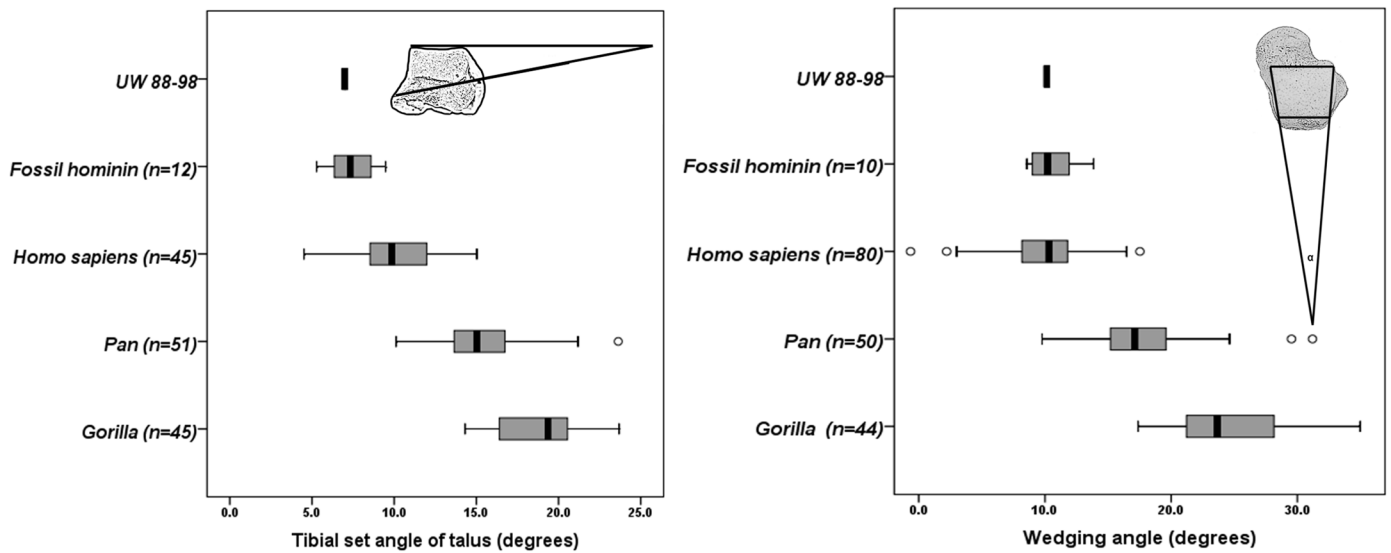


Figure 22. Left graph: The angle formed between the plane of the ankle joint and the axis of rotation (through the tips of the malleoli) differs between bipedal hominins and apes (DeSilva 2009; Latimer et al. 1987). This talar axis angle in U.W. 88-98 is within the observed human distribution, indicating a human-like set of the tibia on the talus. Right graph: The talar body is wedged such that the anterior aspect of the facet is wider than its posterior aspect. This form of wedging is more extreme in the apes, which has been postulated to help dissipate loads incurred during climbing on a highly flexed ankle (DeSilva 2009). The wedging of U.W. 99-98, as with all other fossil hominins, is human-like.

others suggesting they are not only from different individuals, but perhaps from different species (Wood et al. 1998). There is also the possibility that StW 358/363 are associated as well, representing one ankle (Fisk and Macho 1992).

### CALCANEUS OF MH1

#### U.W. 88-113

U.W. 88-113 is a right calcaneal apophysis (Figure 24). It is

complete and well-preserved, other than a 14.1mm crack running superomedially to inferolaterally that spans the plantar part of the bone.

U.W. 88-113 was originally described as a left (Zipfel et al. 2011), but direct comparisons with human and chimpanzee calcaneal apophyses reveal it to most likely be a right calcaneus. Scheuer and Black (2008) suggest siding a calcaneal apophysis by positioning the more “scale-like” surface superiorly. Following this criterion, the apophysis again appears to be from the right side. Scheuer and Black (2004) further suggest that this “cap-like covering” is unlikely to be identifiable as a calcaneal apophysis before 10 years of age in modern humans. Baker et al. (2005) observed that fusion to the calcaneal body in humans begins between 10–14 years, and is complete between ages 16–22. Passalacqua (2013) more recently refined the age at which the apophysis begins to fuse to the calcaneal body in humans to  $12.8 \pm 1.53$  years. The developmental age of this specimen, therefore, resides in a very specific window (~10–12 years) that fits the age of the MH1 individual (based on modern human developmental standards) quite well (Berger et al. 2010).

The apophysis is 30.2mm DP and a maximum of 21.9mm ML. An apophyseal flange projects laterally, and is 12.6mm superior to the most plantar aspect of the bone. The elevated positioning of this flange, which forms the homologous structure as the lateral plantar process (or lateral tubercle) in humans (Boyle et al. 2018; Latimer and Lovejoy 1989), is similar to that observed in the MH2 calcaneus and contrasts starkly with the anatomy of a modern human calcaneal apophysis (Latimer and Lovejoy 1989; Zipfel et al. 2011; Figure 25). Dorsal to the flange, the apophysis

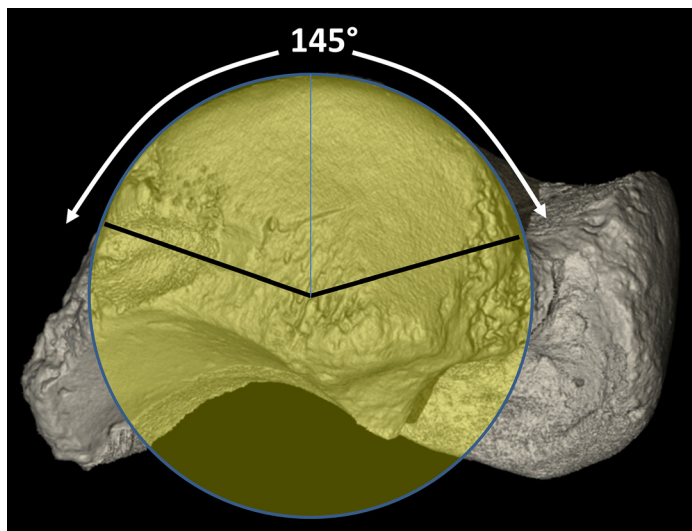


Figure 23. The angle subtended by the articular facet of the talus is 145°, which is slightly higher than the value calculated for A.L. 288-1 (Lucy), and may be related to the small size of MH2.



Figure 24. U.W. 88-113 in (from left to right): lateral, distal, medial, and proximal views. Note the dorsally elevated apophyseal flange that forms the lateral plantar process in adult calcanei (Scale bar=3 cm; photo by P. Schmid).

is bulbous and scale-like. It is delineated from the plantar half of the apophysis by a subtle line running superolateral to inferomedially. The plantar region is smooth proximally, with a distinct medial plantar process that extends distally and terminates in a narrow beak-like projection. As mentioned above, U.W. 88-113 recalls the anatomy of the MH2 calcaneus (Figure 26), though it is slightly smaller in dorsoplantar height, which may be related to its juvenile status. There are two important points to be made from the anatomy of U.W. 88-113. First, Latimer and Lovejoy (1989) observed that infant human calcanei possess a plantarly positioned lateral plantar process, leading them to suggest that this repositioning of a structure that would functionally increase the volume of the calcaneal tuberosity and help dissipate forces during heel-striking bipedalism was probably under genetic control. Our observations on juvenile calcanei of humans and great apes concur (Zipfel et al. 2011). Second, another individual (MH1) with a dorsally positioned lateral plantar process lessens the possibility that MH2 may be pathological in calcaneal anatomy, but suggests instead that a primitive, more ape-like development of the plantar tubercles may characterize *Au. sediba*.

## CALCANEUS OF MH2

### U.W. 88-99

U.W. 88-99 (Figures 27 and 28; Table 10) is the most complete adult calcaneus in the early hominin fossil record (Figure 29). It is associated with and still physically adherent to U.W. 88-97 and U.W. 88-98. Descriptive text based solely on the 3D printouts of the segmented element is noted (see Materials and Methods for protocol), otherwise the descriptions are based on the original specimen. The fossil measures 56.9mm from the most proximal aspect of the calcaneal tuberosity to the cuboid facet, which has some erosion at the plantar border and thus this is a minimum length measure though quite close to the actual length. There is etching along the lateral surface of the calcaneal

body, producing several small holes in the cortex; however, the surface is generally well-preserved. Distally, the cuboid facet is heavily eroded around the edges, and thus it is difficult to accurately characterize its morphology.

On the 3D printout, the lever arm for *M. triceps surae* is long, measuring 40.1mm from the calcaneal tuberosity to the midpoint of the posterior articular surface of the talus, and only 16.8mm from this point to the cuboid facet. The most salient aspects of this bone can be seen in lateral view.

The superior half of the calcaneal tuberosity is flat and angled superodistally to inferoproximally. The tuberosity flexes at its SI midpoint below which it curves plantarly to become convex and beak-shaped. In lateral view, the cuboid facet is slightly angled plantarly, similar to the condition exhibited by modern humans and suggestive of rearfoot arching (Berillon 2003). However, erosion around the cuboid facet (especially plantarly) stipulates that any assessment of the plantarly angled facet is tentative. The DP height of the most distal aspect of the calcaneal body is 20.1mm.

In lateral view, the lateral plantar process is well-developed and dorsally positioned. There is a nearly horizontal retrotrochlear eminence connecting the lateral plantar process and the peroneal trochlea, which is quite robust. This aspect of the anatomy of the *Au. sediba* calcaneus contrasts with anatomies found in modern humans and in *Au. afarensis* (Latimer and Lovejoy 1989; Zipfel et al. 2011). While it has been argued that the lateral plantar process and the peroneal trochlea are developmentally (and inversely) related in hominoids (e.g., Weidenreich 1940), recent evidence to the contrary suggests there may be no inverse relationship between these structures (Gill et al. 2014), demonstrating both the independence of these anatomies, and the selective importance of the plantar shift of the lateral plantar process in the evolution of efficient bipedal gait (Latimer and Lovejoy 1989). Lateral plantar process positional information appears not to change developmentally (Latimer and Lovejoy 1989; Zipfel et al. 2011) and therefore may

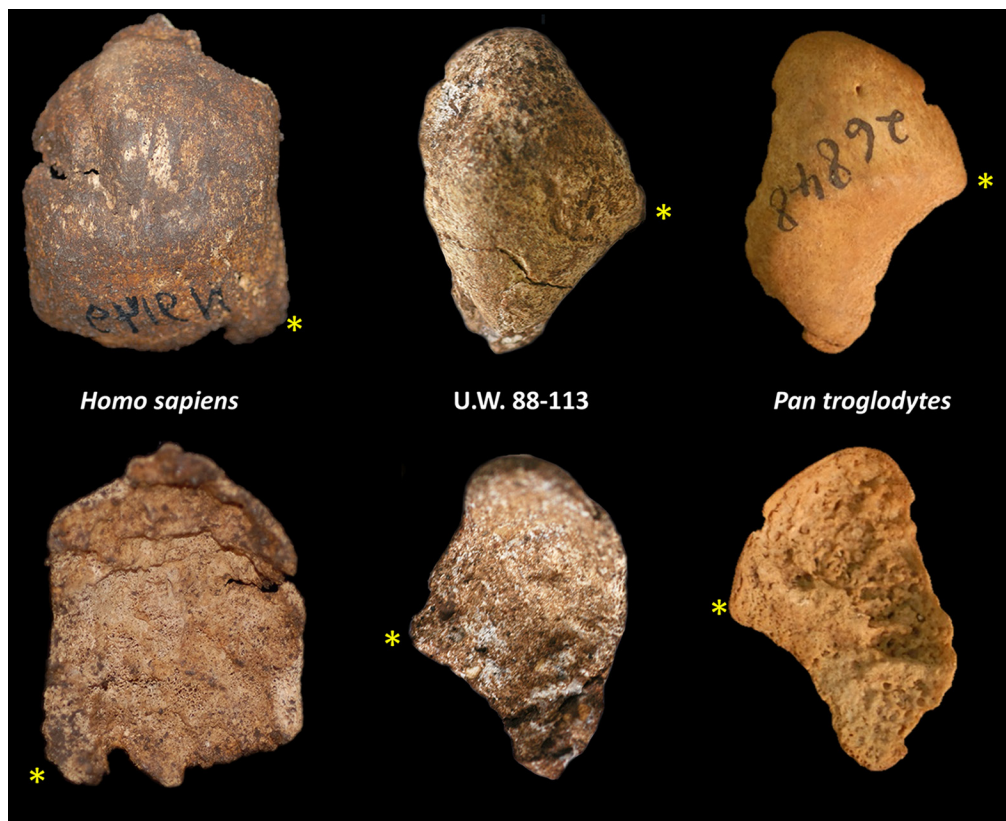


Figure 25. Calcaneal apophyses in proximal (top row) and distal (bottom row) views from (left to right): human, U.W. 88-113, and chimpanzee. The human has been reversed to reflect a right calcaneus. An asterisk notes the relative position of the apophyseal flange for the lateral plantar process. Notice that U.W. 88-113 is absolutely less broad ML than the human condition and possesses a more dorsally elevated flange for the lateral plantar process. The latter anatomy on the modern human apophysis, in comparison, is typically plantar in the adult condition.

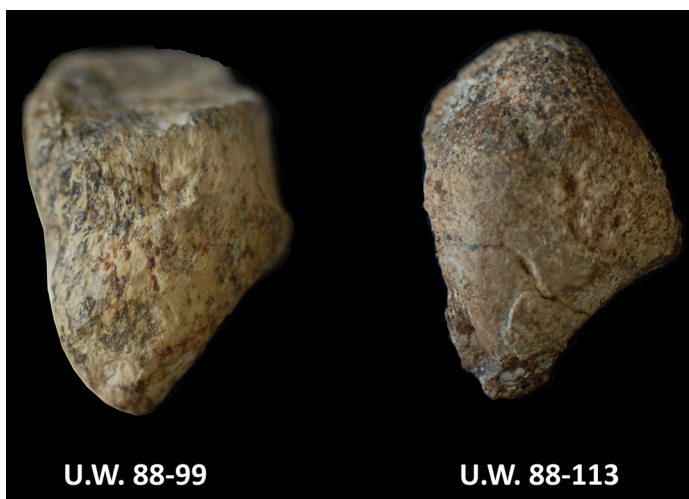


Figure 26. U.W. 88-99 and U.W. 88-113 shown proximoplantarly. U.W. 88-113 (right) possesses a dorsally elevated apophyseal flange, which eventually forms the lateral plantar process in the adult calcaneus. Both the juvenile MH1 and the adult MH2 share this general arrangement in calcaneal anatomy, including a dorsolaterally-angled orientation of the lateral plantar process. The 'beaked' medial plantar process is visible at the bottom of the image.

be a genetically encoded adaptation that acts to increase the overall volume of the calcaneal body to dissipate the internal stresses incurred during heel-striking bipedalism (Latimer and Lovejoy 1989). For this anatomy, *Au. afarensis* is modern human-like, making this aspect of the calcaneal anatomy of *Au. sediba* (both MH1 and MH2: see U.W. 88-113) ape-like and presumably primitive. While this anatomy may be relatively well-characterized in *Au. afarensis* (based on three specimens: A.L. 333-8, -37, -55), it is much less understood in *Au. africanus*. There is a single calcaneus from Sterkfontein Member 4 (StW 352) that has been sheared through the calcaneal body and unfortunately does not preserve the proximal tuberosity (McNutt et al. 2017), though like U.W. 88-99, it too appears to be quite gracile (Prang 2015). The calcaneus assigned to StW 573 does not preserve this anatomy (Deloison 2003).

Plantarily to the projecting lateral plantar process is a large concavity separating the lateral plantar process from the medial plantar process. The *M. abductor digiti minimi* muscle originates here in chimpanzees (Swindler and Wood 1973; Figure 30) and presumably would have done so in *Au. sediba*. Also, in lateral view, a strongly curved plantar surface, which creates a beak-like medial plantar process, is suggestive of an important role for the superficial head of the *M. flexor digitorum brevis*, a muscle thought

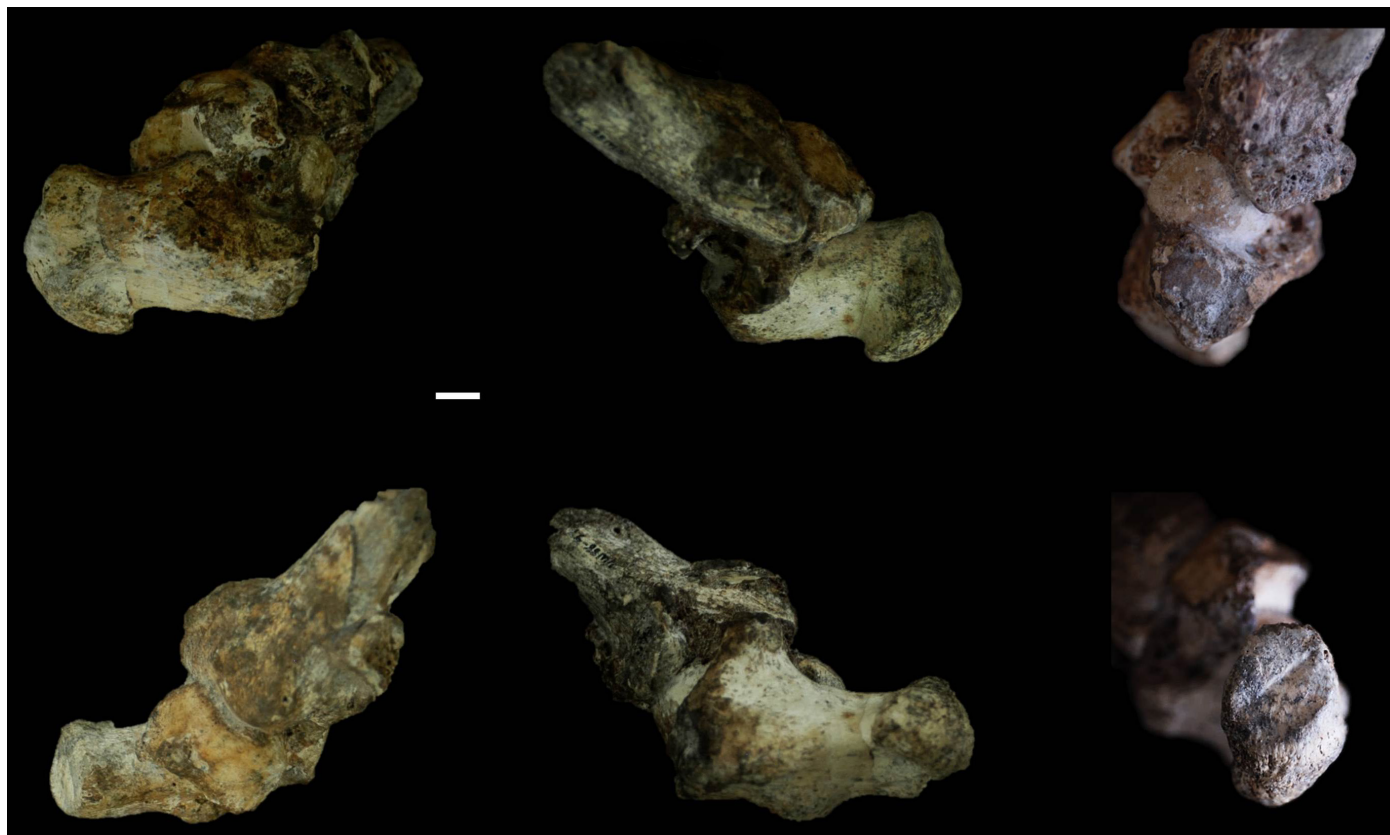


Figure 27. U.W. 88-99 calcaneus (cemented together with U.W. 99-97 distal tibia and U.W. 99-98 talus). Images are shown relative to the calcaneus. The top row (left to right) illustrates lateral, medial, and distal views. The bottom row (left to right) illustrates dorsal, plantar, and proximal views (scale bar=1cm).

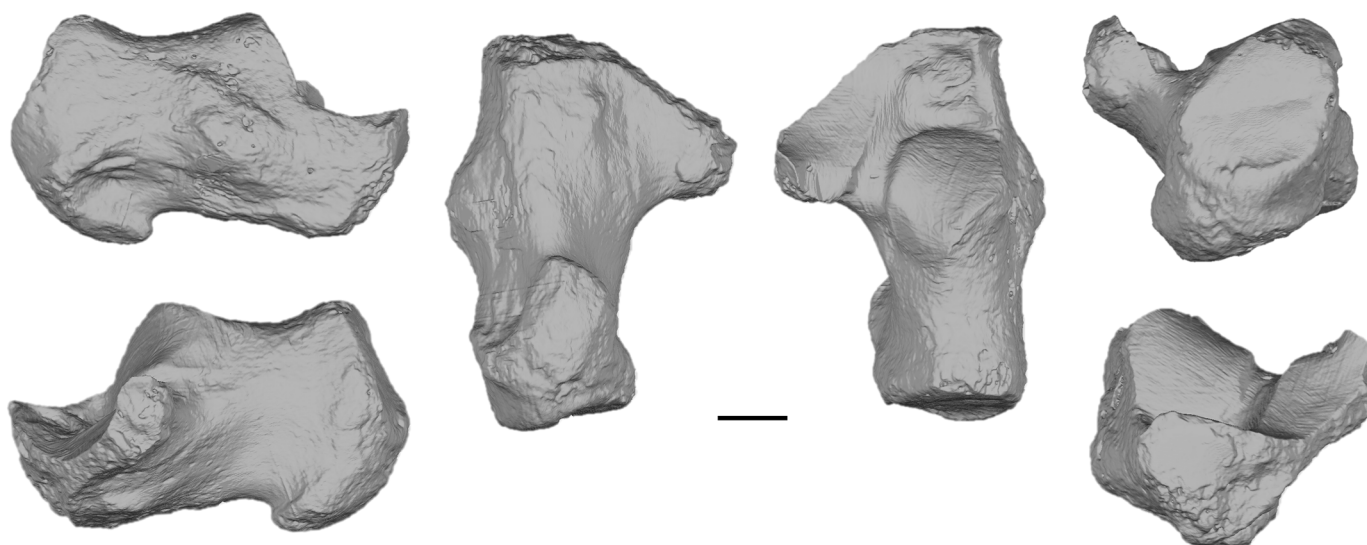


Figure 28.  $\mu$ CT renderings of the calcaneus (U.W. 88-99). From left to right: lateral (top), medial (bottom), plantar, dorsal, proximal (top), distal (bottom) (scale bar=1cm).

**TABLE 10. COMPARATIVE CALCANEAL MEASUREMENTS.**

Specimen	U.W. 88-99	A.L. 333-8	A.L. 333-37	A.L. 333-55	StW 352	Omo-33-74-896	OH 8	U.W. 101-1322
Maximum length of fragment	56.9	61.9	41.2	52	50.1	69.4	32.5	57
Posterior calcaneal length (Martin 1928)	43.7	46.8	-	46.4	-	51.9	-	42.7
Anterior calcaneal length (from anterior most point of posterior talar facet to anteriormost point of cuboid facet)	13.2	-	-	-	19	17.5	14.4	14.3
Maximum height of distal body (near cuboid facet)	23.1	-	-	-	19.1	27.4	17.1	17.7
Minimum DP height of distal body (at base of posterior talar facet)	19.4	17.3	-	17.6	16	19.5	13.8	15.6
Maximum dorsoplantar height of calcaneal tuberosity	33	38.1	33.5 <sup>1</sup>	38.8	-	-	-	-
Maximum mediolateral breadth of calcaneal tuberosity	21.8	22.7 <sup>1</sup>	24.6	23.6	-	-	-	-
Maximum mediolateral breadth of posterior talar facet	17.3	24.4 <sup>1</sup>	-	24.5 <sup>1</sup>	14.5	19.4	-	14.4
Maximum proximodistal length of posterior talar facet	19.8	29.8 <sup>1</sup>	-	-	22	28.4	-	20.8
Proximodistal length of sustentaculum tali base	19.5	25.5	-	-	19.4 <sup>1</sup>	21.4	17.9	20.2
Dorsoplantar height of sustentaculum tali base	9.1	11	-	-	9.8	9.3	9.6	8.8
Subtended angle of posterior talar facet	118°	82°	-	-	120°	87°	-	89°
Volume of posterior calcaneus (cm <sup>3</sup> )	13.4	28.7	-	29.8	-	-	-	15.4

Measurements of Hadar fossils from Latimer et al. (1982) compared with our observations on the original fossils. All others taken on original fossils.

<sup>1</sup>Estimates that approximate the actual value.

to be important in pedal grasping (Sarmiento 1983). The peroneal trochlea is well-developed, projecting ~4.5mm laterally from the main body of the calcaneus. The groove for the *M. peroneus brevis* is palpable just superior to the peroneal trochlea, though the groove for the *M. peroneus longus* inferior to the trochlea is not detectable. Just proximal to

the groove for peroneus brevis is a small pit for the calcaneofibular ligament. This pit is much deeper and more obvious on Hadar calcanei (e.g., A.L. 333-8, and A.L. 333-55).

The calcaneal tuberosity is gracile. At its minimum, the tuberosity is 25.9mm SI and 18.6mm ML. In proximal view, the tuberosity is ovoid in shape, and a maximum of 33mm

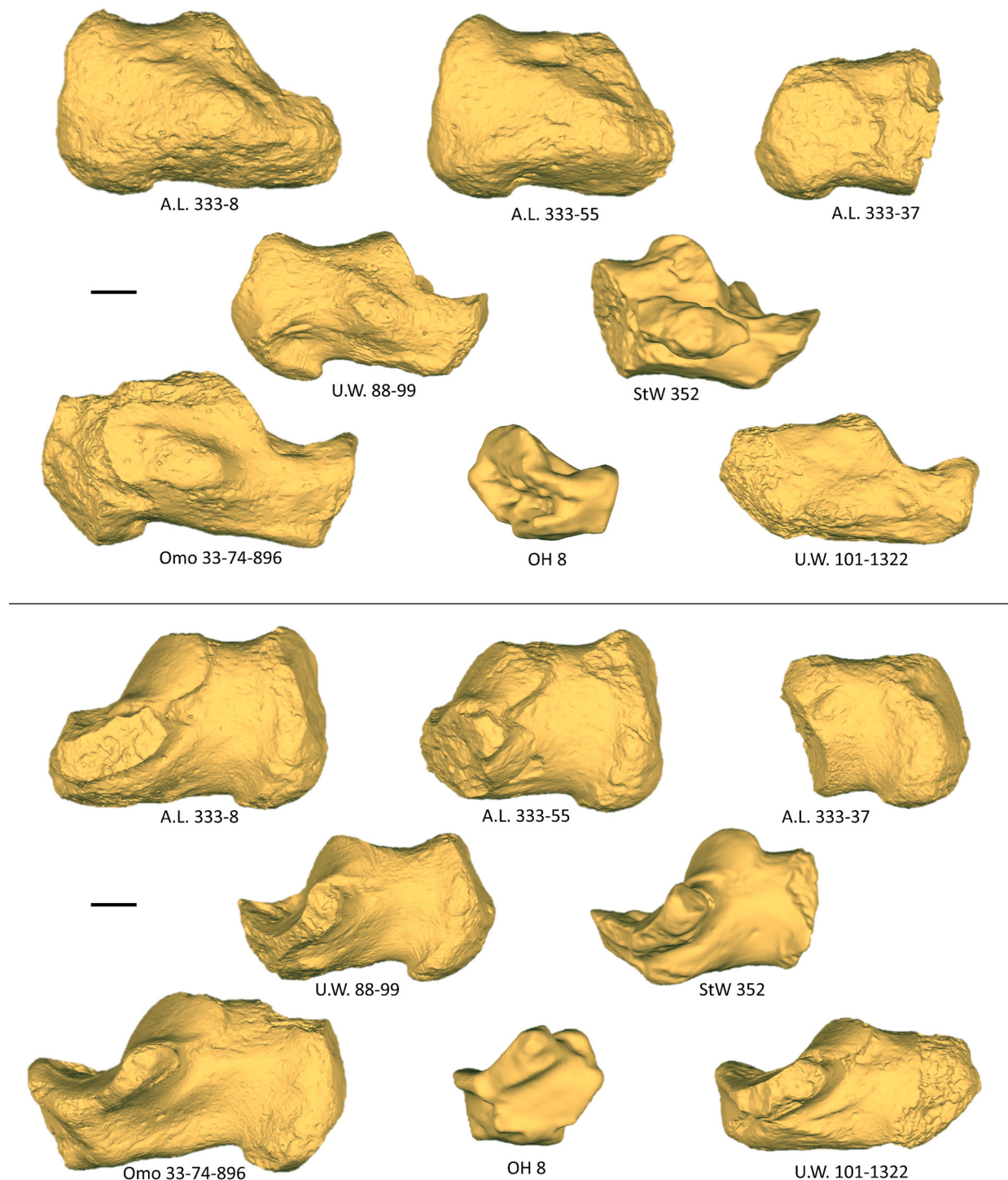


Figure 29. Hominin calcanei in lateral (top half) and medial (bottom half) views, mirrored to reflect the right side when necessary. Calcanei are exceptionally rare and often fragmentary. There are three calcanei from Hadar (A.L. 333-8, A.L. 333-37, A.L. 333-55); and single specimens from Omo (Omo 33-74-896), Malapa (U.W. 88-99), Sterkfontein (StW 352), and Olduvai (OH 8). Multiple calcanei are known from *Homo naledi*, though only the most complete one (U.W. 101-1322) is shown here. Notice the dorsally-positioned lateral plantar process in Au. sediba (plantarly positioned in the three Hadar calcanei). Note as well the plantarly-tilted cuboid facet of the Omo and OH 8 calcanei. The other calcanei are too fragmentary to characterize this morphology with certainty. The U.W. 88-99 calcaneus has a beak-shaped medial plantar process, though this anatomy can also be found on the calcaneus from Omo (scale bar=1cm).

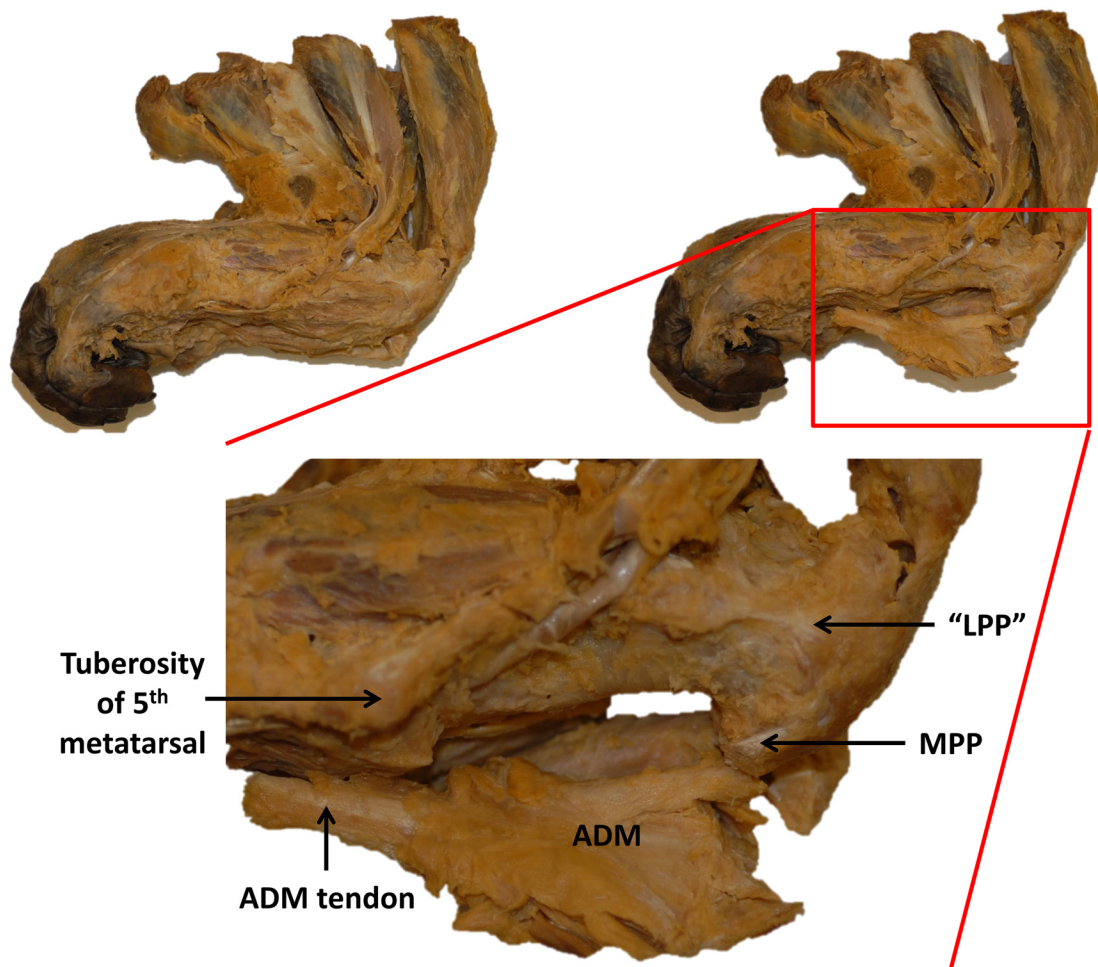


Figure 30. Muscular anatomy along the lateral aspect of the foot in a modern cadaveric chimpanzee. In the upper left image, the left foot of the chimpanzee is shown (dorsal surface facing upwards). In the upper right image, *M. abductor digiti minimi* has been reflected away from its origin along the lateral aspect of the calcaneus. The bottom image is a zoomed-in, detailed view of that anatomy. In this individual chimpanzee, the concave space between the medial plantar process (MPP) and the dorsally-elevated lateral plantar process, which is easily palpable, serves as the origin for the *M. abductor digiti minimi*, the tendon of which travels under the tuberosity of the fifth metatarsal. A similar calcaneal anatomy in *Au. sediba* suggests to us the presence of a similar role for *M. abductor digiti minimi* as occurs in modern chimpanzees.

SI and 21.8mm ML at its maximum. However, the ML maximum does not occur plantarly, as in humans or in other fossil hominins (e.g., A.L. 333-37; Figure 31), but instead the calcaneal tuberosity tapers plantarly. The broader dorsal part of the tuberosity is flat and divided into two facets by a groove progressing plantomedially to dorsolaterally. This groove demarcates a superior facet for the retrocalcaneal bursa and a middle facet that terminates inferiorly in a rugose insertion of the Achilles tendon (Kachlik et al. 2008). This rugosity is angled dorsolaterally (parallel to the superior groove), separating the middle facet from the inferior facet. Weak Sharpey's fibers can be felt within this rugosity, and are oriented perpendicular to the long axis of the calcaneal body. The superior facet for the retrocalcaneal bursa is 11.3mm SI at the midpoint of the calcaneus (31.9% of the total tuberosity height); the middle facet 10mm SI (28.2% of the total tuberosity height), and the inferior portion of the

bone 14.2mm SI. These proportions are human-like, which average a retrocalcaneal bursa facet SI of 26.9% and middle facet SI of 31.8% (n=10 humans).

In dorsal view, the tuberosity is long and narrow. Relative to the long axis of the bone, the insertion for *M. triceps surae* is medially-deviated 13°. Unlike in apes and *Au. afarensis*, the calcaneus does not 'flex' at the peroneal trochlea and instead remains straight, as it does in most humans. The posterior talar facet of the 3D printout is strongly convex PD and slightly concave ML. It faces distomedially, essentially in line with the long axis of the calcaneus as in humans, and unlike the more medially-angled facet found in modern apes. The talar facet comprises an arc with a radius of curvature of 11.6mm, and a joint subtended angle of 118.3°, similar to the mobile subtalar joint found in chimpanzees and gorillas (Latimer and Lovejoy 1989; Zipfel et al. 2011) and in StW 352 (see Table 10), but quite distinct from

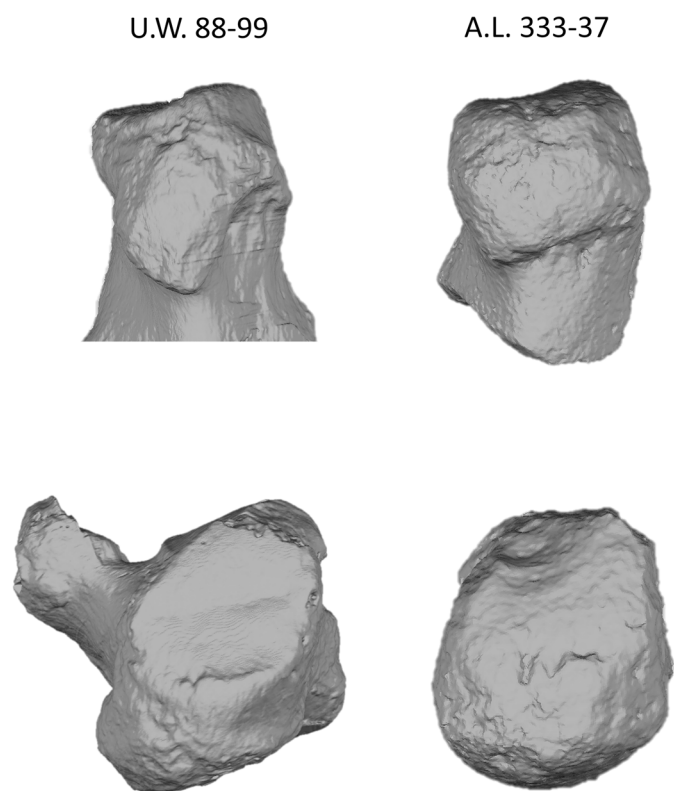


Figure 31. U.W. 88-99 (left side) and the similarly-sized A.L. 333-37 calcaneus (right side) from Hadar. These are shown in plantar (top) and proximal (bottom) views. Notice that in the *Au. sediba* calcaneus, the medial plantar process terminates inferiorly in a beak-like anatomy, while in the Hadar calcaneus, medial and lateral plantar processes merge into a mediolaterally widened inferior margin that effectively creates an enlarged heel. In proximal view, the difference in breadth of the inferior margin results in the widest part of the calcaneal tuberosity being in a much more human-like plantar position in the Hadar calcaneus (*Au. afarensis*) than in *Au. sediba*. This comparison should assuage concerns that the anatomy of U.W. 88-99 is because of its small body size.

the condition in modern and some fossil hominins (A.L. 333-8, Omo 33-74-896), suggesting considerable subtalar joint mobility in *Au. sediba* and *Au. africanus* (Prang 2016). The posterior talar facet on the 3D printout is 17.3mm ML and 19.8mm PD. The anterior articular facet for the talus is teardrop-shaped, and combines the anterior and middle talar articular surfaces (Type B variant in Kelikian 2011). The conjoined facet is roughly 19.7mm PD and a maximum of 11.1mm ML. The distance from the distal edge of the posterior talar facet and the cuboid facet is a relatively short 14.3mm PD.

Medially, the plantar tuberosity is dominated by a strongly-beaked medial plantar process. The calcaneal tuber is concave PD and generally smooth. The sustentaculum tali projects laterally 11.8mm from the calcaneal body and is weakly angled distoplantarly. The groove for the *M.*

*flexor hallucis longus* is shallow, but wide—4.5mm ML. Plantarily, the medial plantar process extends 22.7mm distally from the calcaneal tuberosity. There is a rugosity 33.4mm from the proximal end of the calcaneal tuberosity for origin of the long plantar ligament, an important ligament stabilizing the midfoot. This rugosity is also present on calcanei from Hadar and Omo (Gebo and Schwartz 2006). An anterior tubercle appears to be present, though heavy erosion distoplantarly prevents accurate assessment of the origin of the short plantar ligament.

Only a 13.4mm ML and 9.8mm DP portion of the cuboid articular surface is preserved, which is concentrated dorso-laterally. There is a ridge of bone plantolaterally delineating the rim of the calcaneocuboid joint. Medially, the facet appears to extend towards the sustentaculum tali, though the facet does not appear to extend as far proximally and medially onto the calcaneal body as it does in humans with a calcaneocuboid locking mechanism (Bojsen-Møller 1979). Nevertheless, there is no concavity in this area, making it unlike ape calcanei, which are crescent-shaped in this region and often possess an indentation for the cuboid beak. The preserved part of the cuboid facet is moderately concave DP and flat ML.

## METATARSALS OF MH1

### U.W. 88-22

U.W. 88-22 is a right 4th metatarsal (Figure 32; Table 11). It is most likely associated with U.W. 88-16. It has been tentatively assigned to MH1. U.W. 88-22 preserves 48.3mm from the base to the distal end of the shaft, terminating immediately prior to the expansion of the shaft for the missing metatarsal head. The estimated total length of the bone is 56mm based on comparisons to a similarly-sized human fourth metatarsal. At the most distally preserved end, there is a portion of roughened surface that may constitute the epiphyseal surface for an unfused metatarsal head, though this is not certain. There is heavy erosion around the surface of the bone with flakes removed, primarily along the lateral aspect of the shaft and base. Plantar and lateral aspect of the base exhibit damage, including shearing off of the plantar-most lateral corner of the base.

Midshaft external dimensions are 5.5mm ML and 6.5mm DP. Following Pontzer et al. (2010), we calculated a robusticity value based on the DP height of the shaft, its estimated length, and an estimated body mass (35 kg from Holliday et al. 2018). U.W. 88-22 has a robusticity value of 2.2, which is within the overlapping range of values found in humans and the African apes. A midshaft ML/DP ratio of 0.85, which is higher than that found in humans and A.L. 333-160 (Ward et al. 2012), is instead more African ape-like.

The base is angled approximately 95° distomedially relative to the shaft. Without the head, and considering damage along the lateral surface of the shaft, it is difficult to quantify torsion. Since torsion begins quite proximally on the human fourth metatarsal, even fragmentary hominin metatarsals can yield qualitative assessments of fourth metatarsal torsion. Like other fragmentary fourth meta-



Figure 32. U.W. 88-22 is illustrated in (from left to right): dorsal, lateral, plantar, medial, distal (top far right), and proximal (bottom far right) views. Notice the convex base in lateral and medial views (scale bar=1cm).

tarsals (StW 485, OH 8), the shaft appears to externally twist distally. We were able to successfully replicate both the methods and the value calculated for another headless fourth metatarsal (OH 8), reported as 25° by Pontzer et al. (2010). Applying the same approach to U.W. 88-22, we obtained a value of approximately 19° of external torsion, which is similar to the 17° reported for A.L. 333-160 (Ward et al. 2012). Therefore, we cautiously suggest that U.W. 88-22 may have possessed external torsion of the fourth metatarsal head, as is demonstrated in other hominins and humans (Drapeau and Harmon 2013; Ward et al. 2011).

The preserved cuboid facet is ML flat, and DP convex. The base is a minimum of 12.5mm DP and 9.3mm ML. The ML/DP ratio (from Ward et al. 2012) is 0.74, which places U.W. 88-22 within the overlapping human and African ape distributions and similar to other australopiths (but not BRT-VP-2/73a). Using the DP/4th metatarsal length ratio from Haile-Selassie et al. (2012), U.W. 88-22 is 0.22, again falling within the overlapping human and African ape range, and different from both BRT-VP-2/73a (which has a more African ape-like, gracile base) and A.L. 333-160 (which has a more human-like, robust base). Despite having a base that falls within the human range of distribution for measures of robusticity, U.W. 88-22 has unusual convexity to its cuboid facet (quantified in DeSilva et al. 2013).

A convex base of the fourth metatarsal is evidence for a midtarsal break, or midfoot flexion (DeSilva 2010; DeSilva et al. 2015). A mobile midfoot that dorsiflexes at the tarso-metatarsal joint was thought to be unique to non-human primates (DeSilva 2010; Elfman and Manter 1935). Recent work, however, has shown that humans can, and often do, have a midtarsal break (Bates et al. 2013; Crompton et al. 2012; DeSilva and Gill 2013; DeSilva et al. 2015). Perhaps more importantly, DeSilva and Gill (2013) found that humans with a midtarsal break are more likely to have either a flatfoot, or to excessively pronate. Given other skeletal evidence that *Au. sediba* had both a flat foot (Prang 2015), and that *Au. sediba* may have excessively pronated during bipedal walking (DeSilva et al. 2013), these findings relating hyperpronation to the midtarsal break, and skeletal evidence for a midtarsal break in the form of a convex base to U.W. 88-22 support the hypothesis that *Au. sediba* was a hyperpronating biped. This species-level characterization of bipedal locomotor kinematics is reinforced by the fact that U.W. 88-22 does not belong to MH2 (the skeletal basis for much of the hyperpronating hypothesis in DeSilva et al. 2013) and likely belongs to MH1.

Medially, the articular surface for the third metatarsal is flat and 6.8mm PD and 6.2mm DP. It grades into the more proximal facet for the lateral cuneiform which is 2mm PD. Therefore, there appears to be some recessing of the fourth metatarsal into the tarsal row, as is found in humans and other australopiths (Ward et al. 2011), though the small facet for the lateral cuneiform is not angled as it is in most humans, A.L. 333-160, StW 435 (*Au. africanus*), or OH 8, and therefore the tarsometatarsal joint may not have been as stiff as that of *Au. sediba*. This would be consistent with other evidence (DP convex base; weak talar head torsion) for a more mobile midfoot in this species. Plantar to these facets is a pit for the interosseous ligaments. Laterally, the facet for the fifth metatarsal is flat and approximately 5.4mm PD and 8.5mm DP, though plantar damage precludes a definitive measurement. Distal to the facet (and 10.6mm from the base) is a large tuberosity for the interosseous metatarsal ligament. There is a pronounced groove separating the fifth metatarsal facet and the tuberosity for the interosseous ligaments. In lateral view, there is slight curvature to

**TABLE 11. HOMININ FOURTH METATARSAL MEASUREMENTS.**

Fossil	Maximum preserved length	DP depth of base	ML breadth of base	DP midshaft	ML midshaft	Torsion	Reference
U.W. 88-22	47.9	13.4	9.3	6.5	5.5	~19°	This study
BRT-VP-2/73a	68.7	13.3	12.7	9.2	5.4	26–27°	Haile-Selassie et al. (2012)
A.L. 333-160	59.9	17.1	13.1	9.1	6.1	17°	Ward et al. (2012)
StW 485	27	14.1	8.9 <sup>1</sup>	-	-	-	This study
OH 8	40.6	15.4	10.2	8.4	6.4	25°	This study and Pontzer et al. (2010)
D2669	59.1	-	-	8.6	-	29°	Pontzer et al. (2010)
U.W. 101-269	59	13.1	9.5	7.5	6.5	35°	Harcourt-Smith et al. (2015)
U.W. 101-1456	59	16	10.6	7.6	6.7	38°	Harcourt-Smith et al. (2015)

<sup>1</sup>Minimum measurements that underestimate the actual value.



Figure 33. U.W. 88-16 is illustrated along the top in (from left to right) dorsal, plantar, lateral, medial, distal (top far right), and proximal (bottom far right) views. It is most likely associated with U.W. 88-22, a right fourth metatarsal. These two are shown in articulation at the bottom left of the figure. For comparison with U.W. 88-16 and U.W. 88-22, associated fourth and fifth metatarsals (reversed so that they all appear from the right side) of OH 8, and U.W. 101-1456 and U.W. 101-1439 from *Homo naledi* are also illustrated in articulation (scale bar=1cm).

the plantar surface of the shaft, while the dorsal surface of the shaft is straight.

#### U.W. 88-16

U.W. 88-16 is a fragmentary right 5th metatarsal (Figure 33;

Table 12). It is most likely associated with U.W. 88-22, and has been tentatively assigned to MH1. It preserves 46.3mm PD of the shaft, and is estimated to be ~57mm in total length based on comparisons with a 5th metatarsal of a small-bodied modern human foot and to the complete StW 114/115 metatarsal from Sterkfontein (Zipfel et al. 2009). The head, the base, and the tuberosity are missing. The bone is broken proximally just distal to the facet for the fourth metatarsal, and laterally just distal to the tuberosity.

At roughly midshaft, external dimensions are 4.8mm DP, and 6.9mm ML, making it quite DP compressed. Following Pontzer et al. (2010), we calculated a robusticity value based on the DP height of the shaft, its estimated length, and an estimated body mass (~35kg based on Holliday et al. 2018). U.W. 88-16 has a robusticity value of 1.15, which is barely within the human range of values and closer to the range of values observed in African apes. This is contrasted with the robusticity of Mt IV (U.W. 88-22), which has a higher value of 2.2. Greater robusticity of Mt IV than Mt V is unusual in humans (only 8% of humans in the sample by Archibald et al. 1972) though comparatively low robusticity of the Mt V also characterizes the Dmanisi foot (Dowdeswell et al. 2017; Pontzer et al. 2010). The OH 8 foot, in contrast, possesses relatively low Mt IV robusticity (Archibald et al. 1972; Patel et al. 2018)

The dorsal surface of U.W. 88-16 is flat, and in dorsal view there is very slight lateral curvature, though this is concentrated proximally near where the tuberosity would have been. Strong lateral curvature present in many hominin 5th metatarsals is absent in this specimen (see Figure 33). Along the proximomedial surface of the shaft, which is strongly ML convex, there is a slight rugosity, perhaps for the *M. peroneus tertius*. Also in medial view, there is a slight dorsal concavity (plantar convexity), as can be found in many human 5th metatarsals. Laterally, the shaft is ML convex, and there is a subtle rugosity plantarly. The plantar surface is quite flat, and there is an elevation along the most lateral and proximal part of the preserved plantar surface, which is all that is preserved of the tuberosity.

TABLE 12. HOMININ FIFTH METATARSAL SHAFT DIMENSIONS (from Zipfel et al. 2009).

*Specimen	Midshaft width (ML)	Midshaft height (DP)	Ratio (DP/ML)*100
A.L. 333-13	9.4	7.3	77.7
A.L. 333-78	7	6.4	91.4
StW 114/115	8.7	7.4	85.1
U.W. 88-16	6.9	4.8	70
OH 8	7.2	5.8	80.6
SKX 33380	8.9	7.3	82
U.W. 101-518	8.4	5.3	63.1
U.W. 101-1412	8	6.1	76.3
U.W. 101-1439	8.1	5.4	66.7



Figure 34. U.W. 88-33 is illustrated in (from left to right): anterior, posterior, lateral, medial, and proximal views (scale bar=1cm).

## METATARSAL UNASSIGNED TO INDIVIDUAL

### U.W. 88-33

U.W. 88-33 is 31.9mm of a right 5th metatarsal, in two conjoined pieces (Figure 34). It has been briefly described elsewhere (Zipfel et al. 2011). It was found *ex situ* in the Miner's dump (Val 2014). Though it does appear to be from an adult, this bone is not clearly associated with either MH2 or MH4.

The most distal piece of the shaft is a maximum of 16.6mm long and fits cleanly with the base. Plantomedially there is exfoliation of cortical bone. The shaft is 10.4mm ML and 7.5mm DP just prior to the expansion to the tuberosity. Medially, the 4th Mt facet is flat and 6.8mm DP and 7.6mm PD. Proximally, the cuboid facet is flat both DP and ML. It is 9.1mm DP and 7.9mm ML. Base dimensions are presented in Table 13. Laterally there is a projecting tuberosity for the insertion of *M. peroneus brevis*. Dorsally, the base possesses small roughened regions for the dorsal metatarsal ligaments. Plantarly, there is a sulcus for the tendon of *M. abductor digiti minimi*. Immediately medial to the sulcus there is a large tubercle for the origin of the *M. flexor digiti minimi brevis* muscle. The tubercle is situated precisely

where the muscle insertion is plotted on a map of the foot in Logan et al. (2004). This tubercle for the origin of the *M. flexor digiti minimi brevis* is decidedly larger than the corresponding tubercle of other hominin fifth metatarsals (StW 114/115, A.L. 333-13, A.L. 333-78, KNM-ER 803, and OH 8; Figure 35), and suggests an important role of this muscle in the locomotion of *Au. sediba*. Combined with the large area on the calcaneus for the origin of *M. abductor digiti minimi*, this australopith appears to have possessed strong plantar musculature in the lateral midfoot.

## DISCUSSION AND CONCLUSION

As in other australopiths (Ward et al. 2015), the femoral neck of *Au. sediba* is long and anteroposteriorly compressed. The superoinferior height of the femoral neck is slightly smaller than expected for an australopith of its size, though MH1 and MH2 both fall within the range of variation exhibited by *Australopithecus* (see Figure 4). However, the preserved ilium from MH2 appears to lack the extreme lateral flaring found in australopiths, or even in early *Homo* (Churchill et al. 2018; Kibii et al. 2011). The current reconstruction of the hip joint of *Au. sediba* presents a combination of a long-necked femur with a more vertically-oriented ilium (in the sagittal plane) not found in other australopiths. The biome-

TABLE 13. BASE DIMENSIONS OF HOMININ FIFTH METATARSALS.

<sup>1</sup> Specimen	Maximum base width (ML)	Maximum base height (PD)	Base ratio
A.L. 333-13	18.1	12.1	66.9
A.L. 333-78	15.7	11	70.1
StW 114/115	16.5	11	66.7
U.W. 88-33	16	12	75
OH 8	12.2	9.6	78.7
KNM-ER 803	20.3	12	59.1
U.W. 101-518	15	10	66.7
U.W. 101-1439	13.1	8.3	63.1

<sup>1</sup>As reported in Zipfel et al. (2009) except for U.W. 88-33 and Dinaledi fossils (Harcourt-Smith et al. 2015). *Australopithecus* has a relatively conserved base shape (n=3). The proximodistally expanded height of the *Au. sediba* base is entirely explained by the large tubercle for the *M. flexor digiti minimi brevis*. The high ratio in OH 8 is not a function of a tall base, but rather a pathology-induced truncated width.

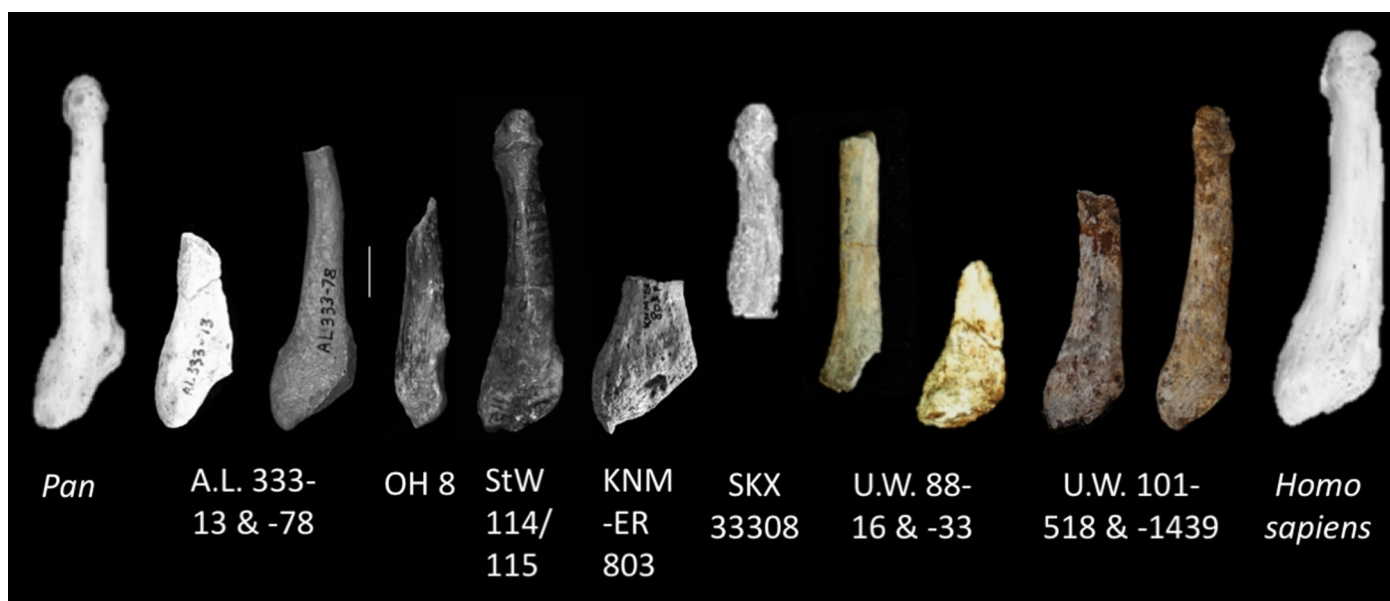


Figure 35. Hominin fifth metatarsals compared to those of *Pan* (far left) and a modern human (far right). Both U.W. 88-16 and U.W. 88-33 (described later in the text) are from the right side and have been reversed so as to be illustrated as from the left side for this comparison. Notice the lateral concavity of the shaft evident in the human, A.L. 333-78, StW 114/115, and SKX 33308, appears to be relatively undeveloped in U.W. 88-16 (figure modified from Zipfel et al. 2009; scale bar=1cm).

chanical consequences of such a combination are unknown. However, the combination of a long femoral neck and wide biacetabular diameter in the absence of iliac flaring is suggested to increase both the contractile force of the abductors and the hip joint reaction force (Ruff 1995). Additionally, mediolateral bending moments around the proximal femoral shaft and the midshaft are predicted to increase (Ruff 1995). These predictions are based solely on *Au. sediba* body dimensions of a generic biped. More work will clearly be needed to understand the functional significance of this hip joint, given these unexpected combinations.

The knee of *Au. sediba* is well-preserved, but is missing a portion of the distal shaft and medial condyle. These parts were digitally reconstructed (see Figure 8). The *Au. sediba* distal femur possesses australopith-like condyles, but is distinct in its anatomy of the patellar surface. While the anterior projection of the lateral patellar lip in *Au. sediba* is *Homo*-like, it remains australopith-like in lacking the anterior projection of the patellar surface (DeSilva et al. 2013; see Figure 8). No other hominin distal femora, including those generally assigned to *Au. africanus* (TM 1513, Sts 34, StW 129, StW 318), possess this combination of characteristics, which indicates that *Au. sediba* has a (presently) unique combination of features that may be reflective of unique locomotor kinematics, particularly during bipedal gaits (Zhang and DeSilva 2018). As we have argued elsewhere (DeSilva et al. 2013), a high lateral patellar lip would help patellar tracking within the patellar groove during medial (internal) rotation of the femur, a corollary of a hyperpronating bipedal gait in modern humans (Tiberio 1987). Additionally, this bony anatomy could compensate for a weak or absent *M. vastus medialis obliquus* in the knee of *Au. sediba*.

The unique femoral anatomy of *Au. sediba* may yield insight into the evolutionary history of the knee joint in hominins (Figure 36). If *Au. sediba* is a sister taxon to *Homo*, then the lateral lip of the patellar groove may have extended first in relative timing, prior to the anterior expansion of the patellar surface. Only in *Homo* are both the extended lateral lip of the patellar groove and the anterior expansion of the patellar surface present. However, if *Au. sediba* and *Au. africanus* are sister taxa, and *Au. sediba* is evolutionarily unconnected to *Homo*, then the anteriorly projecting lateral patellar lip of U.W. 88-63 is likely an autapomorphic anatomy in *Au. sediba*, reflecting gait kinematics unlike that found in other hominins.

The articulated rearfoot of MH2 has been  $\mu$ CT scanned and digitally segmented, producing more accurate renderings of these bones than previously reported. Our anatomical assessment of these bones and functional interpretation of their morphologies (DeSilva et al. 2013; Zipfel et al. 2011) remain essentially unchanged. Both the MH1 calcaneal apophysis and the MH2 adult calcaneus possess a primitive development of the calcaneal tuberosity, resulting in a dorsally-positioned lateral plantar process, quite unlike the anatomy characterizing *Au. afarensis* (Latimer and Lovejoy 1989; Zipfel et al. 2011; see Figures 29 and 31).

Thus, the calcaneus of *Au. sediba* presents an interesting evolutionary dilemma. Figure 37 illustrates the cladistic relationship between *Homo*, *Au. sediba*, *Au. afarensis*, and *Pan troglodytes* (Berger et al. 2010; Dembo et al. 2016; Irish et al. 2013). There are four scenarios to explain the more primitive Malapa calcanei given the hypothesized relationship between these taxa:

1. The gracile calcaneal body and primitive geometry of

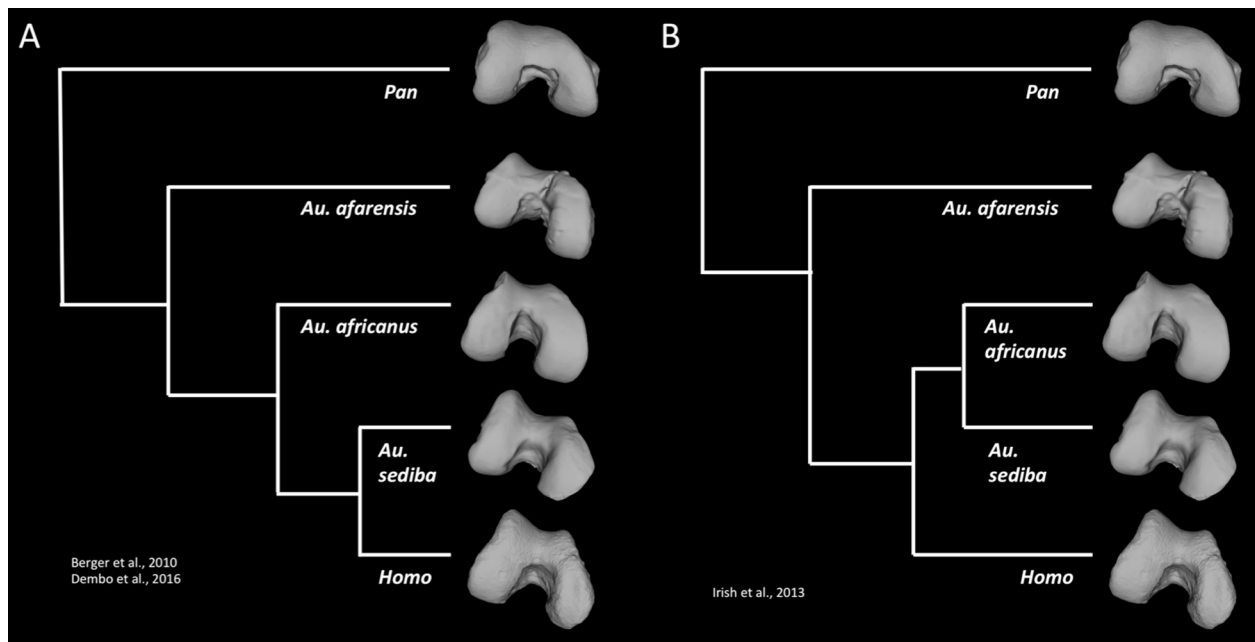


Figure 36. Evolutionary history of the distal femur. Cladistic analyses that have included the Malapa material find that *Au. sediba* is either the sister taxon to *Homo* (Berger et al. 2010; Dembo et al. 2016) or the sister taxon to *Au. africanus* (Irish et al. 2013). Lovejoy et al. (2007) identified a difference between the *Australopithecus* knee and that of *Homo* being the anterior expansion of the patellar surface in *Homo*. A) If *Au. sediba* is the sister taxon to *Homo*, it is most parsimonious that the anterior expansion of the patellar surface happened in a mosaic fashion, with the anterior projection of the lateral patellar lip (present in *Au. sediba*) preceding the anterior expansion of the patellar surface itself (present in *Homo*). B) If *Au. sediba* and *Au. africanus* are sister taxa, it is most parsimonious to suggest homoplasy of the anteriorly projecting lateral patellar lip in *Au. sediba* and *Homo*. This assumes that the shared common ancestor of *Au. sediba* and *Homo* did not have this feature (a statement supported by the absence of an anteriorly projecting lateral patellar lip in other australopiths). In this scenario, *Au. sediba* possesses an autapomorphic anatomy specifically adapted to prevent patellar subluxation due to a different biomechanical environment of the knee in this species (DeSilva et al. 2013), or a less developed *M. vastus medialis obliquus* than might exist in *Homo*.

the calcaneal tuber represents an evolutionary reversal in the *Au. sediba* lineage. While the robust calcaneal tuber may be important for bipedalism (Latimer and Lovejoy 1989), and there is strong evidence that *Au. sediba* was bipedal (Berger et al. 2010; Kibii et al. 2011; Williams et al. 2013; Zipfel et al. 2011), *Au. sediba* may have been more variable and less stereotyped in how the foot contacted the substrate during terrestrial bipedal walking. In this scenario, the anatomy of the *Au. sediba* calcaneus would be the result of non-trivial selection on foot anatomy as part of a broader selective regime for utilizing arboreal resources.

2. The cladistic relationship presented here is incorrect and *Au. afarensis* is more closely related to *Homo* than is *Au. sediba*. This scenario eliminates the need for any evolutionary reversal and represents the *Au. sediba* calcaneus as symplesiomorphic, retaining the more ape-like gracile calcaneus (albeit somewhat enlarged as a result of its bipedal locomotion). If this scenario is correct, the human-like calcaneal body evolved once in eastern African australopiths. Though plausible, this scenario would necessitate independent acquisition of *Homo*-like craniodental (Berger et al. 2010; de Ruiter et al. 2013; de Ruiter et al. 2018; Irish et al. 2013),

vertebral (Williams et al. 2013; Williams et al. 2018), pelvis (Churchill et al. 2018; Kibii et al. 2011), and hand (Kivell et al. 2011; Kivell et al. 2018) anatomy in the *Au. sediba* lineage.

3. The cladistic relationship presented here is correct (Berger 2010; Berger et al. 2012; Dembo et al. 2016; de Ruiter et al. 2013; de Ruiter et al. 2013; Irish et al. 2013) and the human-like calcaneus of *Au. afarensis* evolved in parallel in *Au. afarensis* and *Homo*, meaning that adaptations for heel-striking bipedalism may have evolved at least twice, as posited elsewhere (Prang 2015). Note that in any of these scenarios, there is divergence in bipedal kinematics both between and within eastern and southern Africa australopiths and evidence for locomotor variation (Carlson and Su 2017; DeSilva et al. 2013; Dowdeswell et al. 2017; Haile-Selassie et al. 2012; Harcourt-Smith and Aiello 2004; Zipfel et al. 2011).
4. A final scenario would posit that australopiths were highly polymorphic for calcaneal anatomy with some individuals possessing more gracile calcaneal tubers (like U.W. 88-99 and U.W. 88-113) and others (like A.L. 333-8, A.L. 333-55, A.L. 333-37) possessing more human-like calcaneal bodies. The association between

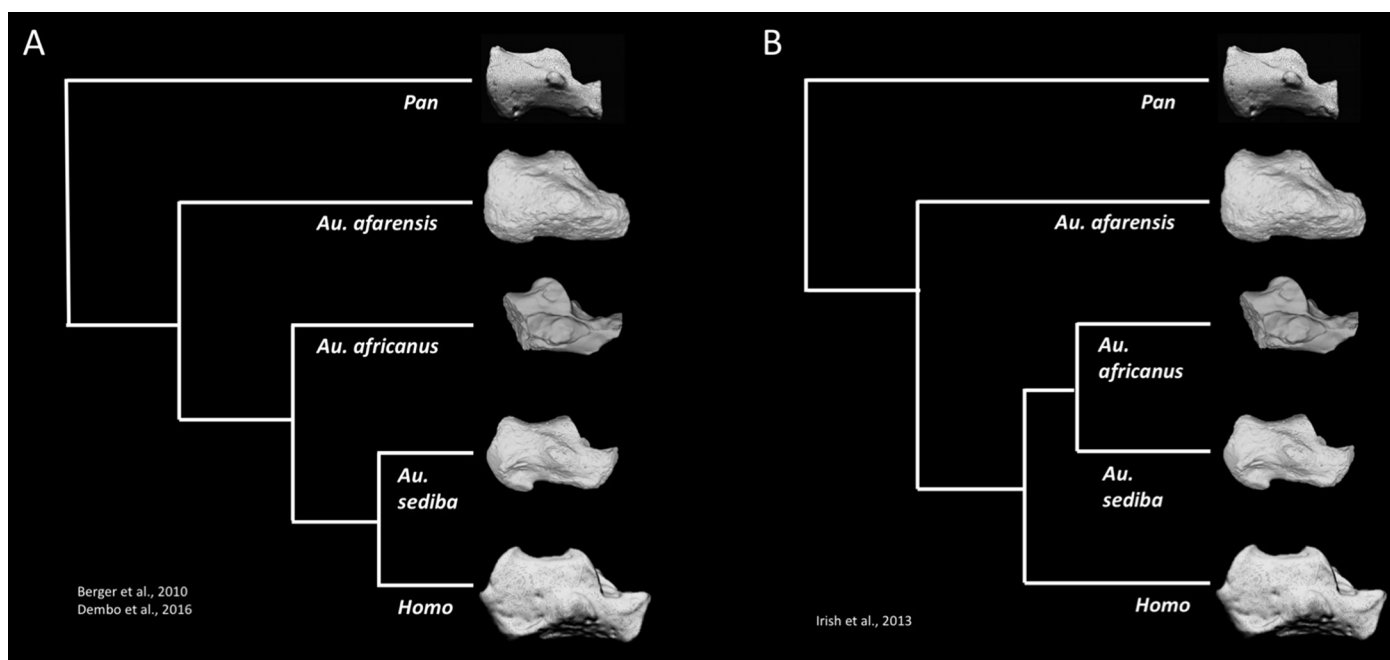


Figure 37. Evolutionary history of the calcaneus. Cladistic analyses that have included the Malapa material find that *Au. sediba* is either the sister taxon to *Homo* (Berger et al. 2010; Dembo et al. 2016) or the sister taxon to *Au. africanus* (Irish et al. 2013). Given these alternative relationships, there are several possible explanations for the seemingly more derived calcaneus of *Au. afarensis* (Zipfel et al. 2011). 1) The heel of *Au. sediba* experienced an evolutionary reversal. 2) Cladistic analyses performed thus far are incorrect; *Au. afarensis* is the sister taxon to *Homo* and the *Au. sediba* calcaneus is symplesiomorphic, retaining an ape-like gracile calcaneus. 3) The human-like calcaneus of *Au. afarensis* evolved in parallel in *Au. afarensis* and *Homo*, meaning that adaptations for heel-striking bipedalism may have evolved at least twice. 4) Australopiths were highly polymorphic for calcaneal anatomy and that the differences between the Malapa and Hadar calcanei are sampling artifacts. Notice here that the proximal calcaneal tuber remains missing in fossils assigned to *Au. africanus*.

calcaneal morphology and particular species (like *Au. sediba* and *Au. afarensis*) would be the consequence of sampling error. Over time, directional selection would result in a more robust average calcaneus (Latimer and Lovejoy 1989) as any ape-like calcanei would reduce in frequency in the breeding population. Considerably larger samples of hominin calcanei—especially contemporaneous ones—would be needed to assess how variable calcaneal morphology has been through evolutionary time.

3D geometric morphometrics were applied to the Malapa fossils, as has been done with other hominin tarsals (e.g., Harcourt-Smith 2002; Jungers et al. 2009; Prang 2016). U.W. 88-99 falls between *H. sapiens* and *G. gorilla* in the morphospace regardless of whether or not estimations for two damaged landmarks on the cuboid facet are included (Figures 38A and 38B). Increasingly positive values along PC 1 (43.5% of variance) correspond with a distal shift of the peroneal trochlea, a more plantarly-positioned lateral plantar process, and an overall expansion of the posterior calcaneal tuber. Increasingly positive values on PC2 (13.3% of variance) correspond to a medial shift of the peroneal trochlea and an elongation of the posterior tubercle. When additional fossil calcanei (A.L. 333-8, A.L. 333-55) are included, calcanei typically assigned to *Au. afarensis* cluster with *H. sapiens*, while *Au. sediba* falls in the space between

*H. sapiens* and African apes (Figure 39). Thus, the MH2 calcaneus possesses a mosaic of features—an ape-like positioning and development of the plantar tubercles, but other human-like anatomies that are functionally important for bipedal locomotion. Ultimately, regardless of divergent morphologies of the plantar tubercles, *Au. sediba* was bipedal and the calcaneus, in part, reflects those functional demands.

The MH2 talus displays a similar mosaic in being human-like in many respects, but ape-like in others, and thus falls between humans and extant African apes in 3D morphospace (Figure 40), although it is important to note that its overall shape is outside that of the modern human range of variation. Anatomies driving PC1 (26% of variance) toward apes include keeling and oblique orientation of the talar trochlea, size of the talar head, and curvature of the posterior calcaneal facet. Anatomies driving PC2 (12.6% of variance) toward *Pongo* include a smaller talar head, a longer talar neck, and a flatter, more vertical lateral malleolar facet. While the *Au. sediba* talus is human-like in having a flat trochlea and a human-like talar axis angle (see Figure 22), it is more ape-like in having a head with minimal torsion and additional morphology suggesting greater mobility in the subtalar joint (Prang 2016; Zipfel et al. 2011).

On the whole, the *Au. sediba* foot is a fine example of a foot adapted for bipedalism, but in a different anatomi-

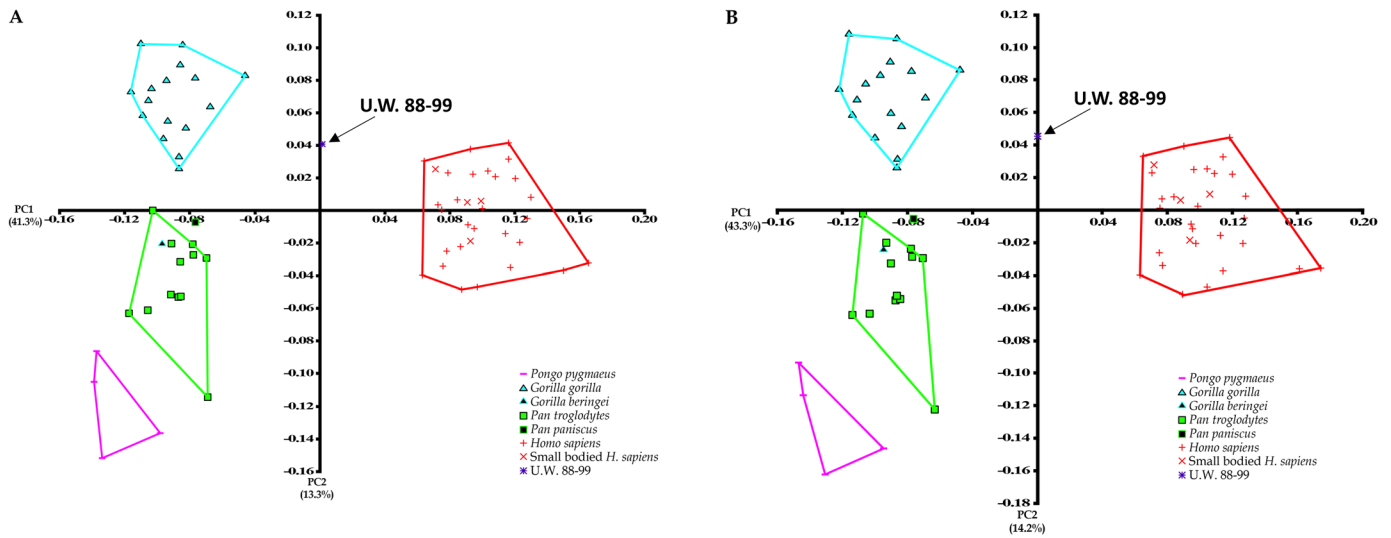


Figure 38. Geometric morphometrics analysis of the calcaneus. Principal component analysis comparing Au. sediba to the living great apes across principal component 1 (horizontal axis) and principal component 2 (vertical axis). A) Analysis includes estimations for landmarks 1 and 2 on the damaged cuboid facet of U.W. 88-99. PC1 explains 43.5% of the variance and PC 2 explains 13.3%. B) Analysis without estimated landmarks. PC1 explains 43.3% of the variance and PC 2 explains 14.2%. Notice the position of Au. sediba in the morphospace between modern humans and gorillas.

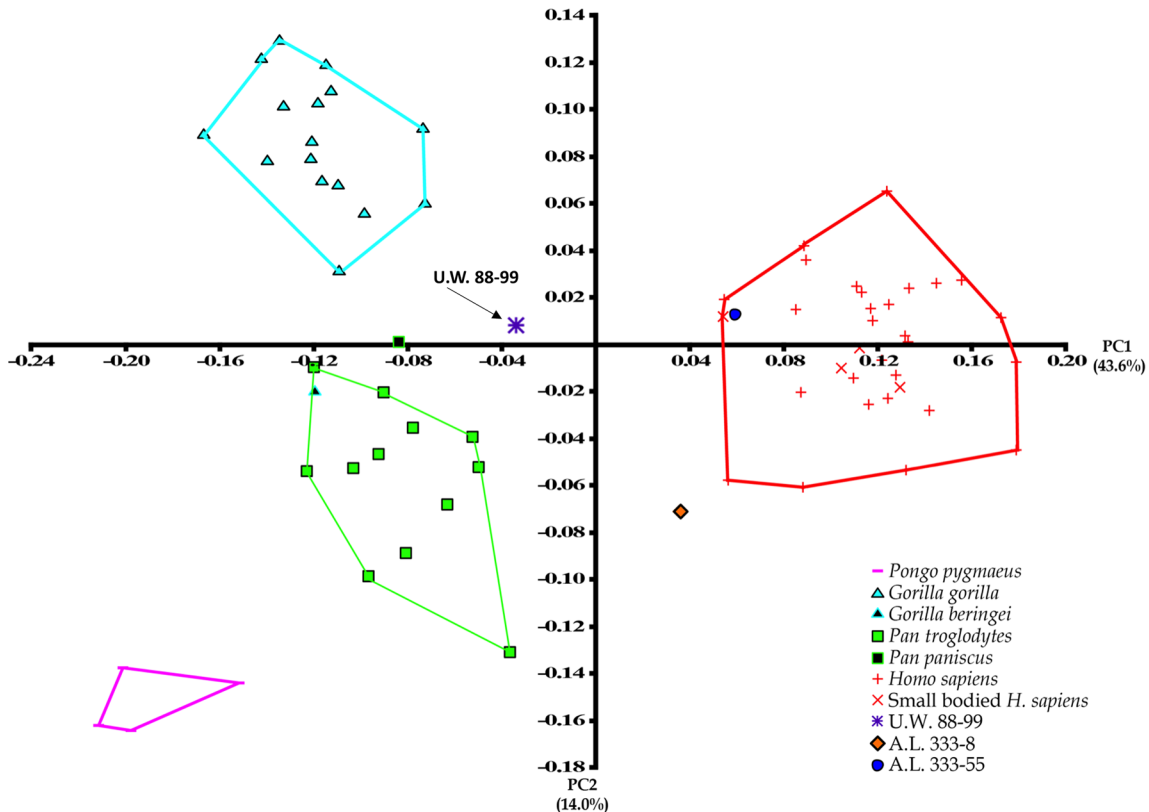


Figure 39. Geometric morphometrics analysis of the calcaneus comparing Au. sediba to the living great apes and other australopithecus across principal component 1 (horizontal axis) and principal component 2 (vertical axis). Analysis comparing the U.W. 88-99 calcaneus to A.L. 333-8 and A.L. 333-55 calcanei. Due to the damage on the Hadar specimens, landmarks 1–8 were excluded from the analysis; only landmarks 9–20 were compared. PC1 explains 43.6% of the variance and PC 2 explains 14%. Notice that while Au. afarensis is at or near the periphery of the modern human distribution, Au. sediba is well outside the human range.

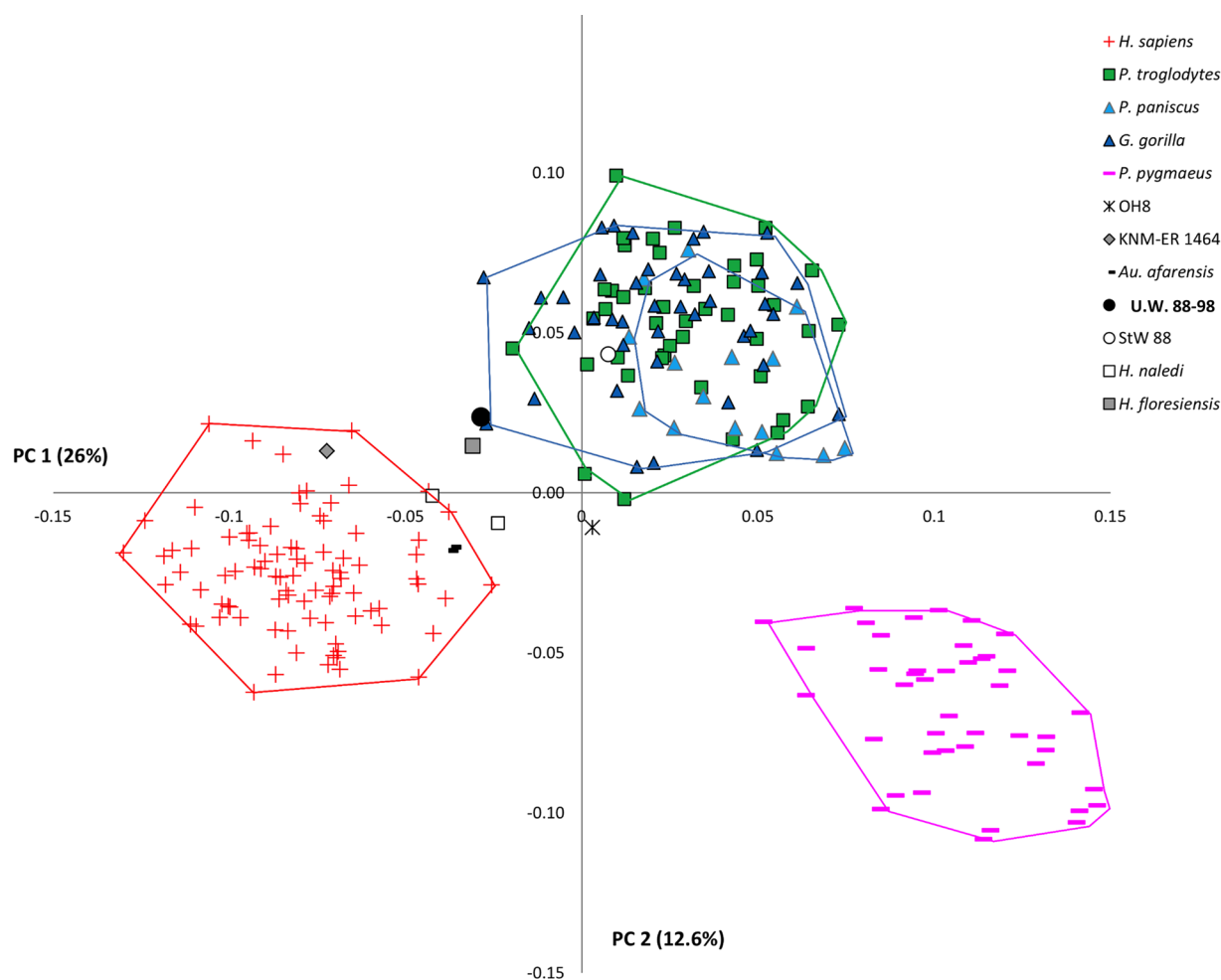


Figure 40. Geometric morphometric analysis of the talus, PC1 vs. PC2. PC1 explains 26% of the variance, and PC2 explains 12.6%. Extant colors: *H. sapiens*—red, Pongo—pink, Gorilla—green, Pan troglodytes—dark blue, Pan paniscus—turquoise. Notice that *Au. sediba* falls between humans and African apes for talar shape.

cal manner than exhibited by other hominins, such as *Au. afarensis* or *Au. africanus*. The vertically oriented shank, limited talar wedging, anteroposteriorly expanded tibial metaphysis, and mediolaterally broad calcaneal tuberosity are bipedal adaptations that *Au. sediba* shares in common with other australopiths. There is evidence for more midfoot mobility than is seen in many other australopiths. The talar head has minimal ape-like torsion and the base of the fourth metatarsal is dorsoplantarly convex, which could be evidence for a midtarsal break.

As we have detailed elsewhere (DeSilva et al. 2013), a hyperpronating bipedal gait is one explanation for how a rigid foot could unlock and result in excessive midfoot mobility in the sagittal plane. A hyperpronating gait of *Au. sediba* during terrestrial bipedalism may be a functional kinematic compromise to also retaining a high degree of arboreal structural adaptation in the midfoot. Adaptations for arboreality in *Au. sediba* probably would alter its terrestrial gait kinematics during bipedal bouts. As in large-bodied arboreal apes, *Au. sediba* possessed a mediolaterally

broad medial malleolus, a ‘beaked’ medial plantar process (e.g., for the origin of the *M. flexor digitorum brevis*), strong lateral pedal musculature (e.g., *M. abductor digiti minimi*), and a mobile midfoot—all of which are anatomies consistent with arboreality. The medial column of the foot will be critical for testing hypotheses about the selective importance of arboreal locomotor behavior in *Au. sediba*. These findings suggest that different australopith species had both diverse locomotor strategies and variation in locomotor kinematics.

The combination of hip, knee, and foot anatomies discovered at Malapa, South Africa, is different from those attributed to either *Au. afarensis* or *Au. africanus* (Table 14). With the discovery of the 3.4 Ma foot from Burtele, Ethiopia (Haile-Selassie et al. 2012), it is now becoming clear that during the Pliocene australopith radiation, different forms of bipedal gait kinematics evolved (Harcourt-Smith and Aiello 2004; Robinson 1972), with different combinations of pedal adaptations for upright walking occurring in different lineages.

**TABLE 14. MOSAIC ANATOMY OF *AU. SEDIBA* FOOT.**

Element	Morphology in <i>Au. sediba</i>	Other fossil hominins with this anatomy	Interpretation
<i>Calcaneus</i>	Dorsally positioned lateral plantar process	None	Hadar australopiths have human-like plantar LPPs making <i>Au. sediba</i> more primitive for this anatomy.
	Gracile tuberosity	StW 352 ( <i>Au. africanus</i> ); Omo; Dinaledi	Unlike the Hadar australopiths in having a quite gracile tuberosity (Prang 2015).
	Angled Achilles insertion	None, though Hadar hominins are more angled than most extant African apes.	Possible that <i>Au. sediba</i> had an elongated Achilles tendon.
	Highly convex subtalar joint	StW 352 ( <i>Au. africanus</i> )	Hadar hominins have flatter subtalar joint. A curved joint has been functionally related to inversion.
	Weakly angled sustentaculum talus	Hadar, Dinaledi	Possibly related to low longitudinal arching of rearfoot.
	Locking cuboid facet	Omo, OH 8, Dinaledi	There is heavy erosion around this area in <i>Au. sediba</i> , but what is preserved more closely resembles a human than an extant African ape.
<i>Talus</i>	Low talar axis angle	All australopiths	A critical bipedal adaptation that orients the tibial shaft vertical to the foot.
	Low wedging of talar trochlea	All australopiths	Indicates limited loading of the foot in excessive dorsiflexion, as seen in apes.
	Mediolaterally flat talar trochlea	Hadar hominins; Dmanisi	Highly variable feature; significance unclear given the deep keeling in specimens from Sterkfontein, Koobi Fora, and OH 8.
	High talar declination angle	Tali often attributed to <i>Homo</i>	Evidence for at least partially arched foot (but see Prang 2015).
	Low head torsion angle	Some australopiths, but <i>Au. sediba</i> has lowest angle	Increased midfoot mobility in <i>Au. sediba</i> .
<i>Metatarsals</i>	Convex base of 4th metatarsal	None	Midtarsal break in MH1; absent in other known australopiths.
	Pattern of metatarsal robusticity (4th>5th)	Dmanisi	May reflect normal variation given human-like pattern in OH 8.
	External torsion of 4th metatarsal	All other hominins, including Burtele foot	Unclear. Perhaps related to arch of the foot.
<i>Distal tibia</i>	Tibial plafond angle ~90°	All other non-pathological hominins	Critical bipedal adaptation that positions the shank vertically over the foot.
	Anteroposteriorly expanded metaphysis	All other hominins	Probable early bipedal adaptation that expanded volume of ankle for stress dissipation during walking.
	Increased depth of tibial surface	All other non-pathological hominins	May reduce tibiotalar range of motion relative to the extant African apes.
	Posterior tibial arch angle	Variable	Evidence for at least a partially-arched foot.
	Mediolaterally thick medial malleolus in both MH2 and MH4	None	Arboreal signal related to loading of the foot in inversion (Zipfel et al. 2011).

**ACKNOWLEDGEMENTS**

We are grateful to the many facilities that permitted access to specimens in their care: Department of Anthropology, The University of Tennessee, Department of Anthropology, University of Vienna, Max Planck Institute for Evolutionary Anthropology, National Museum of Natural History, Smithsonian Institution (Washington, D.C.), Museum für Naturkunde (Berlin), School of Anatomical Sciences (University of the Witwatersrand), American Museum of Natural History (NY), Yale Peabody Museum (New Haven, CT), Powell Cotton Museum (Birchington, Kent, UK), Natural

History Museum (London, UK), and the Royal African Museum (Tervuren, Belgium). Additional and special thanks to colleagues who facilitated access to fossil remains. These include Emma Mbua, Fredrick Kyalo Manthi, Job Kibii, and the National Museum of Kenya. We are grateful to Desalegn Abebaw, Yared Assefa, Metasebia Endalamaw, Tomas Getachew, and the Authority for Research and Conservation of Cultural Heritage, Ethiopia, for the opportunity to study fossil pedal material at the National Museum of Ethiopia. Thank you to Amandas Kwekason and Paul Msemwa, and the Tanzanian Commission for Science and Technology

for permission to study the OH 8 foot at the National Museum of Tanzania. Thank you to the Evolutionary Studies Institute and University of the Witwatersrand Fossil Access Advisory Committee for permitting our study of fossil material housed at the ESI in Johannesburg, South Africa. And, to K. Jakata for assistance at the Palaeosciences Centre Microfocus X-ray CT facility of the University of the Witwatersrand (see [www.wits.ac.za/microCT](http://www.wits.ac.za/microCT) for addition information on the system). Thank you to Stephany Potze for her assistance at the Ditsong Museum of Natural History (Pretoria, South Africa). Funding for this study was provided by the National Geographic Society, National Research Foundation, National Science Foundation, African Origins Platform, Leakey Foundation, and Dartmouth College.

## REFERENCES

- Aiello, L.C. and Dean, C. 2002. *An Introduction to Human Evolutionary Anatomy*. Academic Press, London.
- Archibald J.D., Lovejoy, C.O., and Heiple, K.G. 1972. Implications of relative robusticity in the Olduvai metatarsus. *American Journal of Physical Anthropology* 37, 93–95.
- Baker, B.J., Dupras, T.L., and Tocheri, M.W. 2005. *The Osteology of Infants and Children*. Texas A&M University Press, College Station.
- Bates, K.T., Collins, D., Savage, R., McClymont, J., Webster, E., Pataky, T.C., D’Août, K., Sellers, W.I., Bennett, M.R., and Crompton, R.H. 2013. The evolution of compliance in the human lateral mid-foot. *Proceedings of the Royal Society B* 280, 20131818.
- Berger, L.R. and Tobias, P.V. 1996. A chimpanzee-like tibia from Sterkfontein, South Africa and its implications for the interpretation of bipedalism in *Australopithecus africanus*. *Journal of Human Evolution* 30, 343–348.
- Berger, L.R., de Ruiter, D., Churchill, S.E., Schmid, P., Carlson, K.J., Dirks, P.H.G.M., and Kibii, J.B. 2010. *Australopithecus sediba*: a new species of *Homo*-like australopithecine from South Africa. *Science* 328, 195–204.
- Berger, L.R. 2012. *Australopithecus sediba* and the earliest origins of the genus *Homo*. *Journal of Anthropological Science* 90, 1–16.
- Berillon, G. 2003. Assessing the longitudinal structure of the early hominin foot: a two-dimensional architecture analysis. *Human Evolution* 18, 113–122.
- Bojsen-Møller, F. 1979. Calcaneocuboid joint and stability of the longitudinal arch of the foot at high and low gear push off. *Journal of Anatomy* 129, 165–176.
- Boyle, E.K., McNutt, E.J., Sasaki, T., Suwa, G., Zipfel, B., and DeSilva, J.M. 2018. A quantification of calcaneal lateral plantar process position with implications for bipedal locomotion in *Australopithecus*. *Journal of Human Evolution* 123, 24–34.
- Churchill, S.E., Holliday, T.W., Carlson, K.J., Jashashvili, T., Macias, M.E., Mathews, S., Sparling, T.L., Schmid, P., de Ruiter, D.J., and Berger, L.R. 2013. The upper limb of *Australopithecus sediba*. *Science* 340, 1233477.
- Churchill, S.E., Kibii, J.M., Schmid, P., Reed, N.D., and Berger, L.R. 2018 (this volume). The pelvis of *Australopithecus sediba*. *PaleoAnthropology* 2018, 334–356.
- Clarke, R. and Tobias, P. V. 1995. Sterkfontein member 2 foot bones of the oldest South African hominid. *Science* 269, 521–524.
- Collyer, M.L., Sekora, D.J., and Adams, D.C. 2015. A method for analysis of phenotypic change for phenotypes described by high-dimensional data. *Heredity* 115, 357–365.
- Crompton, R.H., Pataky, T.C., Savage, R., D’Août, K., Bennett, M.R., Day, M.H., Bates, K., Morse, S., and Sellers, W.I. 2012. Human-like external function of the foot, and fully upright gait, confirmed in the 3.66 million year old Laetoli hominin footprints by topographic statistics, experimental footprint-formation and computer simulation. *Journal of the Royal Society Interface* 9, 707–719.
- Day, M.H. 1969. Femoral fragment of a robust australopithecine from Olduvai Gorge, Tanzania. *Nature* 221, 230–233.
- Day, M.H. and Wood, B.A. 1968. Functional affinities of the Olduvai Hominin 8 talus. *Man* 3, 440–455.
- Deloison, Y. 2003. Anatomie des os fossiles de pieds des hominides d’Afrique du sud dates entre 2,4 et 3,5 millions d’années. Interprétation quant à leur mode de locomotion. *Biométrie Humaine et Anthropologie*. 21, 189–230.
- Dembo, M., Radovčić, D., Garvin, H.M., Laird, M.F., Schroeder, L., Scott, J., Brophy, J., Ackerman, R.R., Musiba, C.M., de Ruiter, D.J., and Mooers, A.Ø. 2016. The evolutionary relationships and age of *Homo naledi*: an assessment using dated Bayesian phylogenetic methods. *Journal of Human Evolution* 97, 17–26.
- de Ruiter, D.J., Carlson, K.B., Brophy, J.K., Churchill, S.E., Carlson, K.J., and Berger, L.R. 2018 (this volume). The skull of *Australopithecus sediba*. *PaleoAnthropology* 2018, 56–155.
- de Ruiter, D.J., DeWitt, T.J., Carlson, K.B., Brophy, J.K., Schroeder, L., Ackermann, R.R., Churchill, S.E., and Berger, L.R. 2013. Mandibular remains support taxonomic validity of *Australopithecus sediba*. *Science* 340, 1232997.
- de Ruiter, D.J., Churchill, S.E., and Berger, L.R. 2013. *Australopithecus sediba* from Malapa, South Africa. In *The Paleobiology of Australopithecus*, Reed, K.E., Fleagle, J.G., and Leakey, R.E. (eds.). Springer, New York, pp. 147–162.
- DeSilva, J.M. 2009. Functional morphology of the ankle and the likelihood of climbing in early hominins. *Proceedings of the National Academy of Sciences USA* 106, 6567–6572.
- DeSilva, J.M. 2010. Revisiting the “midtarsal break”. *American Journal of Physical Anthropology* 141, 245–258.
- DeSilva, J.M. and Throckmorton, Z.J. 2010. Lucy’s flat feet: the relationship between the ankle and rearfoot arching in early hominins. *PLoS One* 5, e14432.
- DeSilva, J.M. and Gill, S.V. 2013. Brief communication: a midtarsal (midfoot) break in the human foot. *American Journal of Physical Anthropology* 151, 495–499.
- DeSilva, J.M., Holt, K.G., Churchill, S.E., Carlson, K.J., Walker, C.S., Zipfel, B., and Berger, L.R. 2013. The low-

- er limb and the mechanics of walking in *Australopithecus sediba*. *Science* 340, 1232999.
- DeSilva, J.M., Bonne-Anne, R., Swanson, Z., Gill, C.M., Sobel, M., Uy, J., and Gill, S.V. 2015. Midtarsal break variation in modern humans: functional causes, skeletal correlates, and paleontological implications. *American Journal of Physical Anthropology* 156, 543–552.
- Dowdeswell, M.R., Jashashvili, T., Patel, B.A., Lebrun, R., Susman, R.L., Lordkipanidze, D., and Carlson, K.J. 2017. Adaptation to bipedal gait and fifth metatarsal structural properties in *Australopithecus*, *Paranthropus*, and *Homo*. *Comptes Rendus Palevol* 16, 585–599.
- Drapeau, M.S. and Harmon, E.H. 2013. Metatarsal torsion in monkeys, apes, humans and australopithecids. *Journal of Human Evolution* 64, 93–108.
- Elftman, H. and Manter, J. 1935. Chimpanzee and human feet in bipedal walking. *American Journal of Physical Anthropology* 20, 69–79.
- Fisk, G.R. and Macho, G.A. 1992. Evidence of a healed compression fracture in a Plio-Pleistocene hominid talus from Sterkfontein, South Africa. *International Journal of Osteoarchaeology* 2, 325–332.
- Freidline, S.E., Gunz, P., Hublin, J.-J. 2015. Ontogenetic and static allometry in the human face: contrasting Khoisan and Inuit. *American Journal of Physical Anthropology* 158, 116–131.
- Gebo, D.L. and Schwartz, G.T. 2006. Foot bones from Omo: implications for human evolution. *American Journal of Physical Anthropology* 129, 499–511.
- Gill, C.M., Taneja, A.K., Bredella, M.A., Torriani, M., and DeSilva, J.M. 2014. Osteogenic relationship between the lateral plantar process and the peroneal tubercle in the human calcaneus. *Journal of Anatomy* 22, 173–179.
- Gunz, P., Mitteroecker, P., and Bookstein, F.L. 2005. Semilandmarks in three dimensions. In *Modern Morphometrics in Physical Anthropology*, Slice, D. (ed.). Kluwer Academic/Plenum Publishers, New York, pp. 73–98.
- Gunz, P., Mitteroecker, P., Neubauer, S., Weber, G.L., and Bookstein, F.L. 2009. Principles for the virtual reconstruction of hominin crania. *Journal of Human Evolution* 57, 48–62.
- Haile-Selassie, Y., Saylor, B.Z., Deino, A., Levin, N.E., Alene, M., and Latimer, B.M. 2012. A new hominin foot from Ethiopia shows multiple Pliocene bipedal adaptations. *Nature* 483, 565–569.
- Harcourt-Smith, W.E.H. 2002. *Form and Function in the Hominoid Tarsal Skeleton*. Ph.D. Dissertation, University of London.
- Harcourt-Smith, W.E.H. and Aiello, L.C. 2004. Fossils, feet and the evolution of human bipedal locomotion. *Journal of Anatomy* 204, 403–416.
- Harcourt-Smith, W.E.H., Throckmorton, Z., Congdon, K.A., Zipfel, B., Deane, A.S., Drapeau, M.S.M., Churchill, S.E., Berger, L.R., and DeSilva, J.M. 2015. The foot of *Homo naledi*. *Nature Communications* 6, 8432.
- Heiple, K.G. and Lovejoy, C.O. 1971. The distal femoral anatomy of *Australopithecus*. *American Journal of Physical Anthropology* 35, 75–84.
- Holliday, T., Churchill, S.E., Carlson, K., DeSilva, J., Schmid, P., Walker, C., and Berger, L.R. 2018 (this volume). Body size and proportions of *Australopithecus sediba*. *PaleoAnthropology* 2018, 406–422.
- Irish, J.D., Guatelli-Steinberg, D., Legge, S.S., de Ruiter, D.J., and Berger, L.R. 2013. Dental morphology and the phylogenetic “place” of *Australopithecus sediba*. *Science* 340, 1233062.
- Jungers, W.L., Harcourt-Smith, W.E.H., Wunderlich, R.E., Tocheri, M.W., Larson, S.G., Sutikna, T., Due, R.A., and Morwood, M.J. 2009a. The foot of *Homo floresiensis*. *Nature* 459, 81–84.
- Jungers, W.L., Larson, S.G., Harcourt-Smith, W.E.H., Morwood, M.J., Sutikna, T., Awe, R.D., and Djubiantono, T. 2009b. Descriptions of the lower limb skeleton of *Homo floresiensis*. *Journal of Human Evolution* 57, 538–554.
- Kachlik, D., Baca, V., Cepelik, M., Hajek, P., Mandys, V., and Musil, V. 2008. Clinical anatomy of the calcaneal tuberosity. *Annals of Anatomy - Anatomischer Anzeiger* 190, 284–291.
- Kaplan, E.B. 1958. The iliotibial tract. *Journal of Bone and Joint Surgery*. 40, 817–832.
- Kibii, J.M., Churchill, S.E., Schmid, P., Carlson, K.J., Reed, N.D., de Ruiter, D.J., and Berger, L.R. 2011. A partial pelvis of *Australopithecus sediba*. *Science* 333, 1407–1411.
- Kidd, R. 1993. The long arch: new thoughts on the evolution of an old structure. *Australian Podiatrist* June, 35–43.
- Kivell, T.L., Churchill, S.E., Kibii, J.M., Schmid, P., and Berger, L.R. 2018 (this volume). The hand of *Australopithecus sediba*. *PaleoAnthropology* 2018, 282–333.
- Kivell, T.L., Kibii, J.M., Churchill, S.E., Schmid, P., and Berger, L.R. 2011. *Australopithecus sediba* hand demonstrates mosaic evolution of locomotor and manipulative abilities. *Science* 333, 1411–1417.
- Latimer, B., Ohman, J.C., and Lovejoy, C.O. 1987. Talocrural joint in African hominoids: Implications for *Australopithecus afarensis*. *American Journal of Physical Anthropology* 74, 155–175.
- Latimer, B. and Lovejoy, C.O. 1989. The calcaneus of *Australopithecus afarensis* and its implications for the evolution of bipedality. *American Journal of Physical Anthropology* 78, 369–386.
- Le Gros Clark, W.E. 1947. Observations on the anatomy of the fossil Australopithecinae. *Journal of Anatomy* 81, 300–333.
- Logan, B.M., Singh, D., and Hutchins, R.T. 2004. *McMinn's Color Atlas of Foot and Ankle Anatomy*. Mosby, Toronto.
- Lordkipanidze, D., Jashashvili, T., Vekua, A., Ponce de León, M., Zollikofer, C.P.E., Rightmire, G.P., Pontzer, H., Ferring, R., Oms, O., Tappen, M., Bukhshianidze, M., Agusti, J., Kahlke, R., Kiladze, G., Martinez-Navarro, B., Mouskhelishvili, A., Nioradze, M., and Rook, L. 2007. Postcranial evidence from early *Homo* from Dmanisi, Georgia. *Nature* 449, 205–310.
- Lovejoy, C.O., Heiple, K. G., and Burstein, A.H. 1973. The gait of *Australopithecus*. *American Journal of Physical Anthropology* 38, 757–780.
- Lovejoy, C.O., Johanson, D.C., and Coppens, Y. 1982. Hom-

- inid lower limb bones recovered from the Hadar Formation: 1974-1977 collections. *American Journal of Physical Anthropology* 57, 679–700.
- Lovejoy, C.O., Meindl, R.S., Ohman, J.C., Heiple, K.G., and White, T.D. 2002. The Maka femur and its bearing on the antiquity of human walking: applying contemporary concepts of morphogenesis to the human fossil record. *American Journal of Physical Anthropology* 119, 97–133.
- Lovejoy, C.O. 2007. The natural history of human gait and posture. Part 3. The knee. *Gait Posture* 25, 325–341.
- Lovejoy, C.O., Latimer, B., Suwa, G., Asfaw, B., and White, T.D. 2009. Combining prehension and propulsion: the foot of *Ardipithecus ramidus*. *Science* 326, 72e1–72e8.
- Lovejoy, C.O., Suwa, G., Spurluck, L., Asfaw, B., and White, T.D. 2009. The pelvis and femur of *Ardipithecus ramidus*: the emergence of upright walking. *Science* 326, 71–71e6.
- MacLachy, L.M. 1996. Another look at the australopithecine hip. *Journal of Human Evolution* 31, 455–476.
- Marchi, D., Walker, C.S., Wei, P., Holliday, T.W., Churchill, S.E., Berger, L.R., and DeSilva, J.M. 2017. The thigh and leg of *Homo naledi*. *Journal of Human Evolution* 104, 174–204.
- McHenry, H.M. and Corruccini, R.S. 1978. The femur in human evolution. *American Journal of Physical Anthropology* 49, 473–487.
- McNutt, E.J., Claxton, A.G., and Carlson, K.J. 2017. Revisiting the peroneal trochlea of the StW 352 calcaneus. *South African Journal of Science* 113, 1–5.
- Mitteroecker P, Gunz P, Bernhard M, Schaefer K, and Bookstein FL. 2004. Comparison of cranial ontogenetic trajectories among great apes and humans. *Journal of Human Evolution* 46, 679–698.
- Napier, J.R. 1964. The evolution of bipedal walking in the hominids. *Archives de Biologie* 75, 673–708.
- Ohman, J.C., Krochta, T.J., Lovejoy, C.O., Mensforth, R.P., and Latimer, B. 1997. Cortical bone distribution in the femoral neck of hominoids: implications for the locomotion of *Australopithecus afarensis*. *American Journal of Physical Anthropology* 104, 117–131.
- Passalacqua, N.V. 2013. Subadult age-at-death estimation from the human calcaneus. *International Journal of Osteoarchaeology* 23, 471–474.
- Patel, B., Jashashvili, T., Bui, S.H., Carlson, K.J., Griffin, N.L., Wallace, I.J., Orr, C.M., and Susman, R.L. 2018. Inter-ray variation in metatarsal strength properties in humans and Africa apes: implications for inferring bipedal biomechanics in the Olduvai Hominid 8 foot. *Journal of Human Evolution* 121, 147–165.
- Pickering, R., Dirks, P.H., Jinnah, Z., de Ruiter, D.J., Churchill, S.E., Herries, A.I., Woodhead, J.D., Hellstrom, J.C., and Berger, L.R. 2011. *Australopithecus sediba* at 1.977 Ma and implications for the origins of the genus *Homo*. *Science* 333, 1421–1423.
- Pontzer, H., Rolian, C., Rightmire, G.P., Jashashvili, T., Ponce de León, M.S., Lordkipanidze, D., and Zollikofer, C.P. 2010. Locomotor anatomy and biomechanics of the Dmanisi hominins. *Journal of Human Evolution* 58, 492–504.
- Prang, T.C. 2015. Rearfoot posture of *Australopithecus sediba* and the evolution of the hominin longitudinal arch. *Scientific Reports* 5, 17677.
- Prang, T.C. 2016. The subtalar joint complex of *Australopithecus sediba*. *Journal of Human Evolution* 90, 105–119.
- Richmond, B.R. and Jungers, W.L. 2008. *Orrorin tugenensis* femoral morphology and the evolution of hominin bipedalism. *Science* 319, 1662–1665.
- Rohlf, F.J. and Slice, D. 1990. Extensions of the Procrustes method for optimal superimposition of landmarks. *Systematic Zoology* 39, 40–59.
- Robinson, J.T. 1972. *Early Hominid Posture and Locomotion*. The University of Chicago Press, Chicago.
- Ruff, C.B. 1995. Biomechanics of the hip and birth in early *Homo*. *American Journal of Physical Anthropology* 98, 527–574.
- Ruff, C.B. and Higgins, R. 2013. Femoral neck structure and function in early hominins. *American Journal of Physical Anthropology* 150, 512–525.
- Kelikian, A.S. 2011. *Sarraffian's Anatomy of the Foot and Ankle. Descriptive, Topographic, Functional*. Lippincott Williams & Wilkins, Philadelphia.
- Sarmiento, E.E. 1983. The significance of the heel process in anthropoids. *International Journal of Primatology* 4, 127–152.
- Scheuer, L. and Black, S. 2004. *The Juvenile Skeleton*. Elsevier Academic Press, New York.
- Scheuer, L. and Black, S. 2008. *Juvenile Osteology*. Elsevier Academic Press, New York.
- Stern, J.T. and Susman, R.L. 1983. The locomotor anatomy of *Australopithecus afarensis*. *American Journal of Physical Anthropology* 60, 279–317.
- Susman, R.L. and Stern, J.T. 1982. Functional morphology of *Homo habilis*. *Science* 217, 931–934.
- Swindler, D.R. and Wood, C.D. 1973. *An Atlas of Primate Gross Anatomy*. University of Washington Press, Seattle.
- Sylvester, A.D., Mahfouz, M.R., and Kramer, P.A. 2011. The effective mechanical advantage of A.L. 129-1a for knee extension. *Anatomical Record* 294, 1486–1499.
- Tardieu, C. 1981. Morpho-functional analysis of the articular surfaces of the knee-joint in primates. In *Primate Evolutionary Biology*, Chiarelli, A.B. and Corruccini, R.S. (eds.). Springer-Verlag, New York, pp. 68–80.
- Tardieu, C. 2010. Development of the human hind limb and its importance for the evolution of bipedalism. *Evolutionary Anthropology* 19, 174–186.
- Val, A. 2014. *A 3D Approach to Understand the Taphonomy of the Early Hominins from the Plio-Pleistocene Cave Site of Malapa*. Ph.D. Dissertation, University of the Witwatersrand.
- Ward, C.V., Kimbel, W.H., and Johanson, D.C. 2011. Complete fourth metatarsal and arches in the foot of *Australopithecus afarensis*. *Science* 331, 750–753.
- Ward, C.V., Kimbel, W.H., Harmon, E.H., and Johanson, D.C. 2012. New postcranial fossils of *Australopithecus afarensis* from Hadar, Ethiopia (1990-2007). *Journal of Human Evolution* 63, 1–51.

- Ward, C.V., Feibel, C.S., Hammond, A.S., Leakey, L.N., Moffett, E.A., Plavcan, J.M., Skinner, M.M., Spoor, F., and Leakey, M.G. 2015. Associated ilium and femur from Koobi Fora, Kenya, and postcranial diversity in early *Homo*. *Journal of Human Evolution* 81, 48–67.
- Weidenreich, F. 1940. The external tubercle of the human tuber calcanei. *American Journal of Physical Anthropology* 26, 473–487.
- Williams, S.A., Meyer, M.R., Nalla, S., Gracia-Martinez, D., Nalley, T.K., Eyre, J., Prang, T.C., Bastir, M., Schmid, P., Churchill, S.E., and Berger, L.R. 2018 (this volume). The vertebrae, ribs, and sternum of *Australopithecus sediba*. *PaleoAnthropology* 2018, 156–233.
- Wood, B., Aiello, L., Wood, C., and Key, C. 1988. A technique for establishing the identity of ‘isolated’ fossil hominin limb bones. *Journal of Anatomy* 193, 61–72.
- Zhang, A.Y., and DeSilva, J.M. 2018 (this volume). Computer animation of the walking mechanics of *Australopithecus sediba*. *PaleoAnthropology* 2018, 423–432.
- Zipfel, B. and Berger, L.R. 2009. Partial hominin tibia (StW 396) from Sterkfontein, South Africa. *Palaeontologia Africana* 44, 71–75.
- Zipfel, B., DeSilva, J.M., and Kidd, R.S. 2009. Earliest complete hominin fifth metatarsal—implications for the evolution of the lateral column of the foot. *American Journal of Physical Anthropology* 140, 532–545.
- Zipfel, B., DeSilva, J.M., Kidd, R.S., Carlson, K.J., Churchill, S.E., and Berger, L.R. 2011. The foot and ankle of *Australopithecus sediba*. *Science* 333, 1417–1420.